

SCIENCE REQUIREMENTS DOCUMENT (SRD)

*Observation and Analysis of Smectic Islands in Space  
(OASIS)*

Professor Noel Clark – Principal Investigator  
*Department of Physics  
University of Colorado – Boulder*

Research Professor Joseph MacLennan – Co-Investigator  
*Department of Physics  
University of Colorado – Boulder*

Research Professor Matthew Glaser – Co-Investigator  
*Department of Physics  
University of Colorado – Boulder*

Professor Ralf Stannarius – Co-Investigator  
*Department of Physics  
University of Magdeburg*

Dr. Padetha Tin – Project Scientist  
*National Center for Space Exploration Research  
NASA Glenn Research Center*

Nancy R. Hall – Project Manager  
*NASA Glenn Research Center*

August 15<sup>th</sup>, 2011

FINAL DRAFT

SCIENCE REQUIREMENTS DOCUMENT (SRD)Observation and Analysis of Smectic Islands in Space  
(OASIS)

Professor Noel Clark  
Principal Investigator  
University of Colorado – Boulder

Signature

Date

9/22/2011

Research Professor Joseph MacLennan  
Co-Investigator  
University of Colorado – Boulder

Signature

Date

9/22/11

Research Professor Matthew Glaser  
Co-Investigator  
University of Colorado – Boulder

Signature

Date

9/22/2011

Professor Ralf Stannarius  
Co-Investigator  
University of Magdeburg, Germany

Signature

Date

9/12/2011

Concurrences:

Padetha Tin  
Project Scientist

Signature

Date

9/30/2011

Nancy R. Hall  
Project Manager

Signature

Date

9/30/11

Thomas H. St. Onge  
Chief, ISS and Human Health Office

Signature

Date

10/7/2011

Fred Kohl  
ISS Research Project Manager

Signature

Date

09/30/2011

Francis P. Chiaramonte  
Program Executive for Physical Sciences

Signature

Date

11/8/2011

SCIENTIFIC INVESTIGATORS

*Observation and Analysis of Smectic Islands in Space  
(OASIS)*

PRINCIPAL INVESTIGATOR

NOEL CLARK

Professor  
Department of Physics  
University of Colorado  
Boulder, CO 80309  
tel: (303) 492-6420  
fax: (303) 492-2998  
email: [noel.clark@colorado.edu](mailto:noel.clark@colorado.edu)

CO – INVESTIGATOR

JOSEPH MACLENNAN

Research Professor  
Department of Physics  
University of Colorado  
Boulder, CO 80309  
tel: (303) 492-7543  
fax: (303) 492-2998  
email: [jem@colorado.edu](mailto:jem@colorado.edu)

CO – INVESTIGATOR

MATTHEW GLASER

Research Professor  
Department of Physics  
University of Colorado  
Boulder, CO 80309  
tel: (303) 492-3029  
fax: (303) 492-2998  
email: [glaser@colorado.edu](mailto:glaser@colorado.edu)

CO – INVESTIGATOR

RALF STANNARIUS

Professor  
Department of Physics  
University of Magdeburg  
D-39106 Magdeburg, Germany  
tel: +49 (0391) 67-18582  
fax: +49 (0391) 67-18108  
email: [ralf.stannarius@physik.uni-magdeburg.de](mailto:ralf.stannarius@physik.uni-magdeburg.de)

PROJECT SCIENTIST  
PADETHA TIN

*Staff Scientist*  
*National Center For Microgravity Research*  
*NASA Glenn Research Center*  
*Cleveland, OH 44135*  
*tel: (216) 433-8164*  
*fax: (216) 433-5033*  
*email: [padetha.tin@grc.nasa.gov](mailto:padetha.tin@grc.nasa.gov)*

## TABLE OF CONTENTS

<b>NOMENCLATURE .....</b>	<b>1</b>
SYMBOLS .....	1
SCIENTIFIC ACRONYMS.....	1
TECHNICAL ACRONYMS .....	2
ADMINISTRATIVE ACRONYMS .....	2
<b>OBSERVATION AND ANALYSIS OF SMECTIC ISLANDS IN SPACE (OASIS).....</b>	<b>3</b>
<b>EXECUTIVE SUMMARY .....</b>	<b>3</b>
<b>1 – INTRODUCTION &amp; SCIENCE BACKGROUND.....</b>	<b>5</b>
1.1 – BACKGROUND AND RESEARCH CONTEXT .....	5
1.1.1 – <i>Thermotropic Smectic Liquid Crystals</i> .....	5
1.1.2 – <i>Freely Suspended Liquid Crystal Films</i> .....	5
1.2 – PRIOR GROUND-BASED RESEARCH: EXAMPLES OF FSLC PHYSICS .....	7
1.2.1 – <i>Formation and Coarsening Dynamics of Topological Defects in 2D</i> .....	7
1.2.2 – <i>Using Free Films to Elucidate Novel Structures</i> .....	8
1.2.3 – <i>Orientational Solitons in 2D</i> .....	9
1.2.4 – <i>Elucidation of Interlayer Orientational Ordering in Novel Smectic Phases</i> .....	9
1.2.5 – <i>Identification of Novel Polar Smectic Phases</i> .....	10
1.2.6 – <i>Chiral Smectics in the High-P Electroelastic Regime</i> .....	11
1.2.7 – <i>Gas Permeation of Smectic Films</i> .....	12
1.2.8 – <i>Rupture of Smectic Films</i> .....	13
1.3 – ATOMISTIC AND COARSE-GRAINED SIMULATION OF SMECTICS .....	13
1.3.1 – <i>Molecular Nanosegregation by Photoisomerization</i> .....	13
1.3.2 – <i>Anticlinic Ordering in Smectics</i> .....	14
1.3.3 – <i>Out-of-Layer Fluctuations favor Synclitic Ordering</i> .....	14
1.3.4 – <i>Interface Clinicity and Ordering in Bent-Core Systems</i> .....	15
1.3.5 – <i>Nanosegregation Drives Molecular Tilt and Layer Curvature</i> .....	15
<b>2 – PROPOSED MICROGRAVITY EXPERIMENTS: BACKGROUND / RELATED RESEARCH.....</b>	<b>17</b>
2.1 – KEY PROPERTIES OF FREELY SUSPENDED LIQUID CRYSTAL FILMS.....	17
2.2 – GENERATION AND MANIPULATION OF SMECTIC LIQUID CRYSTAL BUBBLES.....	18
2.3 – ISLANDS ON FSLC FILMS .....	18
2.3.1 – <i>Islands on FSLC Bubbles</i> .....	19
2.3.2 – <i>Dynamics of Islands</i> .....	20
2.3.3 – <i>Island Emulsions</i> .....	20
2.3.4 – <i>Interaction of Islands on FSLC Films</i> .....	21
2.3.5 – <i>Droplets of Isotropic Fluids on FSLC films</i> .....	22
2.3.6 – <i>Island and Drop Generation via Inkjet Printing</i> .....	23
2.4 – THEORETICAL BACKGROUND AND MOTIVATION .....	24
2.4.1 – <i>Stability of Smectic Films</i> .....	24
2.4.2 – <i>FSLC Film Structure and Thermodynamics</i> .....	24
2.4.3 – <i>Dislocation Dynamics</i> .....	29
2.4.4 – <i>Dislocation Structure and Energetics</i> .....	31
2.4.5 – <i>Texture-Mediated Interactions in Smectic C Films</i> .....	35
2.4.6 – <i>Hydrodynamics of Thin Smectic Films</i> .....	37
2.4.7 – <i>Thermocapillary Effects in Smectic Films</i> .....	39

2.5 – PROPOSED THEORETICAL WORK.....	40
2.5.1 – Mesoscopic Models of Dislocation Loop Dynamics .....	40
2.5.2 – Texture-Mediated Interactions in Smectic Films.....	41
2.5.3 – Structure and Interactions of Edge Dislocations in Smectic Films .....	41
2.6 – MOTIVATION FOR MICROGRAVITY RESEARCH .....	42
2.6.1 – Decoupling from Bulk .....	42
2.6.2 – Collective Behavior of One-dimensional Interfaces .....	43
2.7 – KEY ISSUES WHERE KNOWLEDGE IS LACKING.....	44
2.7.1 – 2D Hydrodynamics.....	44
2.7.2 – Probing the Collective Behavior of 1D Interfaces in a 2D Space.....	44
2.7.3 – Investigation of Thermocapillary & Marangoni Effects .....	44
2.7.4 – Study of Surface Tension and Line Tension.....	44
2.7.5 – Textural Interactions.....	44
2.8 – SCIENCE OBJECTIVES IN MICROGRAVITY ENVIRONMENT .....	44
2.8.1 – Study of 2D Hydrodynamics.....	44
2.8.2 – Probing the Collective Behavior of 1D Interfaces in a 2D Space.....	45
2.8.3 – Investigation of Thermocapillary & Marangoni Effects .....	45
2.8.4 – Study of Surface Tension and Line Tension.....	45
2.8.5 – Textural Interactions.....	45
2.8.6 – Ultraweak Interactions.....	45
2.9 – CONCEPTUAL DESIGN OF THE PROPOSED FLIGHT EXPERIMENT.....	46
2.9.1 – General Design Considerations.....	46
2.9.2 – Design Concept Features.....	47
2.10 – ANTICIPATED KNOWLEDGE TO BE GAINED: VALUE AND APPLICATIONS .....	49
2.10.1 – 2D Hydrodynamics .....	49
2.10.2 – Coarsening, Ostwald Ripening Dynamics, and Island and Droplet Interaction .....	49
2.10.3 – Thermocapillary Effects.....	49
2.10.4 – Surface Tension and Line Tension .....	49
2.10.5 – Perturbing Smectic Bubbles.....	49
<b>3 – JUSTIFICATION OF EXTENDED DURATION OF MICROGRAVITY ENVIRONMENT .....</b>	<b>50</b>
3.1 – LIMITATIONS OF TERRESTRIAL EXPERIMENT .....	50
3.2 – LIMITATIONS OF DROP TOWER AND PARABOLIC FLIGHT EXPERIMENTS.....	50
3.3 – LIMITATIONS OF MODELING .....	50
3.4 – NEED FOR MICROGRAVITY SCIENCE GLOVEBOX (MSG) .....	50
<b>4 – EXPERIMENT DETAILS.....</b>	<b>51</b>
4.1 – FLIGHT EXPERIMENT PLAN AND PROCEDURES.....	51
4.1.1 – Pre-Flight Procedures.....	51
4.1.2 – In-Flight Procedures.....	51
4.2 – FLIGHT EXPERIMENT TESTS .....	53
4.3 – POST-FLIGHT DATA HANDLING AND ANALYSIS.....	55
4.4 – GROUND TEST PLAN.....	55
4.4.1 – Flight Hardware Development.....	55
4.4.2 – Proposed Ground-Based Experiments.....	56
4.4.3 – Ground-Based Theory .....	56
<b>5 – SCIENCE EXPERIMENT REQUIREMENTS .....</b>	<b>57</b>
5.1 – SCIENCE REQUIREMENTS SUMMARY TABLE.....	57
Dynamic Inflation and Deflation of the LC Bubble .....	62
5.1.1 – OASIS hardware units.....	64

5.1.2 – Bubble Chambers.....	64
5.1.3 – Bubble Chamber Illumination.....	64
5.1.5 – Bubble Chamber Humidity.....	65
5.1.6 – Bubble Chamber Pressure.....	65
5.1.7 – Liquid Crystal Samples.....	65
5.1.8 – Bubble Inflation System.....	66
5.1.9 – Liquid Crystal Dispensing.....	66
5.1.10 – Bubble Size and Diameter Control System.....	66
5.1.11 – Experimental Air Quality.....	66
5.1.12 – Macro Observation of Entire Bubble.....	67
5.1.13 – Micro Observation of Islands.....	67
5.1.14 – Creation of Droplets on Bubble Film using Inkjet Drop Dispenser.....	67
5.1.15 – Creation of Islands and Pores on Bubble Film.....	68
5.1.16 – External Electric Field Interaction with Islands/Pores on Bubble Film.....	68
5.1.17 – Dynamic Inflation and Deflation of the LC Bubble.....	69
5.1.18 – Temperature Gradient for Marangoni Effect.....	69
5.1.19 – Island Observation & Depolarized Reflective Light Microscopy.....	69
5.1.20 – Microgravity Acceleration Measurement.....	70
5.2 – ILLUMINATION AND IMAGING OF BUBBLES AND ISLANDS (VIDEO MICROSCOPY).....	70
5.2.1 – Macro-View Imaging of the Whole Bubble.....	70
5.2.2 – Micro-View Video/Spectrometry.....	72
5.2.3 – Real-time Observation.....	72
5.3 – ASTRONAUT INVOLVEMENT AND EXPERIMENT ACTIVATION.....	72
5.4 – DATA REQUIREMENTS.....	72
5.5 – TELESCEINCE.....	72
5.6 – ACCELERATION: MAGNITUDE, DIRECTION, AND FREQUENCY.....	72
<b>6 – SUMMARY OF EXPERIMENTS.....</b>	<b>74</b>
6.1 – EXPERIMENT 1: COARSENING DYNAMICS.....	74
6.2 – EXPERIMENT 2: 2D THERMO-CAPILLARY EFFECTS.....	74
6.3 – EXPERIMENT 3: 2D HYDRODYNAMICS.....	75
6.4 – EXPERIMENT 4: NUCLEATION OF ISLANDS AND PORES.....	76
<b>7 – EXPERIMENT PROTOCOL &amp; TEST MATRICES.....</b>	<b>77</b>
7.1 – INITIAL SETUP.....	77
7.1.1 – Positioning of the Bubble Chamber.....	77
7.1.2 – Bubble Formation.....	77
7.1.3 – Generation of Islands/Droplets.....	78
7.1.4 – Test Matrix for Initial Setup.....	79
7.2.1 – Experiment 1: Coarsening Dynamics.....	81
7.2.2 – Test Matrix for Experiment 1.....	82
7.3.1 – Experiment 2: 2D Thermo-Capillary Effects.....	83
7.3.2 – Test Matrix for Experiment 2.....	84
7.4.1 – Experiment 3: 2D Hydrodynamics.....	85
7.4.2 – Test Matrix for Experiment 3.....	86
7.5.1 – Experiment 4: Nucleation of Islands and Pores.....	87
7.5.2 – Test Matrix for Experiment 4.....	87
<b>8 – FLIGHT RESULTS.....</b>	<b>88</b>
8.1 – EVALUATION OF SUCCESS CRITERIA.....	88
8.1.1 – Make and Observe 2D Island Emulsions.....	88

8.1.2 – 2D Hydrodynamics of Smectic Films and Islands .....	88
8.1.3 – Electric Field Effects .....	88
8.1.4 – Thermocapillary Effects.....	88
8.1.5 – Creation and Observation of Isotropic Droplet Interactions on Bubble.....	88
8.1.7 – Island/Hole Generation by Pressure Quenches .....	88
8.2 – POSTFLIGHT DATA DELIVERABLES .....	89
8.2.1 – Data Archiving .....	89
8.2.2 – Data Interpretation.....	89
<b>9 – REFERENCES.....</b>	<b>90</b>

## LIST OF TABLES

Table 4.1	Flight Experiment Tests .....	53
Table 5.1	Science Requirements Summary .....	57
Table 7.1	Test Matrix for Initial Setup: island generation sequence .....	79
Table 7.2	Test Matrix for Initial Setup: droplet generation sequence .....	80
Table 7.3	Test Matrix for Experiment 1 .....	82
Table 7.4	Test Matrix for Experiment 2 .....	84
Table 7.5	Test Matrix for Experiment 3 .....	86
Table 7.6	Test Matrix for Experiment 4 .....	87

## LIST OF FIGURES

Figure 1.1	Typical liquid crystal molecules and phases .....	5
Figure 1.2	Depolarized reflected light microscopy setup .....	5
Figure 1.3	Topological defect annihilation .....	6
Figure 1.4	Observation of transverse and longitudinal polarization .....	6
Figure 1.5	Surface $\pi$ -walls in an achiral smectic C film .....	7
Figure 1.6	Field-induced fracture of the smectic C director field .....	7
Figure 1.7	Field-induced orientational solitons in a chiral smectic C film .....	8
Figure 1.8	Soliton rings on an FLC film .....	9
Figure 1.9	Nematic and smectic textures of bola-amphiphilic liquid crystal films .....	9
Figure 1.10	Layer-director structures of chiral smectic CP phases of bent-core molecules .....	10
Figure 1.11	Polarization splay modulation of the <b>B7</b> banana phase .....	11
Figure 1.12	Annihilating (+1,-1) defect pair in a high polarization smectic C film .....	11
Figure 1.13	Permeation of smectic films .....	12
Figure 1.14	Bursting smectic bubble .....	12
Figure 1.15	Simulation of nanosegregation of the azo-dye <b>7AB</b> in a smectic solvent .....	13
Figure 1.16	Bulk atomistic simulation of the anticlinic phase of <b>MHPOBC</b> .....	13
Figure 1.17	Free energy of hard spherocylinder smectic vs. interlayer tilt orientation .....	14
Figure 1.18	Simulations of hard spherocylinder bent-core systems .....	15
Figure 2.1	Islands on smectic flat films and bubbles .....	17
Figure 2.2	Setup for generating and observing smectic bubbles and islands .....	18
Figure 2.3	Island dispersion and sedimentation on a smectic bubble .....	19
Figure 2.4	Interface dynamics of one and two layer films .....	20
Figure 2.5	Force curve between two smectic C islands measured using laser tweezers .....	21



Figure 2.6	Island chaining vs. enantiomeric excess in a chiral smectic C film .....	21
Figure 2.7	Interacting arrays of isotropic droplets on FSLC films .....	22
Figure 2.8	Chaining of isotropic droplets .....	22
Figure 2.9	Island interaction force vs. enantiomeric excess in a chiral smectic C film .....	23
Figure 2.10	FSLC islands generated by inkjet printing .....	23
Figure 2.11	Schematic of a pore in a smectic film .....	23
Figure 2.12	Sketch of FSLC film meniscus structure .....	24
Figure 2.13	Interferometric measurement of FSLC film meniscus thickness .....	25
Figure 2.14	Film tension vs. thickness .....	25
Figure 2.15	Critical radius for growth of a dislocation loop on an FSLC film .....	26
Figure 2.16	Pendant pore in a FSLC film .....	27
Figure 2.17	Line tension vs. film thickness for <b>8CB</b> .....	28
Figure 2.18	Schematic structure of smectic edge dislocations .....	29
Figure 2.19	Pore radius vs. time for <b>8CB</b> films .....	30
Figure 2.20	Dislocation motion constant $C$ vs. film thickness .....	31
Figure 2.21	Topological defect near an island in a SmC film .....	35
Figure 2.22	Chaining of islands on a SmC film .....	35
Figure 2.23	Island interaction on a SmC film .....	36
Figure 2.24	Quadrupole arrangement of islands and defects .....	36
Figure 2.25	Flow of a fluid spherical shell .....	38
Figure 2.26	Mobility of a particle on a fluid spherical shell .....	38
Figure 2.27	OASIS experimental concept .....	48
Figure 5.1	Setup for macro video observation of the bubble .....	66
Figure 5.2	Schematic of air jets for island generation .....	67
Figure 5.3	Model optical reflection spectra of SmA film .....	69
Figure 5.4	Optical reflectivity of a SmA film measured by color CCD camera .....	69

**OBSERVATION AND ANALYSIS OF SMECTIC ISLANDS IN SPACE****NOMENCLATURE**

## SYMBOLS

$1D$	-	one dimensional	$p$	-	polarization density
$2D$	-	two dimensional	$P$	-	pressure
$3D$	-	three dimensional	$P(\mathbf{r})$	-	polarization field
$a$	-	excess surface entropy	$\Pi$	-	disjoining pressure
$\mathbf{b}$	-	molecular bow director	$r$	-	defect separation
$\mathbf{c}$	-	c-director	$r_b$	-	radius of bubble
$d$	-	layer spacing	$r_i$	-	radius of island
$\mathbf{E}$	-	electric field	$\rho$	-	ratio of film area to perimeter
$F$	-	dissipation function	$R$	-	radius of tethering needle
$g$	-	permeation coefficient	$Re$	-	Reynolds number
$G$	-	Gibbs free energy	$\mathcal{R}$	-	reflectivity
$\gamma$	-	surface tension	$S$	-	in-plane shear rate
$h$	-	film thickness	$\Sigma$	-	vorticity
$\eta$	-	viscosity	$t$	-	time
$k_B$	-	Boltzmann's constant	$T$	-	temperature
$K$	-	Frank elastic constant	$\tau$	-	film tension
$\kappa$	-	thermal diffusivity	$v$	-	fluid velocity
$Ma$	-	Marangoni number	$\xi$	-	length
$n$	-	refractive index			
$\mathbf{n}(\mathbf{r})$	-	director field			
$N$	-	number of layers			

## SCIENTIFIC ACRONYMS

$DRLM$	-	Depolarized Reflected Light Microscopy
$LC$	-	Liquid Crystal
$FLC$	-	Ferroelectric Liquid Crystal
$SmA$	-	Smectic A liquid crystal phase
$SmC$	-	Smectic C liquid crystal phase
$FSLC$	-	Freely Suspended Liquid Crystal

**NOMENCLATURE (Continued)***TECHNICAL ACRONYMS*

BC	-	Bubble Chamber
AFC	-	Auxiliary Fluids Container
ETM	-	Equipment Transfer Module
LMM	-	Light Microscopy Module
MSG	-	Microgravity Science Glovebox
BGMS	-	Bubble Generation and Motion System
MDV	-	Macro-view Digital Video
$\mu$ DV	-	Micro-view Digital Video
SPEC	-	Spectrometer
IDD	-	Inkjet Drop Dispenser

*ADMINISTRATIVE ACRONYMS*

GRC	-	Glenn Research Center
SRD	-	Science Requirement Document
SCR	-	Science Concept Review
ISS	-	International Space Station
PI	-	Principal Investigator
UCB	-	University of Colorado at Boulder

## OBSERVATION AND ANALYSIS OF SMECTIC ISLANDS IN SPACE (OASIS)

### EXECUTIVE SUMMARY

The *OASIS Science Requirement Document* describes a series of experimental and theoretical studies of the interfacial and hydrodynamic behavior of freely suspended liquid crystal (FSLC) films. FSLC films are formed from rod-shaped molecules that self-organize as bulk materials into fluid smectic LC phases: periodic stackings of layers in which each layer is a two dimensional (2D) fluid on the order of a molecular length in thickness. FSLC films exhibit a combination of physical characteristics that have made them uniquely exciting systems for the study of equilibrium and out-of-equilibrium phenomena in reduced dimensionality, for example liquid crystal ordering and fluctuations in two dimensions, and the effects of finite size on liquid crystal phase transitions. Here we show that FSLC films in microgravity present extraordinary opportunities for the study of fluid dynamic and thermodynamic behavior in reduced dimensionality, and for the exploration of fundamental nonequilibrium fluid interfacial phenomena.

The key relevant FSLC film properties are as follows: (i) The smectic layering forces FSLCs to be quantized in thickness in integral numbers of layers (the layer number) and suppresses pore formation and bursting. This enables the formation in air of stable single-component, layered, fluid, FSLC films as thin as a single molecular layer (~3 nm thick). (ii) The low vapor pressure of smectic-forming compounds enables the long term stabilization of these films, such that a given few layer thick film can be studied in the laboratory for many months. Such films are structures of fundamental interest in condensed matter physics. They are the thinnest known stable condensed phase structures and have the largest surface-to-volume ratio of any condensed phase preparation, making them ideal for studies of fluctuation and interface phenomena. (iii) The LC layering makes films of uniform layer number highly homogeneous in basic physical properties such as thickness, surface tension, and viscosity, and, away from the edges of the film, completely free of local pinning or other external spatial inhomogeneities. (iv) The interactions which are operative in liquid crystals are generally weak, leading to the easy manipulation of order by external agents such as applied fields and surfaces, and to significant fluctuation phenomena with extended spatial correlations. These fluctuation, field, and surface effects, combined with the wide variety of LC order parameters and symmetries, makes FSLC films a rich system for probing basic fluid physics.

We present here the results of ground-based experiments on planar and spherical-bubble FSLC films, carried out both to illustrate the possibilities for microgravity study and to develop microgravity experiments. Spherical-bubble FSLC films tethered on fine needles can be made with very small ratios of film area to perimeter, yielding systems in which coupling to the bulk fluid is extremely weak.

These ground-based experiments motivate the proposal of a variety of microgravity studies using the tethered bubble geometry. The proposed experiments will be carried out on bubbles formed and studied in situ in dedicated sample chambers in the Microgravity Science Glovebox (MSG) of the ISS. Sample chambers will be equipped for the following functionalities and experiments: (i) Automated bubble inflation to a selected size. (ii) Bubble positioning. (iii) Using gas jets tangent to (but not contacting) the bubble surface, and tether meniscus heating to generate and study in-plane flow and pull material from the meniscus, generating islands (circular domains with extra layers) on the film. (iv) High-resolution and low-resolution imaging of the bubble in reflected light to observe bubble flow and dynamics, and coarsening of island emulsions. (v) Elec-

trodes and local heaters near (but not contacting) the bubble for local application of electric field to the film surface, and for the study of thermocapillary effects. (vi) Optical measurement of film thickness. (vii) Inkjet deposition of isotropic droplets onto the bubble for the study of droplet interactions. (viii) Temperature control to study the effects of LC phase behavior. (ix) Study of weak interactions between islands and droplets.

Microgravity experiments will be pursued with the following objectives:

Detailed tests of theories of hydrodynamic flow, of relaxation of hydrodynamic perturbations, and of hydrodynamic interactions in 2D will be made. Freely suspended bubbles in microgravity, without islands, convection, and sedimentation represent nearly ideal, physically and chemically homogeneous 2D fluid systems for the precision study of 2D hydrodynamics. The effects of introducing islands or droplets will be studied, both as controllable inclusions that modify the flow and as markers of flow.

A second goal will be to study the behavior of collective systems of 1D layer step interfaces on 2D bubble surfaces, including the equilibrium spatial organization and interaction of islands, and the nonequilibrium coarsening dynamics of island emulsions. In addition to yielding information about a number of relatively weak physical effects (thickness-dependent surface tension and line tension, disjoining pressure, etc.), we anticipate that this will clarify the effects of dimensionality in coarsening dynamics (e.g., on dynamic scaling behavior).

Additionally, we will study interactions between islands and droplets in regimes where they are very weak, in the smectic A phase and at high temperature in the smectic C phase.

We will carry out the first thermocapillary experiments on homogeneous two dimensional fluids. The proposed microgravity experiments present a unique opportunity to explore thermocapillarity, the translational symmetry of the films and the absence of convection mitigating anomalous effects to the maximum extent possible, enabling detailed studies of the thermocapillarity of 2D fluids.

We will study the dependence of surface tension and line tension on film thickness and Burgers vector. Ground-based experiments indicate that equilibrium and nonequilibrium island behavior should be sensitive to this dependence, enabling critical tests of extant theoretical predictions.

We will probe the effects of a spontaneously broken symmetry in the 2D film surface (the appearance of 2D polar, XY-like ordering and accompanying electrostatic polarization) on the interaction of islands, exploring the stability of topologically stabilized emulsions of 1D interfaces in 2D.

## 1 – INTRODUCTION & SCIENCE BACKGROUND

### 1.1 – BACKGROUND AND RESEARCH CONTEXT

#### 1.1.1 – THERMOTROPIC SMECTIC LIQUID CRYSTALS

Smectic liquid crystals are phases formed by rod-shaped molecules organized into one-dimensionally (1D) periodic arrays of layers, each layer being on the order of a molecular length thick. In the fluid smectic phases, the smectics A and C (SmA and SmC), for example, each layer is a two dimensional (2D) liquid, with only short-ranged positional pair correlations within the layer planes and from layer to layer in the direction parallel to the layer planes. **Figure 1.1** shows schematically the structure of these phases and several representative liquid crystal (LC) molecules. These phases are, in general, thermotropic, appearing in single molecular component systems (or in mixtures) only over certain temperature (T) ranges. The fluid smectic phases are typically found in the range  $0^{\circ}\text{C} < T < 200^{\circ}\text{C}$ . In addition to these in-plane fluids, there are a variety of more ordered, 2D hexatic and crystalline phases having various degrees of short, quasi-long range, and long range orientational and/or translational order within and between the layers [1].

The interactions which are operative in liquid crystals are generally weak in comparison to those in crystalline phases, leading to the facile manipulation of the order and structure of liquid crystals by external agents such as applied fields, surfaces, and flow. Thus liquid crystals are the classic materials with soft degrees of freedom, and the first soft materials to be studied in the context of condensed matter physics [2].

#### 1.1.2 – FREELY SUSPENDED LIQUID CRYSTAL FILMS

The modern study of freely suspended thermotropic smectic films was begun in 1973, with the discovery by the PI and coworkers that films of fluid smectics as thin as two molecular layers (thickness,  $t \sim 6$  nm) could readily be made by coating the edge of a hole in a thin plate and drawing a

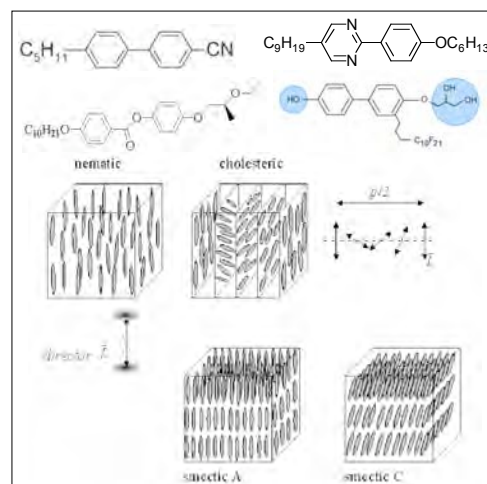


**Figure 1.1:** Examples of some molecules that form liquid crystals, along with sketches of the four most common liquid crystal phases.

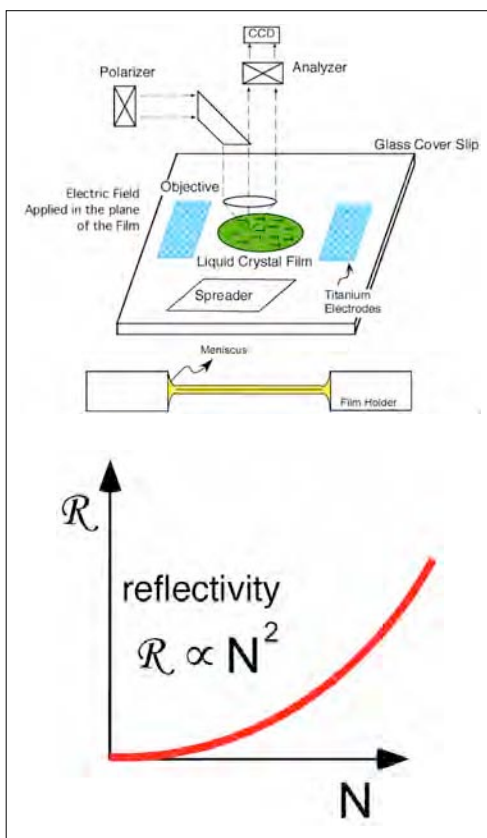


**Figure 1.2:** (top) Laboratory setup for making planar freely suspended smectic liquid crystal films. The spreader is used to draw the film over a hole in a flat thin plate. Observation in reflected light visualizes variations in film thickness and the molecular orientation field across the film. Electrodes enable the film response to in-plane electric field to be studied. The cross section shows the homogeneous film, stabilized in thickness by the smectic layering connecting to bulk LC in the meniscus. (bottom) The optical reflectivity  $\mathcal{R}$  of thin smectic films increases quadratically with layer number  $N$ .

**Figure 1.3:** (a) Annihilating +1 and -1 topological defects imaged by depolarized reflected light video microscopy, showing automated tracking of the defect centers. (b) Plot of defect separation  $r(t)$  vs. time, extracted from the video records, with  $t = 0$  corresponding to a defect separation of  $38 \mu\text{m}$ . The solid gray curve is  $dr/dt \sim K/\eta(1/r)$ , the deterministic prediction given  $K/\eta$  measured from  $dr/dt$  at  $t = 0$ . However, the approach for  $t > 0$  is slower than this prediction for nearly all observed trajectories. Similar behavior is observed for all other starting separations. (c) The effective  $K/\eta$  decreases with separation as  $\log(r)$ , showing that the rate of approach of annihilating defects becomes progressively slower than deterministic as  $r$  decreases.

film across the hole with a second plate [3]. The process and resulting structure is sketched in **Figure 1.2**. The inherent smectic fluid layering on the one hand enables such films to be drawn, and on the other hand stabilizes their structure, enabling films as thin as a single molecular layer be made and studied [4]. The smectic layering allows only films that are an integral number  $N$  layers thick, quantization that ensures that a film of a particular number of layers will be physically homogeneous with respect to its layer structure over its entire area. Measurement of optical reflectivity,  $\mathcal{R}$ , enables the determination of the number of smectic layers, as indicated in **Figure 1.2**. Film stability is further enhanced by the absence of any solvent and by component molecular weights typically in the range  $200 < \text{MW} < 400$  Daltons, which make the vapor pressure over the films quite low. In laboratory experiments, individual two-layer films can be routinely studied for periods of several months.

Since their discovery, ultrathin FSLC films have been a continuous wellspring of new liquid crystal physics, providing a unique experimental context for the study of phase behavior, fluctuations, elasto-hydrodynamics, and interfacial effects in 2D. They are the only system in which the hexatic has been unambiguously identified as a phase of matter [5], and the only physical system in which fluctuations of a 2D XY system and Kosterlitz-Thouless phase transition has been observed [6], and 2D XY quasi-long range order verified [7]. Smectic films have enabled the precise determination of smectic layer electron density and positional fluctuation profile [8] and have been used to show that the interlayer interactions in antiferroelectric tilted smectics do not extend significantly beyond nearest neighbors [9]. FSLC films played a pivotal role in the recent discovery of macroscopic chiral-polar ordering in fluids of achiral molecules [10]. In ultrathin FSLC films, effects arising from weak LC ordering are significantly enhanced, as intermolecular coupling is effectively further reduced by loss of neighbors.

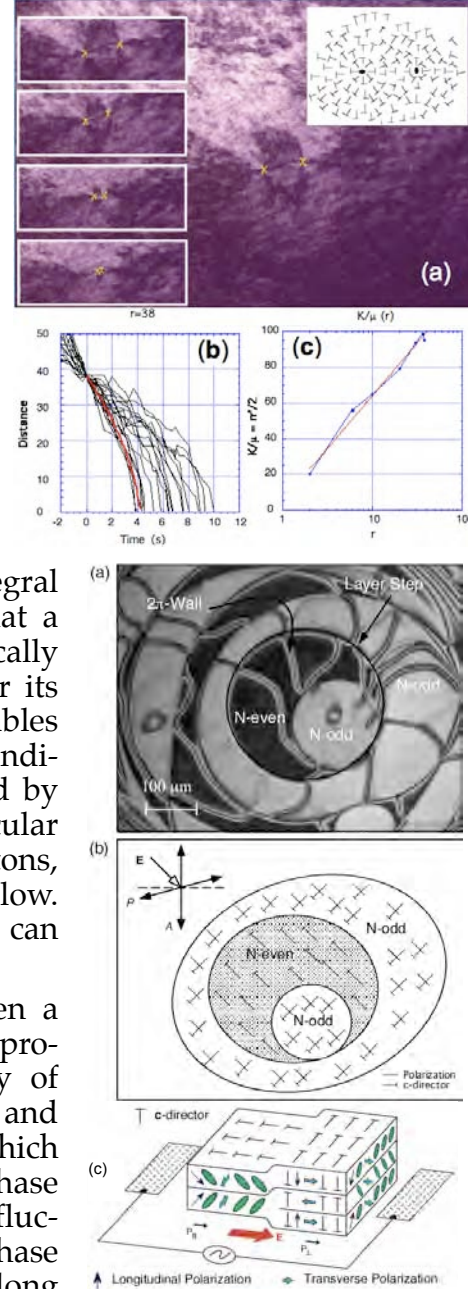


**Figure 1.4:** DRLM observation of in-plane film polarization. (a) DRLM photomicrograph showing longitudinal polarization in even layer number regions and transverse polarization in odd layer number regions. (b) Schematic of the tilt direction and polarization in (a). (c) Even layer number films have longitudinal polarization (in the tilt plane), whereas odd layer number films have transverse polarization (normal to the tilt plane). From [13].



## 1.2 – PRIOR GROUND-BASED RESEARCH: EXAMPLES OF FSLC PHYSICS

Under NASA and NSF support, our research on FSLC films has produced a host of exciting new discoveries and unexpected results, confirming the position of the study of FSLC structures as one of most exciting and fruitful areas of complex fluid physics. The principal experimental technique employed in our work is depolarized reflected light microscopy (DRLM), which we have shown is a powerful tool that can be used to explore a range of interesting 2D physics questions, including the stability and dynamics of interfaces, the formation and evolution of topological defects, the identification and elucidation of new polar phases and of metastable structures not observed in the bulk, and laser tweezing of fluids in 2D. Experimental discoveries have been complemented by theoretical models and computer simulations aimed at exploring the origins of behavior in films and bubbles. Some examples of the exciting science that has emerged from our ground-based research on smectic films are highlighted below.

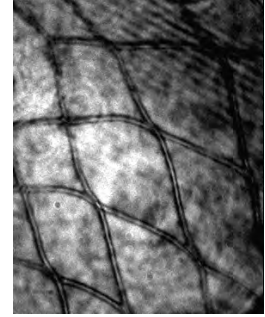


**Figure 1.5:** Two sets of field-induced  $\pi$ -walls on opposite smectic C film surfaces. The film is achiral but still has surface polarization which couples to the field.

### 1.2.1 – FORMATION AND COARSENING DYNAMICS OF TOPOLOGICAL DEFECTS IN 2D

We have studied the attraction and annihilation of pairs of topological defects of opposite strength in two-layer thick, freely suspended smectic C films. Many  $(+1, -1)$  pairs are generated in quenches (from the smectic C to the smectic A and back), achieved by rapidly collapsing a free film bubble from spherical to planar shape. The defects annihilate in pairs until there are only two defects left. These last two are observed via reflected light microscopy. **Figure 1.3a** shows a typical pair of annihilating defects. For several such events, the separation  $r$  vs. time is measured and data for a series of events is used to find the average collapse rate  $dr/dt$  as a function of  $r$ . These data are shown in **Figure 1.3b**. The results are surprising. Current theoretical models of the annihilation process assume that the defects undergo diffusive Brownian motion while attracting via a two dimensional coulomb  $(1/r)$  force [11, 12]. This predicts that at a given separation, the rate of approach,  $dr/dt$ , should behave as  $1/r$  so that  $r(dr/dt) = \text{constant}$ . However our experiments show a clearly different behavior, with  $dr/dt \sim (1/r)\log(r)$ . This observation indicates that the current theoretical understanding of the fluctuation behavior of topological defects, a problem of fundamental interest with wide ranging implications in statistical physics (for example, in describing the physics of vortex motion in superconductors and the kinetics of the early universe [11]) is flawed. We have developed pattern recognition and tracking software to identify topological defects and automate the determination of their positions as a function of time. A typical set of analyzed images is shown in **Figure 1.3a**.

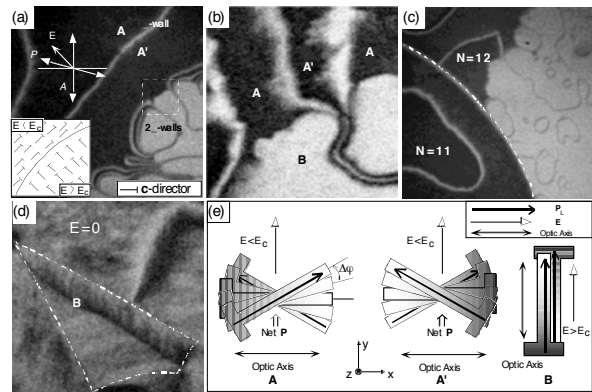


**Figure 1.6:** (a-d) DRLM photos showing orientation fracture [white areas in (a-c)] induced by electric field coupling to the surface polarization. (d) Metastable fracture domain persisting after field removal, indicative of a metastable anticlinic interface in this (synclinic) SmC phase. (e) Schematic of the orientational fracture [17].



images is shown in **Figure 1.3a**.

### 1.2.2 – USING FREE FILMS TO ELUCIDATE NOVEL STRUCTURES

We have obtained a very beautiful result in freely suspended films of the antiferroelectric liquid crystal material **MHPOBC**, demonstrating the first unambiguous evidence for longitudinal ferroelectricity in a liquid crystal and, at the same time, developing a technique for distinguishing ferroelectric from antiferroelectric ground states in tilted smectic phases [13]. **Figure 1.4** sketches the experiment, showing a portion of a freely suspended film, incident and reflected light to probe the orientation of the molecular tilt direction in the film plane, electrodes for applying an electric field in the film plane, and sections of the film where it is two and three layers thick. Where the film has an even number of layers, the surface-induced polarizations give a net polarization in the direction of the molecular tilt, and the single-layer transverse polarizations due to chirality cancel. As a result, in an applied electric field the tilt direction aligns parallel to the field. However, where the film is an odd number of layers thick, the surface polarizations cancel while the transverse polarizations do not, adding to give the net polarization of a single layer. **Figure 1.4c** shows the orientation of the resulting polarization and tilt direction in an applied field, with the tilt direction (indicated by a “T”) normal to the polarization (indicated by a “→”) for an odd number of layers, and parallel to the polarization for an even number of layers. With appropriate optics, the two tilt orientations can be visualized as dark and bright in reflected light (**Figure 1.4b**). The image in **Figure 1.4a** shows a reflected light micrograph of such a film in an applied field. This discovery enables the measurement of longitudinal polarization and a detailed comparison of longitudinal and transverse liquid crystal polarizations.

We have used this technique in a variety of ways, establishing, for example, that the ground state of the bent-core phases is antiferroelectric [13,14], and showing that the so-called “thresholdless antiferroelectric” tilted smectic phase is actually a ferroelectric smectic C [15]. This work was extended to exploit electric field coupling to ferroelectric surface ordering in achiral freely suspended films [16,17]. In a smectic C film, the molecules are tilted, yielding ferroelectric order at the surface. The uniform tilt through the film yields *opposite polarization on the two surfaces*. With the application of an electric field, these polarizations flip to be along the field, some regions going clockwise and others counterclockwise. Such opposite rotation produces line defects where the polarization rotates rapidly through  $\pi$  radians called “ $\pi$ -walls”. These  $\pi$ -

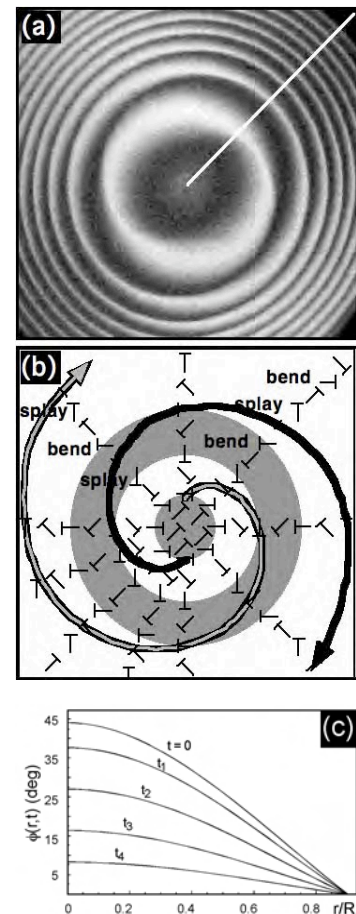


**Figure 1.7:** Soliton rings formed by a rotating electric field. **(a)** As the field rotates each soliton moves toward the film center with a velocity that varies with  $E$  as  $1/E^2$ . **(b)** A fully developed ring pattern with the field removed involves both splay and bend of the orientation field. The splay elastic constant is larger, making the rings wider in the splay regions. **(c)** Net director winding in units of  $2\pi$  turns vs. fractional radial position on the film in units of the film radius for various times showing relaxation of the ring pattern when the  $E$  field is removed. The solid curves are fits to the orientational diffusion equation. From [18].

walls form an interesting pattern on the surface of the film. There are two sets of weakly-interacting walls, one set on each surface, as shown in **Figure 1.5**. This interesting observation enables us to measure the surface polarization and elastic coefficients.

This line of research yielded two novel and unexpected LC phenomena. We found that the tilt orientations on the film surface become anticlinic at high temperatures where the film interior is SmA [16]. Thus, the tilted layers on the two surface of a non-tilted film interact to favor opposite orientation. A variety of possible explanations for this effect have been considered, including van der Waals interactions and fluctuation confinement, but the reasons for the anticlinic ordering remain mysterious. Additionally, by applying a sufficiently large electric field we were able to apply a torque to the orientation field large enough to fracture it [17], yielding, in an achiral SmC film (where the molecular tilts at equilibrium are synclinic – in the same direction – in adjacent layers), a single interface above and below which the molecules tilt in opposite directions, as illustrated in **Figure 1.6**. This interface is metastable, persisting for several minutes after the field is removed, showing that there is a metastable minimum at the anticlinic orientation in the interlayer orientational potential energy.

### 1.2.3 – ORIENTATIONAL SOLITONS IN 2D

The combination of fluidity and local anisotropy which characterizes ferroelectric SmC\* films is effectively probed by application of an in-plane electric field  $E$ . Particularly interesting is the response when the field rotates in the film plane. In this case the tilt direction reorients along with the field in the film center but is pinned with fixed orientation at the film edge, necessitating the formation of an orientational soliton with each  $2\pi$  rotation of the field, as shown in **Figure 1.8**. The solitons reflect the film shape, forming rings on a circular film as in **Figure 1.7a**. The characteristic spacing of the solitons depends on the applied field strength. The solitons move toward the film center with a velocity that increases with applied field strength [18]. With the field removed, the ring patterns provide a useful probe of the LC elastic anisotropy, the rings being wider in regions where the deformation having the larger elastic constant is dominant (**Figure 1.7b**). The orientational diffusion constant can also be measured by observation of the relaxation of the ring pattern (**Figure 1.7c**).

### 1.2.4 – ELUCIDATION OF INTERLAYER ORIENTATIONAL ORDERING IN NOVEL SMECTIC PHASES

In the late 1990s, C. Tschierske of the University of Halle pioneered the development of bola-amphiphiles, small molecules (biphenyl derivatives) which have hydrogen bonding groups at the ends of the core where conventional liquid crystals have aliphatic tails

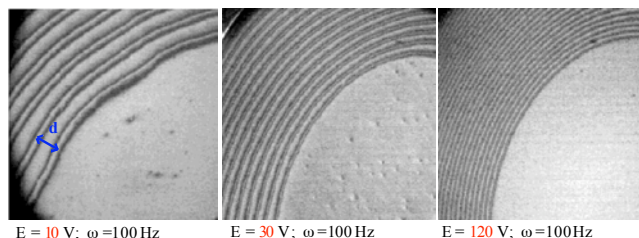


**Figure 1.8:** Soliton rings formed by a rotating electric field  $E$ , each soliton moving toward the film center with a velocity that varies as  $1/E^2$  [18].

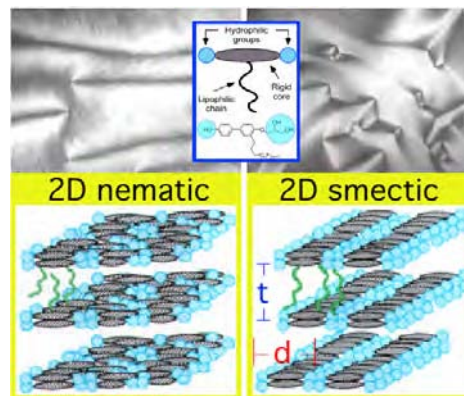


**Figure 1.9:** (top) 2D nematic (high temperature) and smectic (low temperature) textures in few-layer thick freely suspended films of the bola-amphiphilic mesogen of the family shown [19]. (bottom) Schematic representation of the molecular organization of the phases.

[19], and an aliphatic tail connected to the side of the core. These materials form layered lamellar phases where the core long axes lie parallel to the lamellae, offering the possibility of significant 2D ordering in the layer plane. We made the first freely suspended films of such materials and used the film technique to complement Tschierske's x-ray and bulk textural methods to determine phase structure. Although in the beginning it was not clear that such materials would even make freely suspended films, it turned out that it was possible and quite interesting. The nature of the 2D in-plane ordering is clearly discernible from the film textures in **Figure 1.9** which show two fluid phases: a lower temperature phase which exhibits a 2D focal conic texture indicative of in-plane smectic ordering, and a higher temperature phase which is 2D nematic, exhibiting orientation fluctuations reminiscent of the c-director fluctuations in freely suspended smectic C films. It is important to note that the in-plane director field in films of bola-amphiphiles is nonpolar, i.e., it can support  $\pi$  disclination points, several of which are evident in **Figure 1.9**, whereas the orientation field of tilted smectics has topological defects of even multiples of  $\pi$  only.

### 1.2.5 – IDENTIFICATION OF NOVEL POLAR SMECTIC PHASES

**Chiral Phases from Achiral Molecules: Pasteur's Experiment in a Fluid** – Freely suspended film studies played a crucial role in our discovery of macroscopic chiral domains in a fluid phase of achiral molecules. Our observation follows a line of study of the relationship between macroscopic and molecular chirality that was begun by Pasteur in 1848. He found that crystals of a molecularly chiral salt of "racemic acid" existed in left- and right-handed forms, the left- and right-handed molecules spontaneously segregating into macroscopically left- and right-handed chiral crystals. There have been many subsequent observations of coexisting domains of opposite handedness crystallized from both chiral and achiral molecules in isotropic solution. However, in the 150 years since Pasteur, all observations of such spontaneous chiral segregation were made in crystal phases: ours was the first such observation in a fluid. The molecules that form the  $\text{SmCP}_A$ , first synthesized by Matsunaga [20], are bow or banana-shaped as a result of their bent core. We were able to confirm that the highest temperature LC phase, the **B2**, was tilted ( $\text{SmC}$ ) [21]. Our experiments, in particular those on freely suspended films, revealed an amazing feature of this phase missed in the earlier work: the spontaneous breaking of achiral symmetry. This results from the combined effect of the two distinct, intralayer broken symmetries shown in **Figure 1.10**: polar ordering of the molecular bows (with their arrows pointing in a particular direction, clearly a consequence of the bent shape), and molecular tilt (rotation about the arrows). This discovery suggested that a rich variety

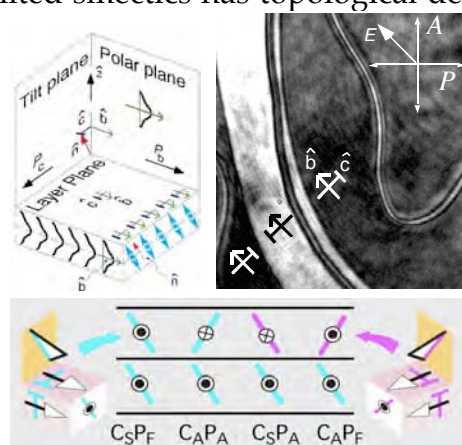


**Figure 1.10:** (left) Layer structure of the chiral phase formed from bent-core molecules, showing the achiral bent-core molecule, the polar ordering of the molecular bows along **b** and the tilt in the direction **c**, which combine to make the layer chiral. (right) Depolarized reflected light micrograph of a three layer thick, chiral freely suspended film formed from bent-core molecules, showing the bright and dark domains of opposite handedness, aligned by the in-plane field **E** to have uniform polar direction **b** but with opposite tilt directions **c**. The groups of lines are  $2\pi$  re-orientations trapped by the field. (bottom) Layer structure of the smectic CP ( $\text{SmCP}$ ) phases formed from bent-core molecules, showing the polar ordering of the molecular bows and the tilt, which combine to make the layers chiral. Here color (cyan or magenta) indicates handedness. The four indicated  $\text{SmCP}$  bilayer structures (either synclinic or anticlinic, and either ferroelectric or antiferroelectric) have all been found. From [14].



of novel structures and phases would be manifest by these molecular shapes.

**Structure of the B7 Phase: Freely Suspended Films of a Polarization-Modulated Smectic** – Our discovery of macroscopic chiral domains in a fluid phase of achiral molecules led to a variety of new freely suspended film projects directed toward developing and understanding new banana phases and structures. One of the most interesting and important has been the realization of the structure of the **B7** phase. This work began with the study of **MHOBOW**, a molecule designed with a methylheptyloxy carbonyl tail to be  $\text{SmC}_5\text{P}_F$ , the homochiral ferroelectric variant of the assembly of tilted chiral layers forming the SmCP phases shown in **Figure 1.10**. This design was, in fact, successful, with electric field application to **MHOBOW** revealing electro-optics familiar from chiral ferroelectric smectics [22]. However, before field was applied, **MHOBOW** looked nothing like the other SmCPs, growing from the isotropic as helical filaments and exhibiting amazing optical textures. Early attempts to make freely suspended films of **B7** materials failed, yielding only filaments. One of the major breakthroughs in understanding the **B7** was our development of a drawing method for **MHOBOW** that, after five years of trying, finally yielded FCLC films.

DRLM images of a typical, few-layer thick **MHOBOW** film are shown in **Figure 1.11**. Freshly-drawn films exhibit a distinctive 2D smectic texture, providing direct evidence for a 1D, pseudo-lamellar modulation of the 2D layer structure in the **B7**. The x-ray diffraction of **MHOBOW** showed that the spacing between the lamellar sub-peaks decreased with time, indicating that the modulation wavelength was increasing. **MHOBOW** has a CHN linkage that is susceptible to hydrolysis into molecular subfragments, and in the films the presence of these impurities eventually increases the modulation wavelength until it is resolvable optically. This serendipitous feature enabled us to show that the basic driving mechanism for the modulation of the polarization, sketched in **Figure 1.11**. This type of modulation reflects the inherent desire of any vector field describing ordering to splay locally, but this response is typically suppressed by the energetic cost of the defects (magenta lines in **Figure 1.11**) which are required if the majority of space is to be filled with one sign of splay. In the bent-core  $\text{SmC}_5\text{P}_F$  system, the driving force is strong enough that polarization modulation is achieved.

#### 1.2.6 – CHIRAL SMECTICS IN THE HIGH-P ELECTROELASTIC REGIME

In chiral smectics, an energetic price is paid for spatial orientational nonuniformity of  $\mathbf{n}(\mathbf{r})$ , the director field and  $\mathbf{P}(\mathbf{r})$ , the polarization field, because of Frank elasticity, and, if splay of  $\mathbf{P}$  is involved, because of the resulting  $\text{div } \mathbf{P}$  volume space charge. At high  $P$ , the latter becomes the dominant energy governing  $\mathbf{n}$ - $\mathbf{P}$  deformations and an entirely new and barely explored re-

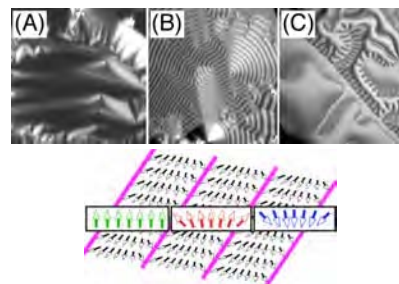


**Figure 1.11:** DRLM image of a few-layer thick **MHOBOW** film. The initial state (A) shows a 2D focal conic pattern in the film plane indicative of a 1D smectic-like, periodic in-plane ordering. With aging over several days, the wavelength of this periodicity becomes optically resolvable (B), and ultimately reveals a network of lines which define stripe domains having a preferred sign of splay (C). (bottom) Polarization splay-modulated structure of the **B7** phase. The layer organization is  $\text{SmC}_5\text{P}_F$ , homochiral and ferroelectric. The bulk polarization prefers local splay, driving the modulation. From [22].

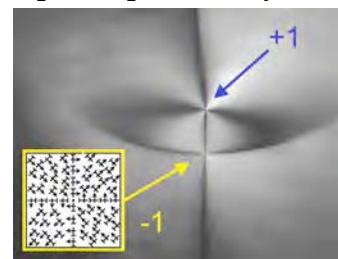


**Figure 1.12:** Annihilating +1, -1 defect pair on a high- $P$  freely suspended film of **C7**. Such structure, very different from what is expected from Frank elasticity, is determined by polarization space charge. We are pursuing its field theory and experimental study.

game of LC field behavior appears. An example is shown in **Figure 1.12**, in which a (+1, -1) pair of topological defects approach each other in preparation for annihilation. While the +1 defect appears quite normal, the -1 defect is forced by space charge to break into blocks of uniform  $\mathbf{P}$  (inset) [23]. Currently no field theory exists to describe the director in the electroelastic limit because the space charge interactions are nonlocal, and because Frank elasticity is still relevant, determining the structure of the boundaries between the orientational blocks. We continue to explore the behavior of high  $P$  films, studying annihilation and the interactions between defects.

### 1.2.7 – GAS PERMEATION OF SMECTIC FILMS

Owing to their unique geometrical properties, smectic bubbles can be used for fundamental experiments to determine material properties of smectogens, and to understand basic mechanisms of hydrodynamics in quasi two dimensional systems.

The existence of a slight overpressure (up to a few hundred Pa) inside FSLC bubbles, combined with the small membrane thickness, allows the quantitative study of gas flow through a thin liquid membrane [24]. Since the pressure difference across the membrane is directly related to the bubble radius, the gas permeability through thin liquid sheets can be derived analytically from the shrinkage dynamics of smectic bubbles. Depending on the membrane thickness, this process may take from minutes to hours for bubbles of millimeter or centimeter sizes. The shrinkage dynamics can be described by a model that considers the solubility of gas in the liquid and the diffusion coefficient in the film. Data for air permeation through a film of **DOBAMBC** are shown in **Figure 1.13**. The film becomes practically impermeable in low temperature phases (e.g., smectic I) with in-plane lattice order. The different permeation coefficients of different gases (helium, for instance, has an extremely large permeability) allows in principle the separation of gas mixtures.

Measurements of the inner excess pressure vs. bubble size provide straightforward access to the surface tension  $\gamma$  of smectic materials [25]. These experiments are particularly interesting in the vicinity of phase transitions where anomalies in the temperature trend of  $\gamma$  hint at the existence of surface phase transitions. Experiments with communicating

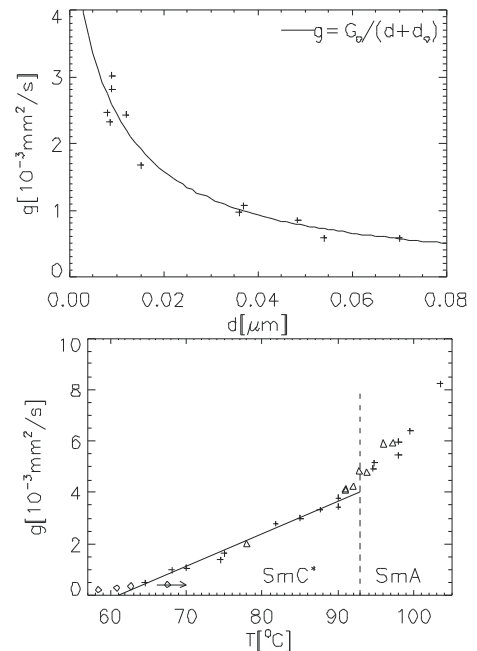


**Figure 1.13:** Permeation of air through films of the mesogenic material **DOBAMBC** as a function of film thickness  $d$  (top) at 80°C, temperature dependence (bottom) of the permeation coefficient  $g$  (from Ref. [24]).

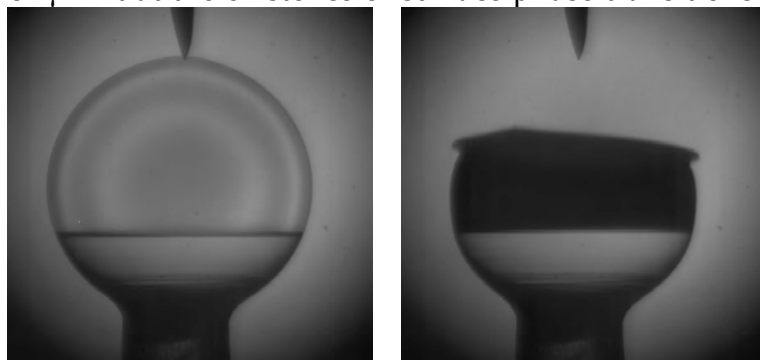


**Figure 1.14:** Rupture of a spherical bubble of a smectic A liquid crystal (**8CB**). The left image shows the initial bubble with two regions of uniform film thickness, the top with  $h = 1.4 \mu\text{m}$ , the bottom part several  $\mu\text{m}$  thick. The bubble radius is  $r_b \sim 4 \text{ mm}$ . The right image was taken 0.9 ms after initiation of the burst. The darkened appearance is due to the propagation of mechanical (peristaltic) waves.

bubbles [25] provide the most precise technique to compare surface tensions of different materials and to obtain relative surface tension data.

### 1.2.8 – RUPTURE OF SMECTIC FILMS

In addition to the studying bubbles in or near equilibrium, we have examined the rupture dynamics of thin liquid crystal films, illustrated in **Figure 1.14**, using ultrafast cameras. The key processes in film rupture and the dynamics of recessing free liquid edges were studied optically [26]. The experiments allow analysis of mechanical (capillary) waves traveling on free standing films, and tests of hydrodynamic models of film dynamics.

### 1.3 – ATOMISTIC AND COARSE-GRAINED SIMULATION OF SMECTICS

The computational component of this research has focused on improving our understanding of liquid crystal nanophysics via direct atomistic and coarse-grained simulation of molecular organization in smectics, in particular the layering in smectics and the influence of nanosegregation on molecular orientation, and the behavior of solutes in smectic films. During the past several years we have developed a variety of effective computational tools for the simulation of molecularly realistic liquid crystal models, and have begun to apply them to understanding smectic structure [27,28]. These tools include a hybrid *ab initio*/empirical force field specifically designed for modeling LC materials and special simulation techniques (multiple-timestep molecular dynamics, hybrid Monte Carlo, particle-mesh Ewald method) enabling efficient configuration-space and conformational sampling. A highly accurate force field is required because the self-organization of soft materials such as LCs is governed by the interplay of a variety of subtle energetic and entropic effects, which must be adequately quantified [29].

#### 1.3.1 – MOLECULAR NANOSEGREATION BY PHOTOISOMERIZATION

These methods have been applied to the study of solute distribution in a smectic phase, under conditions where the shape of the solute molecules, in this case the azo dye **7AB**, can be changed from linear (*trans*) to bent (*cis*) optically [30]. We find a distinctive photo-induced nanosegregation, the **7AB** intercalating between and

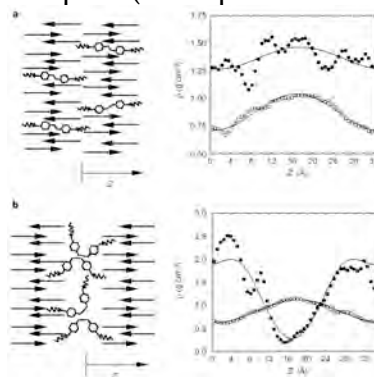


**Figure 1.15:** (left) Schematic of the nanometer scale organization of the azo dye **7AB** in a smectic solvent. (right) Mass density profiles along the layer normal for **8CB** (open circles) for a trans-**7AB/8CB** mixture (a) and for a cis-**7AB/8CB** mixture (b). In the trans state the **7AB** locates preferentially in the smectic layers, whereas in the cis state it nanosegregates between the layers. The calculated layer expansion which results matches that found in experiments. From [30].

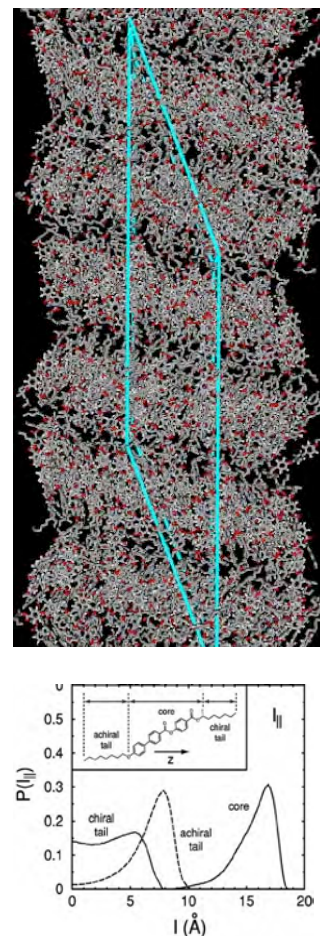
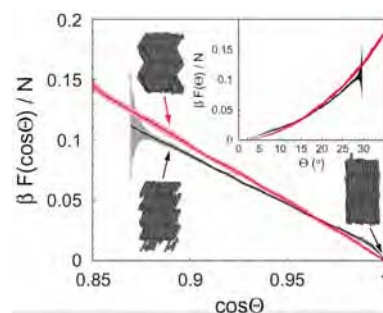


**Figure 1.16:** Bulk atomistic simulation of **MHPOBC** in the antiferroelectric phase showing its anticlinic molecular tilt in adjacent layers (top). The plot from the simulation (bottom) shows that the **MHOC** tail lies parallel to the layers, leading to reduced out-of-layer fluctuations and anticlinic, rather than synclinic, ordering.



**Figure 1.17:** Helmholtz free energy as a function of the cosine of the tilt angle for synclinic (black) and anticlinic (red) states of the hard spherocylinder system. Also shown is the free energy as a function of tilt angle (inset) for both states, and several representative configurations of the system. This energy difference favoring the synclinic state with increasing tilt is explicitly due to out-of-layer fluctuations. If these are suppressed by an additional potential, the synclinic and anticlinic curves become essentially identical. From [31].



expanding the layers upon *trans* to *cis* isomerization as indicated in Figure 1.15. Quantitative agreement with measured layer expansion indicates that the simulation accuracy enables the addressing of a variety of smectic structure issues.

### 1.3.2 – ANTICLINIC ORDERING IN SMECTICS

One of the more interesting questions in the physics of tilted smectics is the origin of the anticlinic ordering in the classic antiferroelectric material **MHPOBC** (Figure 1.16 [13]) and its homologs and derivatives that share the methylheptyloxy carbonyl (**MHOC**) tail, for example **MHOBOW**. In order to address this question and provide a basis for design of other bent core systems, we carried out simulations of **MHPOBC** directed toward understanding the organization of the tails in anticlinic phases. Figure 1.16 (top) shows a typical configuration in the antiferroelectric phase. Although not evident from this picture, statistical analysis (Figure 1.16 (bottom)) shows that the **MHOC** tail is bent by  $\sim 90^\circ$  so that it is nearly parallel to the layers. This orientation of the tail makes it energetically more costly for molecules to fluctuate out of one layer and into the next, an event that favors synclinic ordering. Thus we expect that out-of-layer fluctuations would favor synclinic ordering, which we demonstrated in the model, discussed next.

### 1.3.3 – OUT-OF-LAYER FLUCTUATIONS FAVOR SYNCLINIC ORDERING

The overwhelming majority of tilted smectic LCs exhibit synclinic ( $\text{SmC}$ ) ordering (a uniform tilt direction in all smectic layers) rather than anticlinic ( $\text{SmC}_A$ ) ordering (a tilt direction that alternates from layer to layer). We have recently proposed that polar, molecular-scale fluctuations of the interface between smectic layers provide a general entropic mechanism favoring synclinic ordering, supported by evidence from simulations of the hard spherocylinder system [31]. We find that the entropy of the synclinic state of spherocylinders with  $L/D$  ratio 5 is higher than that of the anticlinic state for large tilt angles, and show that this entropy difference can be directly traced to molecular-scale fluctuations of the layer interface (Figure 1.17). This entropic mechanism may be suppressed in materials with anticlinic ordering due to a bent molecular conformational preference that quenches interface fluctuations.

### 1.3.4 – INTERFACE CLINICITY AND ORDERING IN BENT-CORE SYSTEMS

Bent-core molecules are effectively thought of as bilayer smectic systems in which every other layer interface is chemically fixed to be a certain angle. The polymorphism of the SmCP class of smectic liquid crystals (**Figure 1.18**) arises from what happens at the other interfaces. We have begun to explore layer interfaces in bent-core systems by carrying out Monte Carlo simulations of a minimal hard-spherocylinder dimer model to investigate the role of excluded volume interactions in determining the phase behavior of bent-core materials and to probe the molecular origins of polar and chiral symmetry breaking [32]. In **Figure 1.18**, we show the phase diagram of hard-spherocylinder dimers of length/diameter ratio 5 as a function of pressure or density and dimer opening angle  $\psi$ . With decreasing  $\psi$ , a transition from a nonpolar to a polar smectic A phase is observed near  $\psi = 167^\circ$ , and the nematic phase becomes thermodynamically unstable for  $\psi < 135^\circ$ . Free energy calculations indicate that the antipolar smectic A (SmAP<sub>A</sub>) phase is more stable than the polar smectic A phase (SmAP<sub>F</sub>). No chiral smectic or biaxial nematic phases were found.

Recent experiments indicate that doping low concentrations of bent-core molecules into calamitic smectics can induce anticlinic and biaxial smectic phases [33]. We have carried out Monte Carlo simulations of mixtures of rod-like molecules (hard spherocylinders with length/diameter ratio  $L_{\text{ban}}/D = 5$ ) and bow-shaped molecules (hard spherocylinder dimers with length/diameter ratio  $L_{\text{ban}}/D = 5$  or 2.5 and opening angle  $\psi$ ) [34]. Some of the results are shown in **Figure 1.18**. We find that a low concentration (3%) of  $L_{\text{ban}}/D = 5$  dimers induces anticlinic (SmC<sub>A</sub>) ordering in an untilted smectic (SmA) phase for  $100^\circ \leq \psi < 150^\circ$ . For  $L_{\text{ban}}/D = 2.5$ , no tilted phases are induced. However, with decreasing  $\psi$  we observe a sharp transition from *intralamellar* nanophase segregation (bow-shaped molecules segregated within smectic layers) to *interlamellar* nanophase segregation (bow-shaped molecules concentrated between smectic layers) near  $\psi = 150^\circ$ .

### 1.3.5 – NANOSEGREGATION DRIVES MOLECULAR TILT AND LAYER CURVATURE

The phase behavior of the tilted smectic phases observed in freely suspended films has made it clear that many surprises are in store in the study of the interlayer organization of smectics. Coarse-grained and atomistic simulations of calamitic and bent-core liquid crystals show that nanophase segregation is a unifying concept that can explain a wide range of phenomena in calamitic and bent-core smectics, shedding light on the molecular origins of tilt, spontaneous chirality, polarization splay, and saddle-splay layer curvature in bent-core liquid crystals. Nanophase segregation of chemically

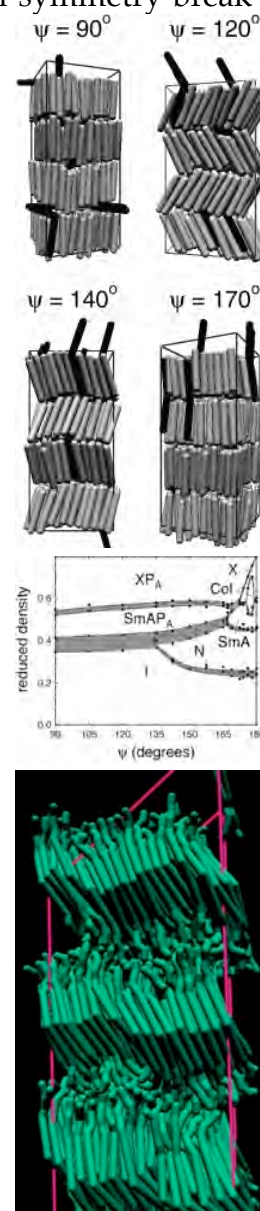


**Figure 1.18:** (top) Equilibrated configurations of the  $L_{\text{ban}}/D = 5$  system for bent-core angles  $\psi$  of  $90^\circ$ ,  $120^\circ$ ,  $140^\circ$ , and  $170^\circ$ . Banana molecules are shown in black and rods in gray. From [32]. (middle) Phase diagram of bent-core molecules of hard-spherocylinder dimers as a function of the opening angle  $\psi$ . The antipolar, untilted smectic phase is preferred, i.e., the layer interface between molecules is synclinic. From [34]. (bottom) Undulated phase of model bent-core molecules with fluid splay stripes.



dissimilar functional groups into distinct sublayers is a defining property of smectic liquid crystals. Such segregation can be driven by intramolecular variations in flexibility, intermolecular interactions, or molecular shape. We propose that nanophase segregation leads to frustration deriving from a mismatch in the preferred areal densities of distinct smectic sublayers. This “built-in” frustration can be relieved in a variety of ways. For example, frustration arising from competition between the conformational entropy of flexible aliphatic tails (which favors a relatively large area/molecule) and van der Waals attraction between rigid cores (which favors a smaller area/molecule) can be relieved by molecular tilt within the core sublayer. In a similar way, frustration deriving from nanophase segregation appears from simulations to be responsible for characteristic nanostructure formation in bent-core smectics, including polarization splay in the **B7** phase, illustrated in **Figure 1.11**, and spontaneous saddle-splay layer curvature in the dark conglomerate phase. Nanophase segregation also influences the structure and fluctuations of the interlayer interface, modifying the tilt coupling (synclinic vs. anticlinic) and polar coupling (ferroelectric vs. antiferroelectric) between adjacent smectic layers [35]. Computer simulations are helping us develop an improved understanding of the delicate coupling between molecular properties, the details of the layer interfaces, and the microscopic structure of smectics.

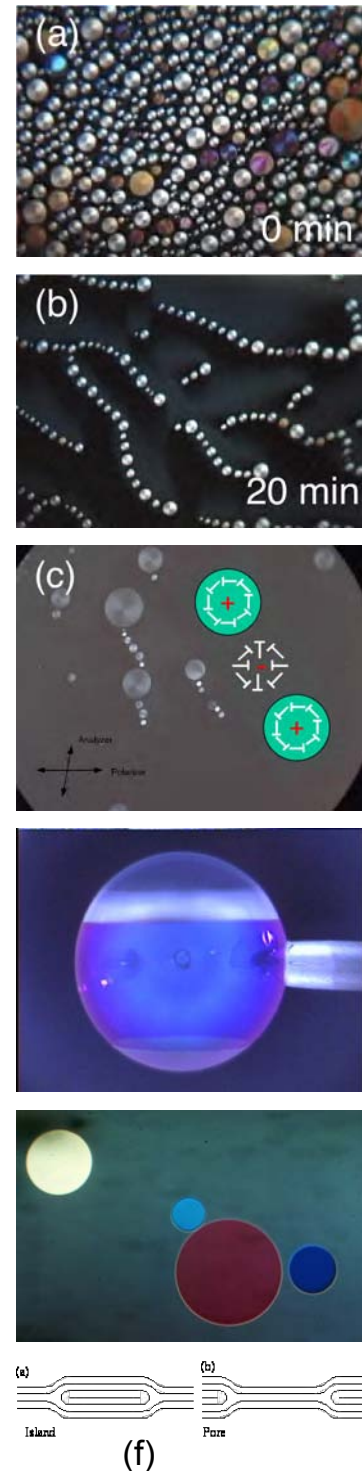
## 2 – PROPOSED MICROGRAVITY EXPERIMENTS: BACKGROUND / RELATED RESEARCH

In this section, we present: (i) the results of the ground-based research on planar and spherical-bubble (SB) FSLC films that motivated the development of the OASIS proposal; (ii) relevant theoretical background and proposed theoretical research; and (iii) a description of the proposed microgravity experiments.

### 2.1 – KEY PROPERTIES OF FREELY SUSPENDED LIQUID CRYSTAL FILMS

The key relevant FSLC film properties are as follows: (i) The smectic layering forces FSLCs to be quantized in thickness in integral numbers of layers (the layer number  $N$ ) and suppresses pore formation and bursting. This enables the formation in air of stable, single-component, layered, fluid, FSLC films as thin as a single molecular layer ( $\sim 3$  nm thick). (ii) The low vapor pressure of smectic-forming compounds enables the long-term stabilization of these films, such that a given few-layer thick film can be studied in the laboratory for many months. Such films are structures of fundamental interest in condensed matter physics. They are the thinnest known stable condensed phase structures and have the largest surface-to-volume ratio of any condensed phase preparation, making them ideal for studies of fluctuation and interface phenomena. (iii) The LC layering makes films of uniform layer number highly homogeneous in basic physical properties such as thickness, surface tension, and viscosity, and, away from the edges of the film, completely free of local pinning or other external spatial inhomogeneities. (iv) The interactions which are operative in liquid crystals are generally weak, leading to the easy manipulation of order by external agents such as applied fields and surfaces, and to significant fluctuation phenomena with extended spatial correlations. These fluctuation, field, and surface effects, combined with the wide vari-

**Figure 2.1:** (a) Array of pancake-shaped smectic islands generated on a  $\sim 1$  cm diameter smectic C bubble. (b) Island chain aggregates during coarsening process. (c) Islands have topological defect strength  $+1$  in the azimuthal tilt plane orientation field, and each one is accompanied by a  $-1$  defect in the background film. The  $-1$  defects mediate an attractive interaction between the islands. These images are  $700\ \mu\text{m}$  wide. (d) An 8 mm diameter smectic bubble tethered on a needle and viewed in reflected light. The needle edge is razor-sharp, making the Plateau border extremely thin. This and the small ratio of needle radius to bubble radius severely restricts transport of material onto or from the bubble (weak tethering limit). The horizontal bands indicate the 1D interfaces (layer steps) separating regions with different layer number  $N$ , with the thicker regions sedimenting in the 1g laboratory environment. In microgravity, the disposition of such interfaces will be determined by their mutual interactions. (e) Smectic islands ( $20\ \mu\text{m} < \text{diameter} < 100\ \mu\text{m}$ ) viewed in reflected light, illustrating the quantization of film thickness. The islands ( $20 < N < 40$ ) are thicker than the background film ( $N \sim 10$ ) and bounded by 1D interfaces where  $N$  abruptly changes. The proposed work focuses on the collective dynamics of such interfaces as a probe of the physics of capillarity in ultrathin fluid films. (f) Schematic film profiles for islands and pores. We propose to explore the physics mediating the change in layer number.



ety of LC order parameters and symmetries, makes FSLC films a rich system for probing basic fluid physics.

## 2.2 – GENERATION AND MANIPULATION OF SMECTIC LIQUID CRYSTAL BUBBLES

The inherent fluid-layer structure and low vapor pressure of smectic liquid crystals enable the long term stabilization of freely suspended, single component, layered fluid films as thin as 30 Å, a single molecular layer. Stable spherical films of low vapor pressure fluids are potentially quite interesting and useful for a variety of studies of the flow and fluctuation properties of thin fluid films. The formation and manipulation of smectic bubbles has thus been a focus of our work. Our initial studies were complicated by a geometry requiring very slow filling during the critical period when the bubble reaches its minimum radius of curvature as a hemispherical cap at the end of the hypodermic needle. Analysis of this problem indicated that we needed to minimize the gas volume behind the bubble and with this change we were able to generate smectic bubble films very easily. We have developed an apparatus, with components sketched in **Figure 2.2**, that enables us to inflate bubbles, observe them optically at low and high resolution, and manipulate them with laser tweezers, flow and electric field in our laboratory. Bubbles are inflated in a small chamber using a computer-controlled syringe. This chamber is attached to the x-y stage of an Olympus research microscope, which is used for high-resolution viewing of the tops of bubbles. All observation is in reflected light, since reflectivity  $\mathcal{R}$  is very sensitive to  $N$ , the number of layers in the film ( $\mathcal{R} \sim N^2$ ). Low-resolution observation of the entire bubble is carried out also in reflection with a macro-video camera and a hemisphere of the bubble diffusely illuminated from all directions to make its features visible.

## 2.3 – ISLANDS ON FSLC FILMS

An important class of OASIS experiments focus on the behavior of islands on FSLC films. Islands are pancake-like stacks of extra layers on an otherwise uniform thickness film, as shown in **Figures 2.1** and **2.3**.

Islands are of interest as statistical mechanical and

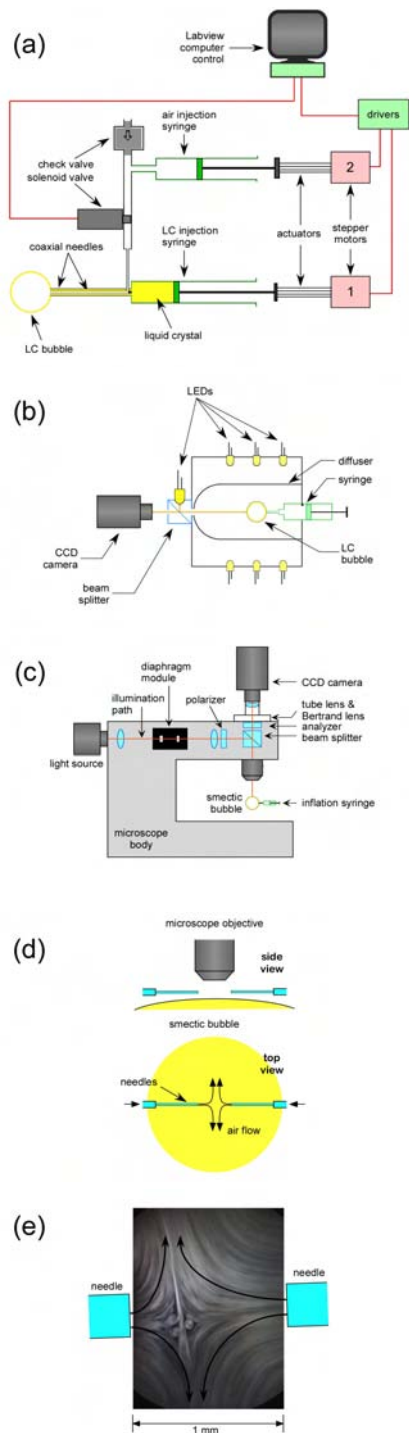


**Figure 2.2:** Experimental setup for creating, illuminating, observing, and manipulating smectic bubbles: (a) LC injection and bubble inflation; (b) Hemisphere illumination and macro reflected light videography; (c) High-resolution reflection microscopy of the top of the bubble; (d) Gas jets for setting up extensional flow of the bubble surface; (e) Rapidly moving islands enable visualization of the extensional flow of the bubble surface generated by the jets. Several islands are transiently trapped in the velocity null at the center and being stretched by the flow. The result of this process is the island emulsion of **Figure 2.1a**.

dynamical objects because of their very small mass ( $10^{-12}$  grams for a  $10\ \mu\text{m}$  diameter island), and coupling to the two-dimensional fluid film. The islands respond in a polar way to applied electric field, indicating that they are either charged or significantly more polarizable than the surrounding film. In a microgravity environment, the Perrin length,  $k_B T / mg$  for an island, will be large compared to the bubble size, meaning that in this case the islands will be thermally dispersed over the bubble surface. Interactions between islands can be modified by applying electric fields to the bubble film.

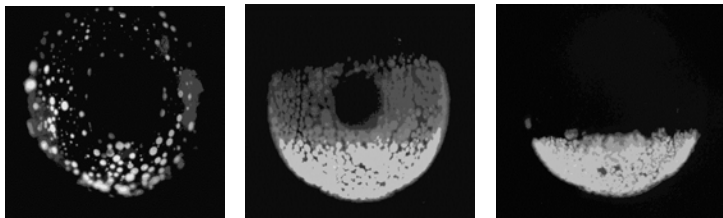


**Figure 2.3:** Islands sedimenting on a freely suspended **8CB** smectic bubble. Photographs show smectic C bubbles,  $\sim 20$  mm in diameter, viewed in reflected light. The dark parts of the bubbles are  $\sim 3$  to 5 smectic layers thick. Pancake shaped islands having additional layers are evident. The black spot in the center of the bubbles is an illumination artifact. In the bubble geometry, the ratio of the Plateau border length around the needle to the film area is very small relative to planar films. This enables the formation of island arrays by a slight decrease of internal pressure. Islands can be dispersed on the film by an air jet (**left**), but in 1 g sediment to the bottom within a few minutes (**right**).

### 2.3.1 – ISLANDS ON FSLC BUBBLES

Islands are readily generated on a tethered bubble because  $\rho$ , the ratio of film area to perimeter, is large. For the typically used planar geometry, the film perimeter is of the order of the distance across the film. For the bubble geometry, for example with a bubble inflated on a needle, the perimeter is of the order of the needle diameter, which can be 100X smaller than the film dimension (bubble radius). At the film edge is a Plateau border where the film thickens to become bulk material. Changing the area of the film produces in-plane stress but since the film can exchange material with the bulk at its edge, the stress generated is low and transient, determined by the rate of change of area and the hydrodynamics of flow into or out of the border. The small value of the ratio  $\rho$  in the bubble geometry enables much larger in-plane dynamic stress. If the surrounding gas is gently moved to produce a vorticity  $\Sigma$  in the vicinity of the bubble, then the bubble will rotate with  $\Sigma$ , nearly as a solid object. However, if a focused gas jet is brought near the film, the film begins to shear and the islands are stretched over the film surface. If the maximum in-plane shear rate is  $S$  this will lead to the tearing of the islands and the formation of smaller islands of dimension  $r_i \sim \gamma / \eta S$ , where  $\gamma$  is surface tension,  $\eta$  the shear viscosity, and  $S$  the in-plane shear rate.  $r_i$  appears to be on the order of a few microns for achievable shear rates. The result of such a process is that the film becomes a sea full of tiny floating islands (**Figure 2.1a**), which slowly coalesce (**Figure 2.1b**). The sheared films in this state behave as two-dimensional emulsions. At lower temperatures in the smectic A or C phases, the islands appear to be able to contact one another for extended periods without coalescing, a result, we suppose, of the energy barrier to elimination of the dislocation structures at their edges. The slow coalescence is also a result of the small size of the Plateau border, which inhibits loss of islands at the film edge. Initial experiments have shown that using razor-edged needles can significantly reduce the size of the Plateau border, as shown in **Figure 2.1d**. These effects of needle geometry will be investigated further.

### 2.3.2 – DYNAMICS OF ISLANDS

Islands can exhibit a fascinating collective dynamic behavior in their growth/decay, some aspects of which have recently been treated theoretically by Holyst and coworkers [36]. Consider the data shown in **Figure 2.4**, obtained in the 3M material CRL-EX-900084, which makes monolayer FSLC films [37]. Here a one-layer ( $N = 1$ ) hole in a two-layer film spontaneously decreases in size, pulling more material through the Plateau border out onto the film. This is in itself somewhat mysterious since the typical way to reduce the free energy of a film system is to move material to the bulk. However, in this case  $N = 2$  layer thick areas are the most stable. This film also has  $N = 2$  islands within the  $N = 1$  hole. The data show clearly the collective nature of the dynamics of the 1D interfaces on a 2D smectic film, with the velocity of expansion of a one-layer thick hole in a two-layer thick film changing when a growing two-layer thick island in the hole hits its edge. Non-local behavior arises because these distinct moving dislocations are competing for the same material, which must come from the Plateau border. The constant velocities suggest that line tension effects are relatively unimportant, *i.e.*, that the motion is being driven by the  $N$ -dependence of the film surface energy. We intend to generalize the Holyst model to include nested island/hole cases with  $N$ -dependent surface energies and test its applicability to this system.

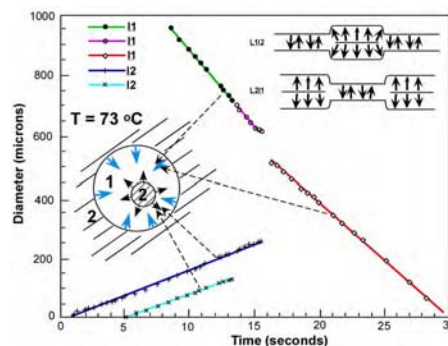


**Figure 2.4:** 1D interface dynamics in an inhomogeneous film of a fluorinated SmA. Regions two layers thick are lowest in energy and grow at the expense of one layer thick areas. Thus the 1 layer thick hole shrinks, at a constant rate (green). In the early stages it has a two layer island on it which grows at a constant rate (dark blue). When this island coalesces with the surface, the shrinkage rate of the hole abruptly changes, showing that the shrinkage or growth is a partially non-local process.

### 2.3.3 – ISLAND EMULSIONS

Swirling the bubble with an air jet generates a 2D foam of islands which is generally stable against island aggregation, a process which takes place very slowly. We show in **Figures 2.1** and **2.3** examples of two dimensional (2D) emulsions (arrays of islands) or foams (arrays of pores) on smectic films and observing their structure and dynamics. **Figure 2.2d** shows the setup for generating island emulsions. Once the bubble is inflated, a pair of opposing, sub-millimeter diameter hypodermic needles connected to pressurized gas are located within 100 microns of being tangent to the smectic sphere. These gas jets induce pure extensional, in-plane flow at a point on the bubble, with a shear rate of  $\sim 100 \text{ s}^{-1}$ , which generates a two-dimensional array of islands as shown in **Figure 2.1a**. The overall generation mechanism is not completely determined but one important process is illustrated in the inset of **Figure 2.2d**, which shows an island being pulled apart by the extensional flow. The emulsion in **Figure 2.1** is in the smectic C (SmC) phase, and is stabilized by the elastic energy of the  $c$ -director field. The  $c$ -director field is visualized by the “T” symbol, where the bar indicates the end of the tilted molecules closest to the reader. The boundary of an island imposes a  $2\pi$  reorientation of  $c$  as it is circumnavigated, trapping a  $+1$  ( $2\pi$ ) strength topological defect inside and a  $-1$  strength defect outside, as indicated in **Figure 2.1c**. This condition generates short-range repul-



sion and longer range attraction between the islands. **Figure 2.1b** shows the evolution of the emulsion on the top of the sphere (where we can currently do high-resolution imaging), showing that the density decreases as the islands sediment to the lower part of the bubble, and that at lower density the system forms island chains stabilized by topological charge alternation (+1 – 1 +1 –1 +1 –1 ...). In a microgravity environment, the islands will be thermally dispersed over the bubble surface and sedimentation will not occur.

### 2.3.4 – INTERACTION OF ISLANDS ON FSLC FILMS

We have directly measured the elastic dipolar interactions between islands on freely suspended smectic films using the multiple-trap optical tweezer technique outlined in **Figure 2.5**. The interactions between islands in non-chiral materials are surprisingly small but they increase significantly in chiral materials [38,39]. This is manifest under the microscope as an increase in the amount of spontaneous island chaining, as shown in **Figure 2.6**. The measured interaction potentials can be fitted qualitatively with two-dimensional energy curves computed assuming that the interaction is purely elastic in nature, as shown in **Figure 2.5**. Measurements of the attractive force at fixed island separation as a function of enantiomeric excess, shown in **Figure 2.7**, provide direct confirmation that the interactions increase with increasing chirality. In chiral films, the elastic constant so obtained is significantly (~10 times) greater than the values typically found in non-chiral materials, as indicated in the caption of **Figure 2.5**.

In summary, we have observed that the magnitude of the interaction force between islands is much smaller in the racemic smectic C case than in the chiral smectic C\*, an effect we attribute to long-range coulombic forces arising from polarization charges.

**Studies of Island Interactions in High Polarization Materials** – As we have shown above, the interaction force between islands on a freely suspended film depends quadratically on spontaneous polarization charge. This means that both elastic interactions and polarization charge ef-

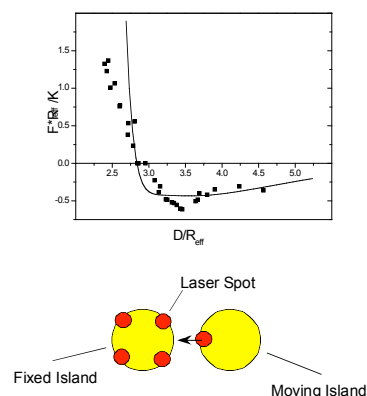


**Figure 2.5: (top)** Interaction force  $F$  between chiral smectic C\* islands on a freely suspended film as a function of island separation  $D$ . The solid line is the best fit assuming a single elastic constant and ignoring space charge effects. This measurement is for a pair of islands with average radius  $R_{ave} = 12.5 \mu\text{m}$ , 5-30 layers thick, on a 2-layer film. The 2D elastic constant is  $K = K_{3D} \cdot h$ , where  $K_{3D}$  is the bulk elastic constant and  $h$  the film thickness. The fit yields  $K_{3D} = 56 \text{ pN}$ , assuming an effective average island radius  $R_{eff} = \alpha \cdot R_{ave}$  with  $\alpha = 1.08$ . The material used is **MX8068**. **(bottom)**: Illustration of technique used to measure interaction forces between smectic islands using optical tweezers. The island on the left is fixed by four time-sharing optical traps. Another trap is used to pull the island on the right away from its equilibrium position.

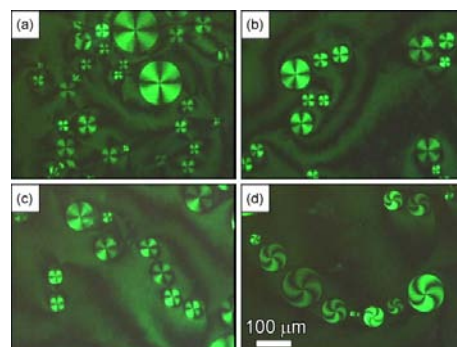


**Figure 2.6:** Microscope images, obtained in reflection between crossed polarizers, of smectic C islands of the material **MX8068**, showing typical brush textures and chaining behavior as a function of chiral mixture. **(a)** Pure racemate. **(b)** 10% chiral in racemic. **(c)** 25% chiral in racemic. **(d)** 100% chiral. With increasing enantiomeric excess we see a greater tendency for island chaining and a transformation from radial to spiral brushes within the islands.

fects have to be considered in order to model the interactions between islands.

### 2.3.5 – DROPLETS OF ISOTROPIC FLUIDS ON FSLC FILMS

In addition to islands other kinds of inclusions, such as isotropic liquid drops or solid particles, can be introduced onto FSLC films. Like islands, these objects present a specific boundary condition for the c-director field and thus interactions between such droplets are mediated by elastic forces of the field, self-organizing into spontaneous chains and lattices [40]. As with smectic islands, interactions can be ‘switched’ on and off by temperature control, heating the films into the smectic A phase (off) or cooling them to smectic C (on), so that reversible structure formation can be studied. **Figure 2.7** shows typical examples of arrays of isotropic liquid droplets on a FSLC film. In addition, boundary conditions are more flexible than for smectic islands. It is possible to generate different types of interactions by selecting specific boundary conditions of the c-director at the droplet boundaries. With appropriate materials, one may obtain radial, tangential or oblique anchoring [41]. It is even possible in some mesogenic materials to change anchoring conditions from radial to tangential by varying the temperature. Most studies reported to date have been achieved with molten mesogenic material near the clearing point [42,43]. Another option is the dispersion of solid particles on the film surface [44]. Such particles in the micrometer diameter range exhibit similar structure forming mechanisms. It has been shown that in photosensitive material (azo or azoxy chromophores), one may reversibly change the droplet density in such films, thus controlling the pattern forming process [45].

All ground-based experiments on isotropic drops have been restricted to planar smectic films. The Inkjet Drop Dispenser may be used to deposit droplets of different, immiscible li-

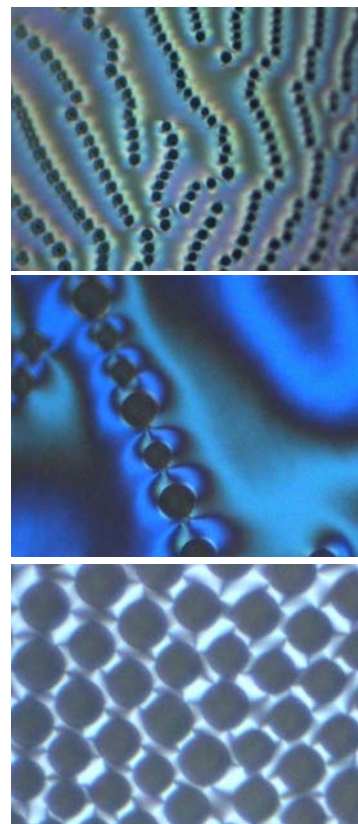


**Figure 2.7:** (top): Chains of isotropic liquid crystal droplets in a smectic C film observed without polarizers. (middle): Single droplet chain under crossed polarizers. (bottom): Hexagonal lattice of droplets under crossed polarizers. The images are approximately 200  $\mu\text{m}$  wide.

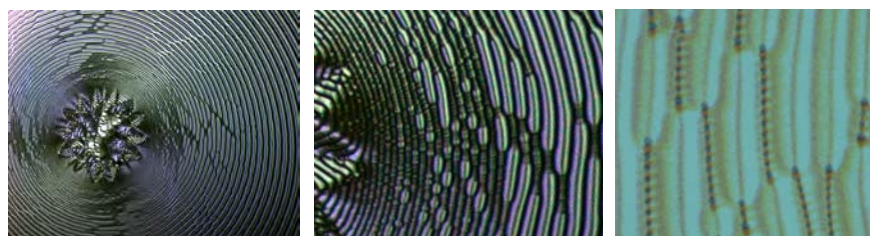


**Figure 2.8:** Arrays of droplet chains aligned by a target pattern in a FSLC film, viewed by DRLM. The **left** image width is  $\sim 2$  mm. (middle) Detail of the same image, four times magnified, with single droplets resolved. (right) Individual droplet chains in the inversion wall array.

quids on FSLC bubbles. Analysis of the structures and the dynamics of the organization process can provide fundamental insights into spontaneous pattern formation in 2D. These experiments are of particular interest for bubbles, wherein the droplets interact in a curved space. Lattices on a spherical surface [46] are of general importance and they can hardly be observed and studied under gravitation because of the interference of buoyancy with the weak elastic forces of the material. In addition to the fundamental scientific interest in such

pattern-forming phenomena, there is a potential technological impact, since such organized microstructures can be transferred onto solid substrates and photopolymerized.

### 2.3.6 – ISLAND AND DROP GENERATION VIA INKJET PRINTING

Islands generated spontaneously on films or bubbles, or those created using shear flow, show a wide range of diameters and thicknesses in any given experiment. We have nevertheless been able to study island interactions between carefully selected pairs (or clusters) of such “natural” islands that are of similar size and layer number.

With a view to generating large numbers of islands of uniform size, we have performed preliminary experiments using an inkjet printer head to deposit homogeneous droplets of low viscosity fluids on thin smectic films (**Figure 2.10a**). When drops of water, for example, adhere to the film, they nucleate new smectic islands. Liquid crystal material from the film wets the water and covers the free surface of the droplet over the course of several minutes, until the remains of the original drop (which will have shrunk by evaporation during this time) are completely covered by smectic material. Such islands are very uniform in size and interact, forming chains similar to those observed previously, as can be seen in **Figure 2.10b**. They may exhibit c-director textures that are more complex than those seen in “natural” islands (**Figure 2.10c** and **d**). We propose to continue to develop inkjet techniques as a method for delivering droplets of liquid crystal. We will investigate whether we can print small volumes of nematic or smectic material onto films in order to generate islands. To compensate for the higher viscosity of smectics, the reservoir and print head may need to be heated. It is known from work by R. Meyer and P. Pieranski that dust or smoke particles can be used to nucleate smectic islands. One of our goals is to use a relatively volatile liquid (such as water or alcohol), or liquid crystal itself, to create monodisperse islands that have no remnant impurities in them and hence will be fully equivalent in all their physical properties to “natural” smectic islands.

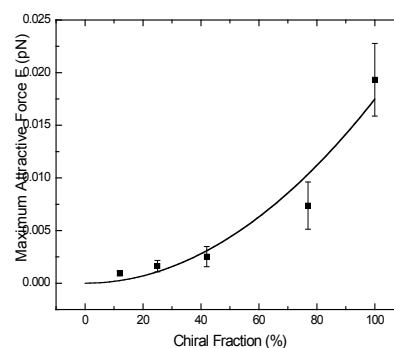


**Figure 2.9:** Experimentally measured attractive force as a function of chiral SmC\* percentage at an island separation  $D=3.5 R_{ave}$ . The solid line is the best quadratic fit to this graph.  $R_{ave}$  for the islands used in this experiment is in the range of 8-17  $\mu\text{m}$ .

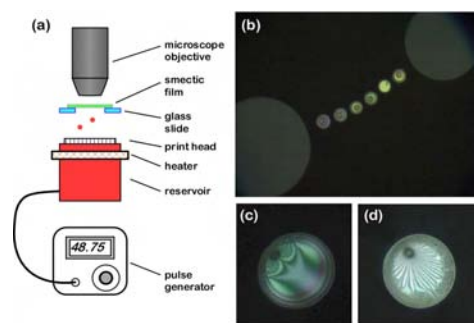


**Figure 2.10:** Inkjet printing of smectic islands. Small water drops printed by a piezoelectric inkjet print head onto a smectic film (**a**) transform after about 30 minutes into monodisperse smectic islands. These interact, forming chains (**b**), and exhibit complex textures, such as multiple  $\pi$ -walls (**c,d**).

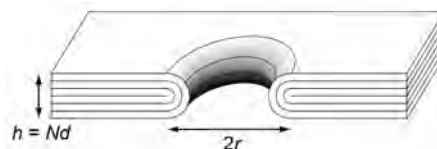


**Figure 2.11:** Schematic depiction of the formation of a pore of radius  $r$  in an  $N$ -layer freely suspended smectic film, where  $h = Nd$  is the film thickness and  $d$  is the smectic layer spacing.



## 2.4 – THEORETICAL BACKGROUND AND MOTIVATION

### 2.4.1 – STABILITY OF SMECTIC FILMS

FSLC films are long-lived, metastable fluid structures that are stabilized against thinning by smectic layering. In thermal equilibrium, rupture of a FSLC film involves nucleation and growth of a pore that penetrates the film, as indicated schematically in **Figure 2.11**. Removal of material from the film to the meniscus at the film boundary leads to a reduction in surface area and in the associated interfacial free energy. Unlike isotropic fluid films, however, FSLC films cannot thin continuously, but only in discrete multiples of the smectic layer spacing. Thus, pore nucleation requires formation of a pore boundary of finite thickness (equal to the film thickness), and the interfacial free energy cost of creating the pore boundary produces an activation barrier to pore nucleation.

The typical lifetime of a FSLC film can be deduced from the pore nucleation rate [47]. A rough estimate of this rate can be obtained by considering the Gibbs free energy change associated with formation of a pore in an  $N$ -layer film,  $\Delta G = 2\pi r h \gamma - 2\pi r^2 \gamma$ , where  $r$  is the pore radius,  $h = Nd$  is the film thickness,  $d$  is the smectic layer spacing, and  $\gamma$  is the surface tension. The first term in  $\Delta G$  represents the interfacial free energy cost of creating the pore boundary (assumed to be cylindrical), and the second term represents the interfacial free energy gain due to reduction in the area of the two free surfaces of the film (hence the factor of 2). This estimate of the free energy change is admittedly crude, and neglects other contributions to the free energy, including the pressure difference between the film and the meniscus and the disjoining free energy of the film (discussed below), but it is sufficient for a qualitative understanding of film stability.

The critical pore radius is the position of the maximum in  $\Delta G$ ,  $r_c = h/2$ , and the activation barrier is  $\Delta G_{\max} = 2\pi\gamma r_c^2 = \pi\gamma h^2/2$ . For thin films,  $r_c$  is microscopic, ranging from  $r_c \approx 15$  Å for a 1-layer film to  $r_c \approx 300$  Å for a 20-layer film (assuming  $d \approx 30$  Å). The pore nucleation rate per unit area is  $f = f_0 \exp[-\Delta G_{\max}/(k_B T)]$ , where  $f_0$ , the attempt frequency per unit area, is of the order of the speed of sound divided by the cube of the molecular diameter ( $f_0 \approx 10^{27} \text{ s}^{-1} \text{ cm}^{-2}$ ). With typical numbers ( $\gamma \approx 30 \text{ dyne/cm}$ ,  $d \approx 3 \times 10^{-7} \text{ cm}$ ), we have  $f = f_0 \exp[-\pi\gamma N^2 d^2/(2k_B T)] \approx 10^{27} \exp[-100 N^2] \text{ s}^{-1} \text{ cm}^{-2}$  at  $T = 300 \text{ K}$ . This is an exceedingly small number, even for a one-layer film ( $f \approx 4 \times 10^{-17} \text{ s}^{-1} \text{ cm}^{-2}$  for  $N = 1$ ), and the  $N^2$ -dependence of the exponent implies that two-layer or thicker films are almost indefinitely stable (lasting for months under suitable conditions). Empirically, it is found that one-layer films are rather unstable (although one-layer films of certain materials may be stable for an hour or more), suggesting that the pre-factor in the exponent should be somewhat smaller than 100 [47].

### 2.4.2 – FSLC FILM STRUCTURE AND THERMODYNAMICS

Freely suspended smectic films are in chemical and mechanical equilibrium with the meniscus that forms at the boundary of the film holder (**Figure 2.12**). Thus, any discussion of the thermodynamic and mechanical properties of FSLC films must

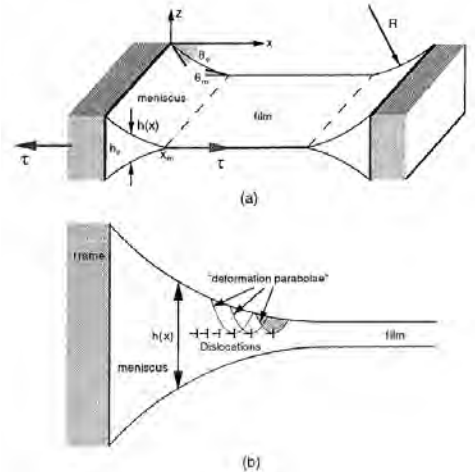


**Figure 2.12:** Schematic representation of a smectic film in contact with a meniscus (from [52]).  $h(x)$  defines the shape of the meniscus, which is circular, with radius  $R$ , close to the film.  $\theta_m$  and  $\pi/2 - \theta_0$  are the contact angles at the film and at the frame, respectively, and  $\tau$  is the film tension. The distribution of dislocations in the meniscus is shown in (b).

necessarily take the meniscus into account.

The formation and structure of the smectic meniscus has been discussed in detail by Picano et al. [48]. These authors show that the smectic meniscus has a circular profile, in contrast with ordinary liquids, for which the meniscus has an exponential shape, with the size of the meniscus set by the capillary length  $l_c = \sqrt{\gamma/\rho g}$  (determined by the competition between gravity and surface tension). Moreover, the smectic meniscus is about two orders of magnitude smaller than that of an isotropic liquid, with a structure that depends on the complex, irreversible process by which the smectic film is created (involving dislocation nucleation at the boundary of the film). The circular profile of the meniscus results from functional minimization

of its free energy, including contributions from surface tension, the Laplace pressure difference between the interior and exterior of the meniscus (due to curvature of the surface), and the core energy of the dislocations [48]. This calculation assumes that the meniscus consists of non-interacting elementary dislocations confined to its mid-plane (Figure 2.12). It is reasonable to neglect dislocation interactions in this case because the linear elastic theory of bulk smectics predicts that the pair interaction (Peach-Kohler interaction) between elementary dislocations vanishes if their separation vector is parallel to the smectic layers (along the climb direction) [49]. Giant dislocations (with Burgers vector greater than 20) and focal conic defects are observed in the thickest part of the film, near the film holder (Figure 2.13).

FSLC films owe their stability to the fact that smectics can support a stress in the layer normal direction, and are generally in a state of uniaxial stress, due to the pressure difference between the interior of the meniscus and the surrounding atmosphere. According to the Young-Laplace equation, the pressure within the meniscus is  $P_M = P_A - \gamma / R$ , where  $P_A$  is atmospheric pressure,  $R$  is the curvature of the meniscus in the radial direction, and  $\gamma$  is the (bulk) surface tension. Because the smectic film is in mechanical equilibrium with its meniscus and with the surrounding atmosphere, it is subject to a uniaxial stress; the lateral pressure (perpendicular to the layer normal) within the film is  $P_M$ , while the longitudinal pressure (in the layer normal direction) is  $P_A$ . This produces a thickness-dependent effective tension,  $\tau = dG/dA = 2\gamma + \Delta P h$ , where  $G$  is the Gibbs free energy of the film,  $A$  is the film area,  $\Delta P = P_A - P_M$  is the pressure difference between the atmosphere and the meniscus, and  $h = Nd$  is the film thickness. The predicted linear dependence of film tension on thickness has been experimentally verified for thick smectic films [50].

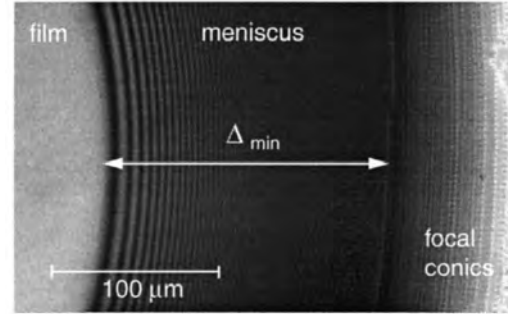


**Figure 2.13:** Microscopic observation of a film and its meniscus, using both transmitted and reflected monochromatic light (from [48]). The interference fringes observed in the thinnest part of the meniscus give the radius of curvature of the meniscus ( $R = 2.8$  mm). Giant dislocations and chains of focal conics are visible in the thickest part of the meniscus.

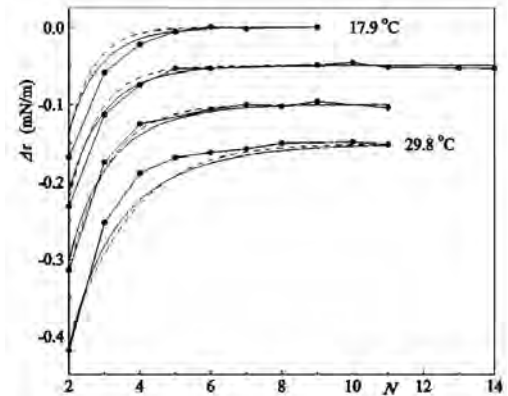


**Figure 2.14:** Film tension decrease ( $\Delta\tau = G_d$ ) versus layer number  $N$  for thin films of 8CB at several temperatures (from [51]). The lines represent fits to Landau-de Gennes theory both with (solid lines) and without (dashed lines) quartic terms in the free energy. The curves have been shifted vertically for clarity.

In thin smectic films, there is an additional (disjoining free energy) contribution to the film tension, arising from effective interactions between the two free surfaces of the film. The structural organization of a smectic film differs from that of the bulk within a boundary region of thickness  $\xi$ , giving rise to structural forces between the two surfaces of the film in thin films ( $h < 2\xi$ ). This structural contribution to the disjoining free energy is expected to dominate in smectic films, although contributions from long-range (electrostatic and dispersion) interactions may also be present. In general, we can write  $\tau = 2\gamma + \Delta Ph + G_d$ , where  $G_d$  is the disjoining free energy per unit area (this is essentially the definition of  $G_d$ ; i.e.,  $G_d \equiv dG/dA - 2\gamma - \Delta Ph$ ). The disjoining free energy usually reduces the tension of a thin smectic film (Figure 2.11) [51], because the two surfaces share the free energy cost of creating two free surfaces once their boundary layers begin to overlap. This behavior is reasonably well captured by a Landau-de Gennes free energy functional that accounts for the variation in smectic order parameter near the free surfaces [51]. Note, however, that the disjoining free energy can have either sign, and its variation with layer number  $N$  need not be smooth and monotonic. For example, we have observed positive disjoining free energy in one-layer films of a partially fluorinated material (Figure 2.2), which tend to spontaneously thicken to form two-layer films (suggestive of an odd/even variation in the sign of  $G_d$ ).

Note that disjoining free energy effects can alternatively be attributed to a thickness-dependent surface tension, i.e.,  $\gamma(N) = \gamma(\infty) + G_d(N)/2$ , where  $\gamma(N)$  is the apparent surface tension of an  $N$ -layer film,  $\gamma(\infty)$  is the bulk surface tension, and the factor of 2 accounts for the fact that the film has two free surfaces. We will use both viewpoints (disjoining free energy and thickness-dependent surface tension) interchangeably, but it should be kept in mind that the two alternative descriptions are equivalent.

The disjoining free energy also determines the apparent contact angle between a smectic film and its meniscus (Figure 2.12) [52]. Considering the balance of forces on the contact line between an  $N$ -layer film and its meniscus leads to the relation  $2\gamma \cos \theta_m = 2\gamma + G_d(N)$  (analogous to the Young equation), which is consistent with our interpretation of  $\gamma + G_d(N)/2$  as the effective surface tension of an  $N$ -layer film (here  $\gamma = \gamma(\infty)$  is the bulk surface tension). Disjoining free energies deduced from measurements of the contact angle are consistent with those obtained from film tension measurements [63].

The stability of smectic films against nucleation and growth of a pore that penetrates the film was considered above. However, smectic films can also undergo layer-by-layer thinning (i.e., dislocation loop or pore nucleation and growth), at a rate governed by the line tension (free energy per unit length) of the dislocation loop.

We can estimate the nucleation rate of a circular pore (( $N-n$ )-layer region) in an  $N$ -layer smectic film from classical nucleation theory. The free energy of an ( $N-n$ )-layer pore in an  $N$ -layer film is  $\Delta G = 2\pi r E - \pi r^2 \Delta P b + \pi r^2 \Delta G_d$ , where  $r$  is the pore radius,  $E$  is the line tension of the dislocation loop (pore boundary),  $b = nd$  is the Burgers vector of the dislocation, and  $\Delta G_d = G_d(N-n) - G_d(N)$  is the change in disjoining free energy per unit area due to film thinning. The critical pore radius is the position of the maximum in  $\Delta G$ ,  $r_c = E / (\Delta P b - \Delta G_d)$ , and the nucleation barrier is  $\Delta G_{\max} = \pi E^2 / (\Delta P b - \Delta G_d) = \pi E r_c$ . For thick films, the disjoining free energy contribution is negligible, and these expressions reduce to  $r_c = E / (\Delta P b) = ER / (\gamma b)$  and

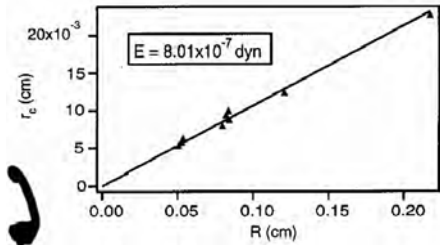


**Figure 2.15:** Critical radius of nucleation  $r_c$  as a function of the radius of curvature of the meniscus  $R$  (from [48]).

$\Delta G_{\max} = \pi E^2 / (\Delta P b) = \pi E^2 R / (\gamma b)$ . In this limit, the critical radius and activation barrier are independent of film thickness, and depend linearly on the radius of curvature of the meniscus. This provides a means of measuring the dislocation line tension  $E$  in thick films, if the surface tension  $\gamma$  and Burgers vector  $b$  are known. For example, the line tension of an elementary ( $n = 1$ ) dislocation loop in a thick 8CB film is  $E = 8 \times 10^{-7}$  dyne (Figure 2.14) [48]. In these experiments,  $r_c$  was measured directly, by locally heating a film to nucleate dislocation loops and observing whether the nucleated dislocation loop grows or shrinks after the heating element is removed (Figure 2.15). An alternative approach involves inserting a needle through the film and measuring the radius of curvature of a layer step ('isthmus') that forms between the needle meniscus and the film meniscus when the needle is brought close to the boundary of the film (the 'Mont Saint-Michel method') [50]. A more accurate method for obtaining  $E$  by measuring the deformation of a dislocation loop in a vertical film under the action of gravity is described below.

The critical nucleation radius typically decreases strongly with decreasing film thickness in thin films (less than  $\sim 30$  layers), due to a decrease in disjoining free energy with thickness ( $\Delta G_d < 0$ , as in Figure 2.14). As discussed above, however,  $G_d$  increases with decreasing thickness in some smectic materials, and nucleation and growth of islands rather than pores can occur if  $\Delta P n d + G_d(N + n) - G_d(N) < 0$ . This is evidently the case in partially fluorinated materials, where we have observed nucleation of two-layer islands in one-layer films (Figure 2.4).

With typical numbers for thick films of 8CB ( $\lambda = 8 \times 10^{-7}$  dyne,  $\Delta P = 250$  dyne/cm<sup>2</sup>), the activation barrier for nucleation of an elementary dislocation loop is found to be quite large,  $\Delta G_{\max} = 2.6 \times 10^{-8}$  erg  $\approx 6 \times 10^5 k_B T$ , which implies a vanishingly small nucleation rate per unit area  $f = f_0 \exp[-\Delta G_{\max} / (k_B T)]$  (recall that  $f_0 \approx 10^{27}$  s<sup>-1</sup>cm<sup>-2</sup>). The activation barrier for thin films of 8CB is considerably smaller, due to the disjoining free energy contribution, but the nucleation rate is still negligible. For a 3-layer film of 8CB, for example,  $\Delta G_{\max} = 300 k_B T$  and  $f < 10^{-100}$  s<sup>-1</sup>cm<sup>-2</sup>!

Although the rate of spontaneous nucleation of dislocation loops is effectively zero, dislocation loops can be artificially nucleated by local heating of a film, by rapid changes in the area supported by the film holder, or by blowing air across a film to induce extensional flow [63,72]. Pores or islands can also be nucleated by uniformly heating the smectic film above the bulk smectic–nematic or smectic–isotropic transition temperature. For moderate superheating, the enthalpy of transition reduces the activation barrier, and a sequence of layer-by-layer thinning transitions is observed as the temperature is increased above the bulk transition temperature [53,54,55,56,57]. Superheating can also lead to the nucleation of isotropic or nematic droplets in the film, which become islands upon subsequent cooling [58,59,60].

As mentioned above, the line tension of dislocation loops can be measured by nucleating a dislocation loop in a vertical film and measuring its deformation when it is in con-

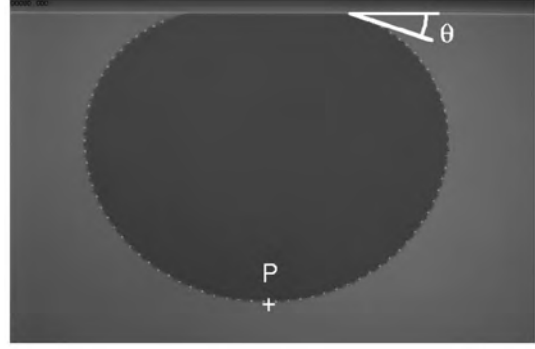


**Figure 2.16:** Dislocation loop in a 12-layer vertical film of 8CB at  $T = 33$  °C (from [62]). The Burgers vector is  $b = 60$  Å (two layers). The dotted line is the best fit to the equilibrium shape calculated from theory, with  $E/b = 1.43$  dyne/cm. The meniscus is visible at the top edge of the photograph, and the horizontal loop diameter is  $466$   $\mu$ m.

tact with the top edge of the film holder (Figure 2.16) [61,62]. This method is a 2D analog of the sessile drop method that is commonly used to measure the surface tension of isotropic fluids. Assuming that the dislocation loop is static (neither growing nor shrinking), the shape of the loop is determined by the differential equation  $\lambda\kappa = b(\Delta P_0 + \rho g z)$ , where  $\kappa$  is the local curvature of the dislocation,  $\rho$  is the mass density of the liquid crystal, and  $z$  is the vertical position within the film (measured from the bottom of the film holder). The line tension  $E$  is obtained by fitting the measured shape to a numerical solution of this equation.

The line tension measured for elementary dislocations (and one two-layer dislocation) using this method is shown in Figure 2.17. The measured line tension decreases with increasing film thickness, in reasonable agreement with a theoretical expression including bulk and surface contributions to  $E$  [62], described below.

Thickness variations in smectic films also lead to variations in the lateral (in-plane) pressure across curved 1D interfaces between 2D regions of differing thickness, due to the finite interfacial tension (analogous to the Laplace pressure drop across a curved 2D interface). We can derive an expression for the pressure difference across the boundary of a circular island or pore by considering the condition for mechanical equilibrium in the limit that the island/pore is chemically isolated from the surrounding film (i.e., neglecting transport of material across the interface). We will, in general, assume that the rate of mass transport across layer interfaces is slow compared with relaxation of the film to mechanical equilibrium (i.e., the velocity of dislocation motion is small compared with the sound velocity), so that the film can be assumed to be in a state of mechanical equilibrium.

The radial force per unit length acting on the interface between an  $N_1$ -layer circular island or pore of radius  $r$  and the surrounding  $N_2$ -layer film is:

$$P_1 N_1 d - P_2 N_2 d + P_A (N_2 - N_1) d + 2(\gamma_2 - \gamma_1) - E/r.$$

Here,  $P_1$  and  $\gamma_1$  are the in-plane pressure and surface tension inside the island/pore,  $P_2$  and  $\gamma_2$  are the corresponding quantities in the surrounding film, and  $E$  is the line tension of the dislocation loop (note that we have incorporated disjoining free energy contributions into a thickness-dependent surface tension). Setting this force to zero (the condition for mechanical equilibrium) leads to the following equation for the in-plane pressure difference between the interior and exterior of the island/pore:

$$\Delta P = \frac{E}{h_1 r} + \frac{2\Delta\gamma}{h_1} + \frac{h_1 - h_2}{h_1} \Delta P_0.$$

Here  $h_1 = N_1 d$ ,  $h_2 = N_2 d$ ,  $\Delta P = P_1 - P_2$ ,  $\Delta P_0 = P_A - P_2$ , and  $\Delta\gamma = \gamma_1 - \gamma_2$ . The first term on the right-hand side of this equation is the 2D analog of the familiar (3D) Laplace pressure, the second term includes the effect of a thickness-dependent surface tension, and the

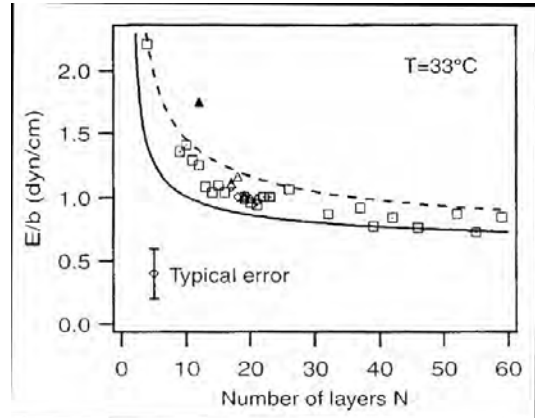


**Figure 2.17:** Line tension  $E/b$  of 8CB as a function of film thickness  $N$  at  $T = 33^\circ\text{C}$  [62]. Empty squares, triangles, and diamonds correspond to elementary dislocations in three different films. The full triangle corresponds to the dislocation of Burgers vector  $60\text{ \AA}$  (two layers) shown in Figure 2.16. The solid and dashed curves are theoretical predictions for dislocations of Burgers vector  $30\text{ \AA}$  and  $60\text{ \AA}$ , respectively.

third term accounts for the pressure exerted by the surrounding atmosphere on a film of non-uniform thickness.

As described in the following **Section**, in-plane pressure differences drive mass transport across dislocation loop boundaries. The balance between this driving force and dissipation associated with mass transport governs the dynamics of edge dislocation loops.

### 2.4.3 – DISLOCATION DYNAMICS

The dynamics of edge dislocation loops in freely suspended smectic films has been studied extensively by Oswald and co-workers [36,63], who have developed a theoretical model for dislocation loop dynamics, based on the dissipation theorem. The relevant theory and proposed extensions are summarized below.

As noted in [63], there are two distinct approaches to the dynamics of edge dislocation loops: a *local* approach, in which the forces acting on dislocation lines are considered explicitly, and a *global* approach, based on application of the dissipation theorem to the system as a whole. The global approach has been successfully applied to the dynamics of isolated dislocation loops in freely suspended films [36,63], and should be applicable to the collective dynamics of assemblies of well-separated dislocation loops, although this hasn't yet been investigated. The equivalence of local and global approaches in specific cases has been established in [49]. The theoretical description of dislocation loop coalescence requires a microscopic treatment of dislocation structure and dynamics. For example, a Landau-de Gennes approach has recently been applied to the annihilation of infinitely long, straight edge dislocations in the bulk SmA phase [64]. In the following, we consider only the global approach to dislocation dynamics.

The dissipation theorem assumes that any free energy gain by the system (consisting of a smectic film and its meniscus) is completely dissipated during dislocation loop growth or shrinkage,  $d\Delta G/dt = \Phi$  (i.e., inertial effects are neglected). Here,  $\Delta G$  is the free energy increase associated with dislocation motion, and  $\Phi$  is the dissipation function.

As discussed above, the free energy of an  $N_1$ -layer circular island or pore (dislocation loop) of radius  $r$  in an  $N$ -layer film is  $\Delta G = 2\pi r\lambda - \pi r^2 \Delta P b + \pi r^2 \Delta G_d$ . Here,  $E$  is the line tension of the dislocation,  $\Delta P = \gamma/R$  is the in-plane pressure difference between the film and the meniscus, where  $R$  is the radius of curvature of the meniscus and  $\gamma$  is the bulk surface tension,  $b = nd$  is the Burgers vector of the dislocation loop, where  $n \equiv N - N_1$  and  $d$  is the smectic layer spacing, and  $\Delta G_d = G_d(N_1) - G_d(N)$  is the disjoining free energy difference per unit area between the  $N_1$ -layer island/pore and the  $N$ -layer 'background' film. Thus,  $d\Delta G/dt = 2\pi v(\lambda - r\Delta P b + r\Delta G_d)$ , where  $v = dr/dt$  is the radial velocity of the dislocation loop. The dissipation function contains three terms,  $\Phi = \Phi_d + \Phi_m + \Phi_f$ , describing, respectively, dissipation due to flow around the core of the dislocation, dissipation due to flow in the meniscus, and dissipation due to two-dimensional flow within the smectic film.

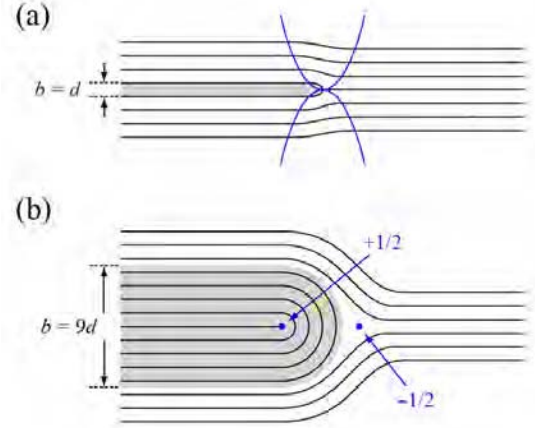


**Figure 2.18:** Edge dislocations in a smectic A. (a) Elementary edge dislocation. The stress is significant within the two parabola drawn in blue. (b) Core of a giant dislocation split into two disclination lines of topological charge  $+1/2$  (left) and  $-1/2$  (right).

The energy dissipated by flow around the dislocation core is  $\Phi_d = 2\pi r(d/\mu)v^2$ , where  $m$  is the mobility of the dislocation (usually assumed to be independent of Burgers vector) [63]. The mobility is independent of  $N$  in thick films but is predicted to decrease as  $\mu_\infty(N-1)/N$  in thin films, where  $\mu_\infty$  is the bulk dislocation mobility. The mobility  $\mu_\infty$  has been measured directly in creep experiments on smectics confined between glass plates [48,49].

The dissipation due to flow in the meniscus is  $\Phi_m = 2\pi r_m CN(d/\mu)v_m^2$ , where  $r_m$  is the radius of the film (assumed to be circular),  $C$  is a function of  $N$  that has been estimated in [36] (see **Figure 2.20**), and  $v_m = (1/N)(r/r_m)v$  is the average hydrodynamic velocity at the entrance to the meniscus (assuming a single circular island or pore is present in the film).

The energy dissipated by 2D flow within the film is  $\Phi_f = 4\pi\eta d(1/N)(1-r^2/r_m^2)v^2$ , where  $h$  is the viscosity corresponding to shear in the plane of the layers ( $h_2$  in the Martin-Parodi-Pershan notation [36]). This term is much smaller than  $F_d$  (by a factor of at least 500), and will be neglected in the following discussion.

With these contributions, the dissipation equation becomes:

$$\frac{1}{\mu} \frac{dr}{dt} \left( 1 + \frac{Cr}{r_m N} \right) = \Delta P - \frac{\Delta G_d}{d} - \frac{E}{rd}.$$

Setting  $dr/dt = 0$ , we recover the expression for the critical pore radius derived above,  $r_c = E/(\Delta P d - \Delta G_d)$ . Defining a characteristic time  $\tau$ , given by

$$\tau = \frac{dr_c}{\mu(\Delta P d - \Delta G_d)},$$

the solution of the dissipation equation can be written

$$\frac{t}{\tau} = \left( 1 + \frac{Cr_c}{Nr_m} \right) \left[ \frac{r(t) - r_0}{r_c} + \ln \left( \frac{r(t) - r_c}{r_0 - r_c} \right) \right] + \frac{C(r^2(t) - r_0^2)}{Nr_m r_c},$$

where  $r_0$  is the pore radius at the initial time  $t_0$  ( $r_0 = r(t_0)$ ). The physical quantities that appear in this expression (e.g.,  $r_m$ ,  $R$ ,  $N$ ,  $r_0$ , and  $C$ ) can be measured experimentally, enabling prediction of the growth dynamics of a single dislocation loop in a smectic film. Fits of experimental measurements of  $r(t)$  to this expression for pores in 8CB films are shown in **Figure 2.19**, with  $C$  treated as a fitting parameter.  $C(N)$  can also be measured by equilibrating two menisci of different radii [65], and the two methods of measuring  $C(N)$  are in reasonable agreement with each other and with a theoretical estimate that explicitly considers the dissipation due to flow around the dislocations located at the mid-plane of the meniscus (**Figure 2.20**) [36,63].

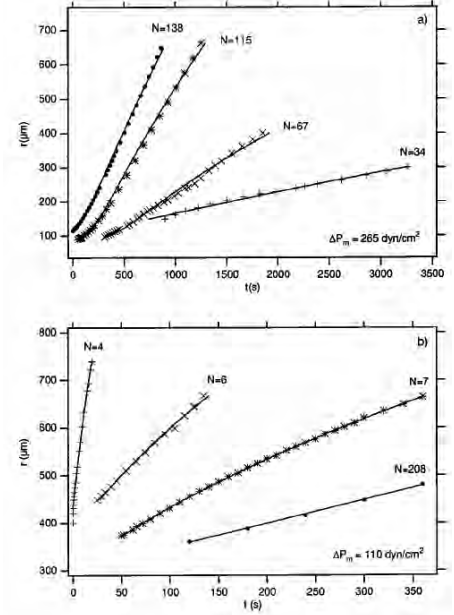


**Figure 2.19:** Pore radius  $r(t)$  measured in two different 8CB films (from [63]). (a) Curves obtained for large and intermediate values of  $N$  ( $\Delta P \approx 260$  dyne/cm<sup>2</sup>,  $N > 20$ ); (b) curves obtained for small  $N$  ( $\Delta P \approx 110$  dyne/cm<sup>2</sup>,  $N < 10$ ), with the first part of the  $N = 208$  curve shown for comparison. In both graphs the curves have been shifted in time for clarity. The solid lines are best fits to the theoretical prediction, taking the values of  $C$  shown in **Figure 2.20**.



In thick films ( $N > 100$ ),  $r(t)$  increases linearly with time for  $r \gg r_c$ , with a velocity  $v_\infty \approx \mu \Delta P$ . In this limit, the growth velocity is limited by dissipation due to flow around the core of the dislocation, and dissipation in the meniscus is negligible. The mobility deduced from these results ( $\mu \approx 4 \times 10^{-7} \text{ cm}^2/\text{s/g}$ ) is in reasonable agreement with previous measurements [48]. In films of intermediate thickness (between 10 and 100 layers), dissipation in the meniscus becomes important, and the growth velocity is systematically smaller than  $v_\infty$ . Finally, for very thin films (less than 10 layers), the disjoining free energy leads to an effective attraction between the free surfaces of the film, providing an additional driving force for dislocation motion that causes a strong increase in growth velocity with decreasing  $N$  ( $v > v_\infty$ , as shown in **Figure 2.19b**).

This formalism can be applied to films containing two or more dislocation loops, in which case the dynamics of a given dislocation loop depends strongly on the other dislocation loops that are present. For example, the critical radius of one dislocation loop depends on the radii of all of the other loops [36]. In general, however, the coupled equations of motion of multiple dislocation loops don't admit closed-form solutions and must be solved numerically.

The previous theoretical work [36,63] neglects in-plane variations in pressure due to dislocation loop curvature and variations in film thickness (e.g., in arrays of thick islands). These contributions may have a significant effect on dislocation loop dynamics, particularly in the bubble geometry, where the influence of the meniscus is minimized. An appropriately generalized theoretical framework will be pursued in our future work.

#### 2.4.4 – DISLOCATION STRUCTURE AND ENERGETICS

The structure of edge dislocations in smectic films determines their line tension, interactions, and dynamics. Here we briefly review the theory of edge dislocations in the bulk and in thin films. Theoretical treatments of defect structure and energetics in smectics [49,36,66] usually start with the linear elastic free energy density

$$f_{el} = \frac{1}{2} [B(\nabla_\parallel u)^2 + K_1(\nabla_\perp^2 u)^2] = \frac{1}{2} [B(\partial u / \partial z)^2 + K_1(\partial^2 u / \partial x^2 + \partial^2 u / \partial y^2)^2]$$

valid for small displacements  $u(\mathbf{r})$  of the smectic layers. Here  $z$  is the layer normal direction,  $B$  is the layer compressional modulus, and  $K_1$  is the director splay (layer bend) elastic constant. Director bend and twist distortions, which involve large deviations of the layer spacing from its equilibrium value, are strongly suppressed in smectics, and are usually not considered in treatments of smectic elasticity.

Now consider an edge dislocation in a bulk smectic oriented along the  $y$ -axis, with Burgers vector  $b$ . In this case, the displacement field depends only on  $x$  and  $z$ , i.e.,  $u(x,z)$ . Minimization of the elastic free energy functional leads to an Euler-Lagrange equation for the strain field around the dislocation,

$$\frac{\partial^2 u}{\partial z^2} - \lambda^2 \frac{\partial^4 u}{\partial x^4} = 0,$$

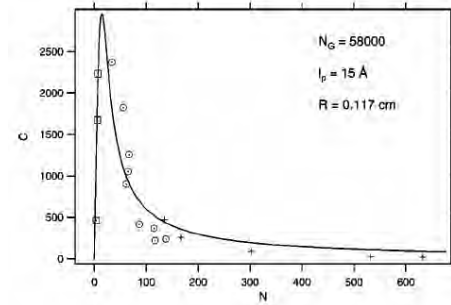


**Figure 2.20:** Values of  $C$  obtained as a function of  $N$  by fitting the experimental  $r(t)$  to the theoretical expression in the text (squares and dots) (from [63]). Values for large  $N$  (crosses) have been obtained by another method, involving equilibration of two menisci of different radii. The solid line is the best fit to a theoretical expression for  $C$ .



where  $\lambda = \sqrt{K_1/B}$ . The solution to this equation in the  $z > 0$  half-space with the  $z = 0$  boundary condition

$$u(x,0) = \begin{cases} 0, & x < 0 \\ b/2, & x > 0 \end{cases}$$

is

$$u(x,z) = \frac{b}{4} \left[ 1 + \operatorname{erf} \left( \frac{x}{2\sqrt{\lambda z}} \right) \right],$$

where erf is the error function. Thus, the tilt angle of the layer normal relative to the  $z$ -axis is

$$\theta(x,z) = \frac{\partial u}{\partial x} = \frac{b}{4\sqrt{\pi\lambda z}} \exp \left( -\frac{x^2}{4\lambda z} \right)$$

and the layer dilation is

$$\frac{\partial u}{\partial z} = \frac{bx}{8\sqrt{\pi\lambda z^3}} \exp \left( -\frac{x^2}{4\lambda z} \right).$$

The strain (and hence the stress) propagates far from the dislocation in the glide ( $x = 0$ ) plane, but falls off exponentially in the plane of the layers, and most of the deformation falls within the two parabolae defined by  $x^2 = \pm 4\lambda z$  (**Figure 2.18a**). This is in sharp contrast to a dislocation in a solid, which gives rise to a stress field that falls off isotropically (as  $1/r$ ) [66].

Given this solution, the elastic free energy per unit length of the dislocation is

$$E = \frac{K_1 b^2}{2\lambda \xi} + E_c = \frac{B\lambda b^2}{2\xi} + E_c,$$

where  $\xi$  is the width of the dislocation core (short-wavelength cutoff) in the  $x$ -direction and  $E_c$  is the core energy. The quadratic dependence of  $E$  on  $b$  would appear to strongly disfavor large Burgers vector dislocations. However, minimizing  $E$  with respect to  $x$  under the assumption that the core energy is proportional to the core width [49],  $E_c \approx \varepsilon \xi$ , yields an optimal core width proportional to  $b$ ,

$$\xi = \left( \frac{B\lambda}{2\varepsilon} \right)^{1/2} b,$$

and a linear dependence of  $E$  on  $b$ ,

$$E = \left( \frac{K_1 B \varepsilon^2}{4} \right)^{1/4} b.$$

This result depends on the *ad hoc* assumption that the core energy is proportional to  $x$ , but is consistent with the experimental observation that non-elementary ( $b > d$ ) edge dislocations are stable against dissociation into elementary dislocations [49], and helps to explain why large Burgers vector dislocations are common in smectics (in contrast to crystalline solids).

The force exerted by a stress field on a dislocation is given by the Peach-Koehler formula,  $\mathbf{F} = (\boldsymbol{\sigma}^t \mathbf{b}) \times \mathbf{t}$  [67], where  $\mathbf{s}^t$  is the transpose of the stress tensor (due to other dislocations or an applied stress),  $\mathbf{b}$  is the Burgers vector, and  $\mathbf{t}$  is a unit vector tangent to the dislocation line. For two parallel dislocations oriented along the  $y$ -axis, with the first dislocation at the origin (0,0) and the second at  $(x,z)$ , the components of force per unit length exerted by the first dislocation on the second are [49]

$$F_x = \frac{Bb_1b_2x}{8\sqrt{\pi\lambda|z|^3}} \exp\left(-\frac{x^2}{4\lambda|z|}\right),$$

$$F_z = \frac{\text{sgn}(z)K_1b_1b_2}{16\sqrt{\pi\lambda^3|z|^3}} \left(2 - \frac{x^2}{\lambda|z|}\right) \exp\left(-\frac{x^2}{4\lambda|z|}\right).$$

If the two dislocations have Burgers vectors of opposite sign, then the climb force  $F_x$  is attractive everywhere, whereas the glide force  $F_z$  is repulsive outside the parabolae defined by  $x^2 = \pm 2\lambda z$  and attractive inside. Due to the exponential decay in the climb direction, the force between dislocations is significant only when the two dislocations are more or less in the same glide plane (same  $x$ ), and vanishes for dislocations in the same climb plane (same  $z$ ).

Large Burgers vector dislocations are predicted to have a different core structure, in which the dislocation is split into a pair of  $+1/2$  and  $-1/2$  disclination lines separated by a distance  $b/2$  (Figure 2.18b) [49,66]. This situation is expected for Burgers vectors greater than about five smectic layer spacings, typically. In this case, the core width  $\xi \approx b/2$ , so the elastic contribution to the dislocation energy scales linearly with  $b$ ,  $E = B\lambda b + E_c$ , and the core energy can be written

$$E_c = \frac{\pi K_1}{2} \ln \frac{b}{2d} + E_d,$$

where  $E_d$  is the core energy of the two disclinations (of order  $K_1$  and independent of  $b$ ). Thus, the energy change resulting from coalescence of two dislocations of Burgers vector  $b$  into a single dislocation of Burgers vector  $2b$  is

$$E(2b) - 2E(b) = \frac{\pi K_1}{2} \ln \frac{4d}{b},$$

which is negative for  $b > 4d$ , implying that large Burgers vector dislocations are favored for sufficiently large  $b$ .

The structure and energy of edge dislocations are modified by the inclusion of nonlinear terms in the elastic free energy, which arise due to rotational invariance of the free energy [68,66,69], but such modifications do not lead to significant qualitative changes in their behavior, and will not be considered further here.

Of more importance in the context of freely suspended smectic films are the effects of interactions of dislocations with free surfaces. As shown by Lejcek and Oswald [70], the elastic interaction energy of a dislocation with a free surface can be taken into account by including a surface free energy contribution

$$F_s = \frac{\gamma}{2} \int_s (\partial u / \partial x)^2 dx$$

in addition to the usual smectic elastic free energy functional, where the integral is over the free surface(s) of the film. This additional term imposes a boundary condition on the usual Euler-Lagrange equation,

$$B \frac{\partial u}{\partial z} = \gamma \frac{\partial^2 u}{\partial x^2},$$

where the right-hand side of this equation is the Laplace pressure difference due to curvature of the free surface, and the left-hand side the local compression or dilation of the smectic layers. A solution to the bulk elastic equation consistent with this boundary condition can be obtained by introducing an image dislocation outside the free surface [49,70]. The free surface exerts a glide force  $F_z$  on the dislocation given by

$$F_z = -\frac{K_1 b^2}{16\sqrt{2\pi\lambda^3 z_0^3}} \frac{\gamma - \sqrt{K_1 B}}{\gamma + \sqrt{K_1 B}},$$

where  $z_0$  is the depth of the dislocation below the free surface. This expression shows that the interaction between the dislocation and the surface is repulsive for  $\gamma > \sqrt{K_1 B}$  and attractive for  $\gamma < \sqrt{K_1 B}$ . For typical smectic elastic constants,  $K_1 \approx 10^{-6}$  dyne and  $B \approx 10^8$  erg/cm<sup>3</sup>, we have  $\sqrt{K_1 B} \approx 10$  erg/cm<sup>2</sup>, which is much smaller than the typical surface tension of a smectic,  $\gamma \approx 25$  erg/cm<sup>2</sup>, and so dislocations are typically repelled from the LC-air interface and will thus tend to reside near the mid-plane of a freely suspended smectic film. This force will compete with the force derived from the lattice potential (Peirls-Nabarro force), which can pin the dislocation at a metastable position (not in the center of the film), so dislocation loops can be at different  $z$ -positions in the film.

Interactions with the free surfaces also contribute to the free energy per unit length (line tension) of a dislocation in a freely suspended smectic film. The line tension of an edge dislocation at the center of an  $N$ -layer freely suspended film can be written

$$E = E_\infty + E_s,$$

where  $E_\infty$  is the line tension of the dislocation in an infinite medium (no free surfaces), and  $E_s$  is the surface correction, given by [70]

$$E_s = \frac{B\lambda b^2}{4\sqrt{\pi\lambda d(N+1/2)}} \text{Li}_{1/2}\left(\frac{\gamma - \sqrt{K_1 B}}{\gamma + \sqrt{K_1 B}}\right),$$

where  $\text{Li}_{1/2}(x)$  is a polylogarithm function,

$$\text{Li}_{1/2}(x) = \sum_{n=1}^{\infty} \frac{x^n}{n^{1/2}}.$$

The surface contribution  $E_s$  falls off slowly with  $N$ , roughly as  $1/\sqrt{N}$ . The theoretical predictions are in reasonable agreement with experimental measurements of the dependence of line tension on film thickness (Figure 2.17) [62].

Finally, as discussed by Holyst [71], surface tension can dramatically modify the surface profile of a thin smectic film in the vicinity of an edge dislocation, increasing the width of the region over which the layers are deformed by as much as an order of magnitude. Holyst also demonstrated that including a surface layer bend elastic term in the free energy can lead to a new minimum free energy solution in which the dislocation is stabi-

lized at a finite non-zero distance from the free surface [71]. Both effects may influence the structure and interactions of edge dislocations in freely suspended smectic films.

#### 2.4.5 – TEXTURE-MEDIATED INTERACTIONS IN SMECTIC C FILMS

The presence of in-plane order (e.g., smectic C tilt) produces strong, directional, long-range effective interactions between islands in smectic films, originating in the generalized elasticity of the ordering field. In smectic C films, in-plane ordering can be characterized by the  $\mathbf{c}$ -director  $\mathbf{c}$ , a unit vector parallel to the projection of the local long molecular axis into the layer plane. Given a specific preferred orientation of  $\mathbf{c}$  at island boundaries, the orientational elasticity of the  $\mathbf{c}$ -director field gives rise to long-range texture-mediated effective interactions between islands [72].

The Frank elastic free energy density of a thin SmC

film is  $f_{el} = \frac{1}{2}K_s(\nabla \cdot \mathbf{c})^2 + \frac{1}{2}K_b(\nabla \times \mathbf{c})^2$ , where  $K_s$  and  $K_b$  are the splay and bend elastic constants, respectively. The orientation of the  $\mathbf{c}$ -director can alternatively be specified by the azimuthal orientation  $f$  of  $\mathbf{c}$  in the plane of the film, in terms of which

$\mathbf{c}(x, y) = [\cos \phi(x, y), \sin \phi(x, y)]$ . In the one elastic constant approximation ( $K_s = K_b = K$ ), the Frank elastic energy is proportional to the squared gradient of  $f$ ,  $f_{el} = \frac{1}{2}K(\nabla \phi)^2$ , and the total elastic free energy of the film is  $F_{el} = \frac{1}{2}K \int (\nabla \phi)^2 dxdy$ . In this approximation, therefore, a SmC film is a realization of the classical 2D XY model. Minimization of  $F_{el}$  leads to the Laplace equation,  $\nabla^2 \phi = 0$ , everywhere except at the location of point defects. Thus, there is a strong analogy between the  $\mathbf{c}$ -director structure of SmC films and 2D electrostatics, although treatment of SmC films with arbitrary boundary conditions requires both ‘electric’ and ‘magnetic’ charges [72].

Now consider a single circular island of radius  $a$  located at the center of a circular film of radius  $R$  ( $R \gg a$ ), with uniform  $\mathbf{c}$ -director orientation at the boundary of the film, and with strong tangential anchoring of the  $\mathbf{c}$ -director at the boundary of the island (the usual experimental boundary condition). Using plane polar coordinates, the boundary condition at the film edge can be expressed as  $\phi(R, \theta) = 0$  for all  $\theta$ , while the boundary condition at the edge of the island is chosen to be  $\phi(a, \theta) = \pi/2 + \theta$  (infinitely strong tangential anchoring). This boundary condition gives the island a topological charge of +1, but the uniform boundary condition at  $r = R$  implies that the net topological strength of the film is zero, so a -1 topological defect must also be present in the film surrounding the island. The pair of topological defects constitutes a dipole, which will interact with other pairs (islands) through a dipole-dipole interac-

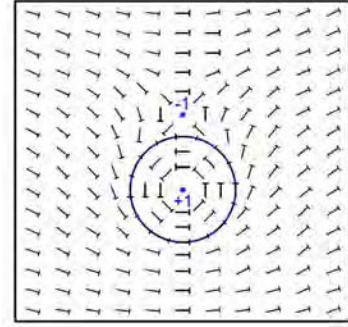


**Figure 2.21:** Topological defects and  $\mathbf{c}$ -director structure in the vicinity of an island in a thin SmC film, with strong tangential anchoring at the boundary of the island.

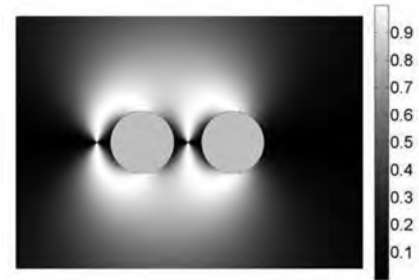


**Figure 2.22:** Equilibrium texture of a 2D smectic C liquid crystal for equally sized circular inclusions at the preferred separation, with free boundary conditions at infinity. A defect with topological charge -1 appears just to the left of each droplet. The brightness represents the square of the sine of the azimuthal orientation, which should be similar to what one would observe with crossed polarizers (from [74]).

tion. This situation is indicated schematically in **Figure 2.21**.

A solution to the Laplace equation in the region outside the island can be obtained by the method of images [72]. The boundary conditions at  $r = a$  and  $r = R$  can be satisfied (in the limit  $R \rightarrow \infty$ ) with three topological defects: a charge of strength -1 a distance  $r_d$  ( $r_d > a$ ) from the center of the island, and two charges inside the island, one of strength +2 at the center of the island and one of strength -1 a distance  $a^2/r_d$  from the center of the island. With this configuration of charges, the free energy of a single dipole is

$$F(r_d) = -\pi K \ln \left[ \left( a/r_d \right)^2 - \left( a/r_d \right)^4 \right] + \pi K \ln(a/\xi) + F_{core},$$

where  $\xi$  is the radius of the -1 defect exterior to the island and  $F_{core} \approx \pi K$  is the core free energy. This free energy is minimized for  $r_d = \sqrt{2}a$ .

The dipolar character of the orientation field surrounding an isolated island or inclusion gives rise to long-range effective interactions between inclusions resembling (but more complex than) interactions between electric or magnetic dipoles [72,73], leading to the formation of dipolar chains (**Figure 2.23**). The effective pair potential is attractive for large separations and repulsive for small separations (**Figure 2.23**), with a preferred center-to-center separation  $2\sqrt{2}a$  between two circular inclusions of equal radius  $a$ . Korolev and Nelson have coined the term ‘defect-mediated emulsification’ for this type of self-assembly, driven by effective interparticle interactions derived from interactions between topological defects [73]. Note that we could equally well have chosen the boundary condition at the edge of the island to be  $\phi(a, \theta) = -\pi/2 + \theta$  (c-director winding clockwise rather than counterclockwise – the mirror image of **Figure 2.21**). In other words, the director field

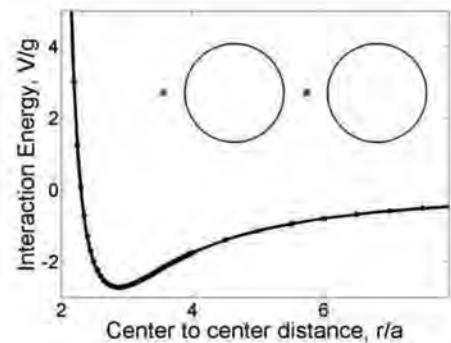


**Figure 2.23:** Pair potential for two inclusions of equal diameter (from [74]). The inset shows equilibrium locations of the two defects at the preferred separation, i.e. at the minimum of the pair potential. The defects prefer to lie on the center-to-center line, as shown on the inset, for all values of  $r$ .

surrounding an inclusion can have an intrinsic handedness or chirality, and both left-handed ( $L$ ) and right-handed ( $R$ ) islands will be present in general. In fact, roughly equal numbers of  $L$  and  $R$  islands are observed in experiments on islands in achiral or racemic smectic C films. In chiral smectic C films, islands of one handedness predominate, although both  $L$  and  $R$  islands are observed in films with moderate enantiomeric excess.

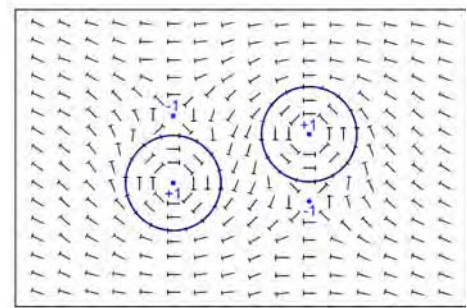


**Figure 2.24:** Preferred antiparallel (disclination quadrupole) arrangement of two smectic C islands of opposite handedness (schematic).

The interactions between islands of opposite handedness are qualitatively different from those between islands of the same handedness. In particular, islands of opposite chirality preferentially adopt a side-by-side antiparallel (quadrupolar) arrangement (**Figure 2.24**) instead of chains. This situation seems not to have been considered in prior theoretical work on the subject, but is evident experimentally in **Figure 2.6**.



The theory of inclusions in smectic C films has been extended by Patricio et al. to the case of unequal bend and splay elastic constants [74] and soft elliptical (deformable) inclusions [75]. The latter study was motivated by experimental studies of nematic droplets in smectic C films, in which the elasticity of the c-director field was observed to produce non-circular droplet shapes [76].

The behavior of smectic C films changes dramatically upon introduction of chirality, due to the fact that chiral smectic C materials are ferroelectric [77]. This introduces a ferroelectric polarization density  $\mathbf{p}(\mathbf{r})$  that is locally perpendicular to the c-director field, and implies an additional electrostatic energy contribution arising from space charge interactions,

$$F_{coul} = \frac{1}{2} \int d\mathbf{r} \int d\mathbf{r}' \frac{\nabla \cdot \mathbf{p}(\mathbf{r}) \nabla \cdot \mathbf{p}(\mathbf{r}')}{|\mathbf{r} - \mathbf{r}'|},$$

where  $\rho_b(\mathbf{r}) = -\nabla \cdot \mathbf{p}(\mathbf{r})$  is the polarization (bound) charge density associated with polarization splay (c-director bend). Because of this additional energy cost, bend deformations are strongly suppressed in high-polarization materials (polarization stiffening), and thermal fluctuations of the c-director field are strongly suppressed. These effects can be qualitatively taken into account in the theory by increasing the effective bend elastic constant. A formal procedure for renormalizing  $K_b$  to account for space charge effects has been derived in the strong-screening limit [77]. This increase in  $K_b$  leads to significantly stronger interactions between islands or inclusions, but arrays of islands display collective behavior that is quite similar to that observed in non-chiral films, namely the formation of dipolar chains. In fact, in thin smectic C films, dipolar chaining is often only observed in high-polarization ferroelectric films; in non-chiral films, thermal fluctuations in the c-director often prevent defect-mediated chain formation.

Such space charge effects modify the internal structure of islands, transforming the +1 disclination at the center of the island from a circumferential to a radial defect to eliminate polarization splay. The orientation at the center of the island in combination with tangential anchoring at the boundary of the island leads to a spiral c-director pattern, which winds either right or left depending primarily on the chirality of the smectic C.

#### 2.4.6 – HYDRODYNAMICS OF THIN SMECTIC FILMS

The hydrodynamic description of smectics is, in general, quite complex [2]. However, the hydrodynamics simplifies for ultra-thin, uniform SmA films (i.e., without dislocations), approaching the ideal case of a 2D fluid with a single relevant shear viscosity ( $\eta_2$  in the Martin-Parodi-Pershan notation [77], corresponding to in-plane shear). In this respect, thin SmA films resemble lipid bilayers. However, as discussed below, the two-dimensional character of smectic films is more pronounced than that of lipid bilayers, due to the low viscosity of the fluid surrounding smectic films (air) with respect to that surrounding a lipid membrane (water), enabling investigation of a distinct range of physical conditions.

Transport of proteins and other biomolecules in lipid bilayers has been intensively studied in recent years, due to the importance of protein diffusion in such processes as membrane-mediated cell signaling and endocytosis. Diffusion processes in lipid membranes were first analyzed by Saffman and Delbruck (SD) [78], who resolved the Stokes paradox (resulting from the divergence of the Stokesian velocity field of a moving object in a 2D fluid) by considering that a lipid bilayer is in fact a 3D system, since it is immersed in an aqueous medium. They used this fact to calculate the drag on a disk in a

lipid membrane in the limit in which the viscosity of the outer fluid is much less than that of the membrane, yielding a diffusion coefficient that decreases logarithmically with increasing radius of the diffusing disk, in contrast to ordinary Stokes diffusion, for which  $D \sim 1/a$ . However, recent experimental studies of the lateral mobility of proteins in membranes [79] find behavior consistent with the simple Stokes result and at odds with the SD result and its extensions [80], so the experimental situation remains somewhat unclear. It has been suggested that hydrodynamic stresses due to local deformation of the membrane by an inclusion can produce enhanced dissipation, leading to a  $1/a$  dependence of the diffusivity [80].

The viscous coupling of a membrane to the surrounding fluid introduces a crossover (SD) length scale  $\xi \approx \eta_m / \eta_f$ , where  $\eta_m$  and  $\eta_f$  are the viscosities of the membrane and surrounding fluid, respectively, and  $h$  is the membrane thickness. The diffusion coefficients of small (radius  $a \ll \xi$ ) inclusions in membranes are predicted to have a logarithmic dependence on their size, crossing over to  $1/a$  (Stokes) dependence for  $a \gg \xi$  [81]. Similarly, the hydrodynamic interactions between pairs of inclusions with a pair separation  $R$  should exhibit a crossover from quasi-2D behavior (strong coupling) for  $R < \xi$  to 3D behavior (weak coupling) for  $R > \xi$ . However, these predictions are difficult to test in lipid bilayers because the crossover lengthscale is small ( $\xi \sim 3 \mu\text{m}$ ). The situation is much more favorable in smectic films, owing to the low viscosity of the surrounding fluid (air) and the fact that the film thickness can be varied over a wide range. For smectic films, the crossover lengthscale ranges from  $\xi \sim 300 \mu\text{m}$  for a 2-layer film to  $\xi \sim 1500 \mu\text{m}$  for a 10-layer film, for example, enabling detailed tests of hydrodynamic models over a wide range of easily accessible experimental conditions. It should be possible, for example, to achieve a situation where  $\xi$  exceeds the linear length scale of a free-standing film or bubble, so that the entire film behaves like a 2D fluid (strong coupling regime), a previously unexplored regime of thin film hydrodynamics. The hydrodynamic behavior of inclusions in this regime is expected to depend strongly on boundary conditions. For example, the mobility is predicted to depend logarithmically on the size of the film or bubble, and should also depend strongly on the film topology (flat film vs. bubble).

Henle et al. have studied the hydrodynamics of inclusions in a spherical membrane [82], and find that their mobility is modified by both the curvature and topology of the membrane. The spherical topology necessarily leads to the appearance of vortices in the 2D interfacial velocity field [83] (Figure 2.25), and introduces a new length scale, the ra-

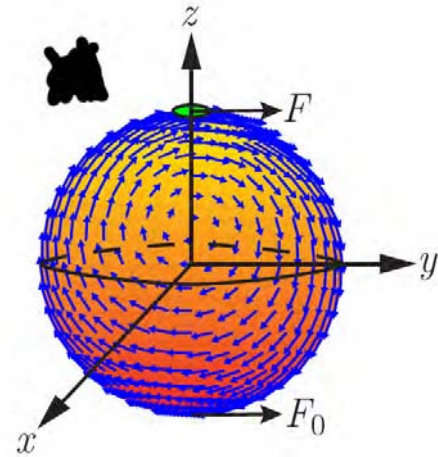


**Figure 2.25:** Schematic illustration and calculated membrane velocity field of a point particle of radius  $a$  (green disk) at the north pole subject to a force  $\mathbf{F}$ , with a pinning force  $\mathbf{F}_0$  at the south pole (from [82]). Here the viscosities of the interior and exterior fluids are identical,  $R/x = 0.1$  and  $R/a = 100$ .

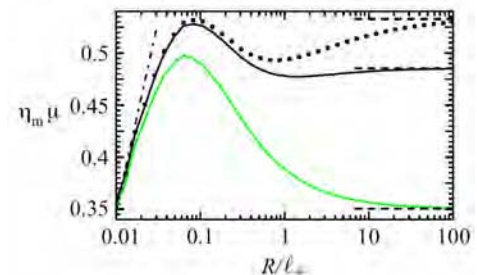


**Figure 2.26:** Dimensionless mobility  $\eta_m m$  for a particle at the north pole of a pinned spherical membrane as a function of the membrane radius  $R$ , for  $x_+ = 10 \text{ mm}$ ,  $a = 0.01 \mu\text{m}$ , and  $\eta_- = 10\eta_+$  (green curve),  $\eta_- = \eta_+$  (black curve), or  $\eta_- = 0.1\eta_+$  (dotted curve). The dashed and dot-dashed lines indicate the theoretical asymptotic results (from [82]).

dius of curvature  $R$ , which competes with the SD lengthscale  $\xi$ . This gives rise to a complex dependence of mobility on  $R$ , as shown in **Figure 2.26**, where the dimensionless mobility  $\eta_m m$  for a particle at the north pole of a pinned spherical membrane is plotted as a function of  $R$ , for various values of the inner viscosity  $\eta$  ( $\eta_-$  and  $\eta_+$  are the viscosities of the fluids inside and outside the membrane, respectively). In all cases, the flat interface SD result  $\eta_m \mu_{SD} \approx \ln(\xi/a)/4\pi$  is recovered in the limit  $R \rightarrow \infty$  (horizontal dashed lines), while  $\eta_m \mu \approx \ln(R/a)/2\pi$  for  $R \ll \xi$  (dot-dash line). The mobility for intermediate values of  $R$  can be either enhanced or reduced relative to the SD result, depending on the value of the inner viscosity.

#### 2.4.7 – THERMOCAPILLARY EFFECTS IN SMECTIC FILMS

Thermally induced surface tension and line tension gradients in freely suspended smectic films can drive fluid flow and dislocation motion, but such phenomena are difficult to study in terrestrial experiments, as they are typically obscured by other effects (e.g., flow driven by convective motion of the surrounding atmosphere). Thermocapillary effects in smectic films have been investigated by Godfrey and Van Winkle [84], who studied horizontal SmC films subjected to in-plane temperature gradients in an evacuated chamber, at a sufficiently low pressure ( $P_A \sim 1$  torr) to eliminate thermal convection. However, their experiment was dominated by thermocapillary flow in the meniscus, which drives (passive) flow in the smectic film, and so did not probe 2D thermocapillary effects within the thin smectic film itself.

Thermocapillary flow will result when forces arising from thermally induced gradients in surface tension are sufficiently large to overcome viscous forces. This is characterized by the dimensionless ratio of surface tension forces to viscous forces (the Marangoni number), which can be written:

$$Ma = \frac{d\gamma}{dT} \frac{\rho c_p \Delta T L}{\eta \kappa}$$

Here,  $\Delta T$  is the temperature difference over a characteristic lengthscale  $L$ ,  $\rho$  is the density,  $c_p$  is the specific heat, and  $\kappa$  is the thermal conductivity. Thermocapillary flow occurs above a critical Maragoni number of  $Ma_c = 80$ .

The surface tension is typically assumed to be a linear function of temperature,  $\gamma = \gamma_0 + \alpha(T - T_0)$ , where  $\alpha$  is the excess surface entropy. In most fluids,  $\alpha < 0$ , so that thermocapillary flow is from hot regions to cold regions (antiparallel to the temperature gradient). In liquid crystals, by contrast, orientational ordering near the surface yields a positive excess surface entropy ( $\alpha > 0$ ), inducing flow parallel to the temperature gradient ( $\alpha \sim 0.2$  dyne / (cm °C) in smectics [84]).

In thin smectic films, we can assume that flow occurs only in the plane of the film (flow in the layer normal direction (permeation) is strongly suppressed by smectic layering), and we can neglect inertial effects (low Reynolds number), so the flow velocity  $\mathbf{v}$  is governed by the 2D Stokes equations for an incompressible fluid, supplemented by a term involving the surface tension gradient:

$$\eta \nabla^2 \mathbf{v} = \nabla P - \nabla \gamma / h$$

$$\nabla \cdot \mathbf{v} = 0$$

The temperature distribution within the film is determined by the temperature equation:

$$\frac{\partial T}{\partial t} + (\mathbf{v} \cdot \nabla)T = \kappa \nabla^2 T$$

One must also consider radiative exchange of energy between the film and the chamber walls, heat conduction through the surrounding atmosphere, and viscous coupling of flow in the film to the surrounding atmosphere. The latter two effects were largely absent in the low-pressure experiments of Godfrey and Van Winkle [84], but radiative effects are always present, and are quite important in thin smectic films due to their large surface to volume ratio. Radiative effects tend to equalize the temperature throughout the film, and consequently decrease the distance over which temperature gradients can be maintained near heat sources and sinks.

In addition to in-plane flow in a uniform film induced by temperature-induced variations in surface tension, thin smectic films exhibit a variety of other thermocapillary effects, including:

- In the absence of flow, local variations in surface tension can produce local changes in film curvature, consistent with the Young-Laplace formula. For example, it should be possible to observe bulging or flattening of a smectic bubble in response to local heating of the film.
- For small Marangoni numbers, it is possible to impose a temperature gradient in a smectic film without inducing surface tension-driven flow. In this case, an in-plane pressure gradient arises in response to capillary forces, consistent with the Stokes equations ( $\nabla P = \nabla \gamma / h$ ). Such local variations in pressure and surface tension will alter the rate of island or pore nucleation, and may be employed to create islands or pores in a controlled way.
- A thickness-dependent excess surface entropy produces thermocapillary forces on dislocation loops in a temperature gradient. Assuming a linear variation of surface tension with temperature, the thermodynamic force on a island or pore is  $\mathbf{F} = A(\alpha_2 - \alpha_1)\nabla T$ , where  $A$  is the area of the dislocation loop and  $\alpha_1$  ( $\alpha_2$ ) is the excess surface entropy inside (outside) the dislocation loop. This effect will drive motion of islands or pores either parallel or antiparallel to a temperature gradient (depending on the sign of  $\alpha_2 - \alpha_1$ ).
- Temperature gradients can produce flow along edge dislocations, due to a temperature-dependent dislocation line energy  $\lambda(T)$ . This will induce circulatory flow along the boundary (and in the interior) of an island or pore, driving motion of islands or pores parallel or antiparallel to the temperature gradient (depending on the sign of  $d\lambda(T)/dT$ ).

It should be possible to observe all of these effects in appropriately prepared freely suspended smectic bubbles.

## 2.5 – PROPOSED THEORETICAL WORK

The theoretical component of the OASIS project will focus on the development of theoretical models for the analysis and interpretation of the proposed experiments. Proposed theoretical activities include:

### 2.5.1 – MESOSCOPIC MODELS OF DISLOCATION LOOP DYNAMICS

We will pursue the development of a comprehensive model of dislocation loop dynamics, appropriate for modeling the proposed island coarsening experiments. Our initial efforts will focus on extending the dissipation theorem-based approach of Oswald and

co-workers [36] to model the Ostwald ripening of collections of dislocation loops in smectic bubbles, including relatively weak effects such as a Burgers vector-dependent dislocation line tension (which generates in-plane pressure differences across island boundaries) and film thickness-dependent surface tension and disjoining pressure (which determine the relative stability of regions of varying thickness), consistent with the global constraints imposed by the bubble geometry (in which bubble diameter is determined by the Laplace pressure difference between the interior and exterior of the bubble). Subsequent versions of the theory will incorporate the effects of island coalescence on coarsening dynamics by including binary collisions between islands in the dynamical equations, and will consider more complicated topologies (e.g., nested dislocation loops). The results of numerical simulations of dislocation loop dynamics will be compared with experiment and with approximate analytic theories of coarsening dynamics (e.g., the Lifshitz-Slyozov-Wagner theory of Ostwald ripening, appropriately generalized to 2D).

### 2.5.2 – TEXTURE-MEDIATED INTERACTIONS IN SMECTIC FILMS

Experimental observations of islands in thin, achiral SmC films show that texture-mediated interactions between islands, deriving from the orientational elasticity of the c-director field, are relatively weak and strongly fluctuating, leading to weak long-range spatial correlations between islands. The situation is dramatically different in chiral SmC films, where the electrostatic energy of polarization space charge associated with splay in the ferroelectric polarization field (bend in the c-director field) causes “stiffening” of the c-director field, suppressing fluctuations and producing strong, long-range texture-mediated interactions between islands and defects (evident in the formation of well-ordered dipolar chains of islands, for example). In the strong screening limit (e.g., where polarization space charge is effectively screened by ionic impurities), the electrostatic interactions can be subsumed into a renormalized bend elastic constant [77], but no general theory applicable to the weak-screening limit has appeared. To better understand interactions and organization of islands in SmC films, we will develop finite-element models of texture-mediated interactions incorporating long-range electrostatic interactions and elastic constant anisotropy. We will also investigate fluctuation-mediated (pseudo-Casimir) interactions between islands and defects in achiral SmC films.

### 2.5.3 – STRUCTURE AND INTERACTIONS OF EDGE DISLOCATIONS IN SMECTIC FILMS

Optical trapping experiments that probe short-range interactions between large Burgers vector dislocation loops in non-polar SmA films reveal a short-range repulsive interaction that acts as a barrier to island coalescence. The physical origin of this short-range repulsion remains mysterious; in particular, it is unknown whether this is a general feature of large Burgers vector dislocations (even in bulk smectics), or whether this behavior is specific to dislocations in thin films. Linear elastic theory of bulk smectics predicts that the pair interaction (Peach-Koehler interaction) between small Burgers vector dislocations vanishes for dislocations whose separation vector is parallel to the smectic layers [49], but interactions between large Burgers vector dislocations have not, to our knowledge, been investigated theoretically, nor has the contribution of nonlinear elasticity to dislocation interactions been evaluated. The thin film geometry is thought to strongly modify the structure of elementary dislocations, reducing the lateral extent of layer deformations by an order of magnitude relative to dislocations in bulk smectics [49], but the effect of structural modification on dislocation interactions has not been studied. We will pursue a better understanding of edge dislocation structure, energetics



(e.g., the dependence of defect line tension on Burgers vector) and interactions in thin smectic films via molecular simulation and phenomenological theory (Landau-de Gennes theory). A significant advantage of this approach relative to elastic theory is that molecular simulation and Landau-de Gennes theory permit the structure of the dislocation core and effective interactions deriving from core overlap to be modeled explicitly.

## 2.6 – MOTIVATION FOR MICROGRAVITY RESEARCH

FSLC films exhibit a combination of physical characteristics that have made them uniquely exciting systems for the study of equilibrium and out-of-equilibrium phenomena in reduced dimensionality, for example liquid crystal ordering and fluctuations in two dimensions, and the effects of finite size on liquid crystal phase transitions. Here we show that FSLC films in microgravity present extraordinary opportunities for the study of fluid dynamic and thermodynamic behavior in reduced dimensionality, and for the exploration of fundamental nonequilibrium fluid interfacial phenomena.

The key relevant FSLC film properties are as follows: (i) The smectic layering forces FSLCs to be quantized in thickness in integral numbers of layers (the layer number) and suppresses pore formation and bursting. This enables the formation in air of stable single component, layered, fluid, FSLC films as thin as a single molecular layer ( $\sim 3$  nm thick). (ii) The low vapor pressure of smectic-forming compounds enables the long term stabilization of these films, such that a given few layer thick film can be studied in the laboratory for many months. Such films are structures of fundamental interest in condensed matter physics. They are the thinnest known stable condensed phase structures and have the largest surface-to-volume ratio of any condensed phase preparation, making them ideal for studies of fluctuation and interface phenomena. (iii) The LC layering makes films of uniform layer number highly homogeneous in basic physical properties such as thickness, surface tension, and viscosity, and, away from the edges of the film, completely free of local pinning or other external spatial inhomogeneities. (iv) The interactions which are operative in liquid crystals are generally weak, leading to the easy manipulation of order by external agents such as applied fields and surfaces, and to significant fluctuation phenomena with extended spatial correlations. These fluctuation, field, and surface effects, combined with the wide variety of LC order parameters and symmetries, makes FSLC films a rich system for probing basic fluid physics.

### 2.6.1 – DECOUPLING FROM BULK

FSLC films can be made in planar (**Figures 2.1a,b,c,e**) or spherical-bubble (**Figures 2.1b, 2.3**) geometries. With horizontal flat films, near zero-g conditions for in-plane motion can be achieved. However, the behavior of such films, especially with respect to film thickness and island dynamics, is controlled to a significant extent by contact with a bulk reservoir of material at the boundary of the film holder, to which it is coupled through a meniscus (**Figures 2.10, 2.11**). As a result, the hydrodynamics and defect dynamics of the film is strongly influenced by the boundary (and by coupling to the bulk reservoir), obscuring many features of 2D film physics. For example, the growth (or shrinkage) of dislocation loops in smectic films is generally driven by the pressure difference between the film ( $P_{\text{film}} = P_{\text{atm}}$ ) and the meniscus ( $P_{\text{meniscus}} < P_{\text{atm}}$ ), and the resulting growth velocity is governed by dissipation due to flow of material through the meniscus [36,48]. In this process, the line tension of the dislocation loop plays essentially no role, as it is much smaller than the pressure difference  $DP = P_{\text{film}} - P_{\text{meniscus}}$ , precluding the study of the 2D version of Ostwald ripening, in which the line tension drives the growth of large dislocation loops at the expense of smaller ones. Similarly, the flow of material into the film boundary prevents the systematic study of effects such as coales-

cence of islands and hydrodynamic interactions between inclusions or islands in smectic films.

The undesirable effects of coupling to the bulk can be effectively eliminated by reducing the perimeter length and volume of the meniscus. Using smectic bubbles tethered on fine needles reduces the meniscus length by the ratio  $R/r_b$  relative to flat films. Ground-based experiments have shown that using razor-edged needles significantly reduces the size of the Plateau border, as shown in **Figure 2.1f**. When the bubble is to be inflated, the tethering needle tip is heated and LC injected, making a thick meniscus that can feed the bubble surface as it is inflated. When the desired radius is reached, the LC is withdrawn back into the needle leaving the bubble with a  $\mu\text{m}$ -scale meniscus that is isolated from the bulk LC, so that the bubble is effectively isolated (not in contact with a bulk reservoir). Under these conditions, the dynamics of dislocation loops will be dominated by Ostwald ripening and dislocation loop coalescence, and will be constrained by the constant bubble diameter (imposed via a constant Laplace pressure difference between the interior and exterior of the film).

Unfortunately, it is not possible to effectively use this isolated smectic bubble geometry in Earth's gravity. In a terrestrial environment the Perrin length for an island,  $k_B T/mg$ , will be small compared to the bubble size, meaning that the islands should sediment to the bottom of the bubble, which is what is observed. In microgravity, on the other hand,  $k_B T/mg$  will be large compared to the bubble size and the islands should be thermally dispersed over the bubble surface. *Microgravity conditions provide the only viable route to the creation of large, uniform, boundary-free fluid films for precision studies of defect dynamics and hydrodynamics in two dimensions.* Terrestrial experiments on the hydrodynamics of smectic films and bubbles are also hampered by flow induced by convection in the surrounding atmosphere. *Microgravity conditions largely eliminate convection, enabling high-precision studies of 2D hydrodynamics and thermocapillary effects in smectic films and bubbles.*

Finally, we note that the envisioned smectic bubbles are not, strictly speaking, boundary-free, as they are supported by a small needle with a diameter much smaller than that of the bubble. However, the presence of the needle can be advantageous, as it behaves like an inclusion that can be manipulated to induce flow in the bubble (e.g., to interact hydrodynamically with islands or other inclusions in the bubble), or (in smectic films with in-plane order) like a point defect with texture-mediated interactions with other topological defects in the bubble.

## 2.6.2 – COLLECTIVE BEHAVIOR OF ONE-DIMENSIONAL INTERFACES

The theoretical discussion of **Section 2.4** shows that the linear interfacial layer steps between regions of different thickness on a FSLC film are highly collective, both in their static and dynamic behavior, exhibiting both local energetics and dissipation, as well as nonlocal interactions enforced by constraints (such as volume conservation) and long ranged electrostatic interactions. The island emulsions visualized in **Figure 2.6** are an example involving both of these effects, representing a topologically stabilized emulsion of one-dimensional interfaces. Freely suspended bubbles in microgravity, without islands, convection, and sedimentation represent nearly ideal, physically and chemically homogeneous 2D fluid systems. This background translational symmetry makes FSLC films of great interest for the study of collective phenomena in 2D.

## 2.7 – KEY ISSUES WHERE KNOWLEDGE IS LACKING

### 2.7.1 – 2D HYDRODYNAMICS

The hydrodynamics of truly homogeneous boundary-free two-dimensional fluids has never been studied. Experiments on flowing soap films come the closest to an ideal situation but they are not of fixed thickness. Since in the simplest approximation the effective viscosity for in-plane flow is proportional to thickness, spatially inhomogeneous flows couple strongly to film thickness variations [85]. There are a variety of predictions concerning the effects of the coupling of a 3D viscous medium (in this case air) to flow in 2D that have never been tested, and are relevant in a variety of contexts, such as protein diffusion in biomembranes.

### 2.7.2 – PROBING THE COLLECTIVE BEHAVIOR OF 1D INTERFACES IN A 2D SPACE

3D coarsening dynamics in emulsions, foams, and other nonequilibrium systems is an important and relatively well-studied problem. 2D coarsening dynamics of 1D interfaces is of increasing importance, but detailed studies are complicated by the lack of appropriate model systems. The proposed bubble experiments offer a well-characterized, homogeneous platform for the study of both equilibrium and nonequilibrium behavior of collective systems of 1D interfaces in 2D. The collective behavior of edge dislocations is critical to understanding mechanics of solids, and there have been very few studies of such phenomena in fluids.

### 2.7.3 – INVESTIGATION OF THERMOCAPILLARY & MARANGONI EFFECTS

Thermocapillary effects in fluids are notoriously difficult to characterize in Earth's gravity due to the complicating effects of convection and chemical partitioning of components in thermal gradients. Marangoni effects and thermally generated instabilities are important nonequilibrium phenomena that appear when fluid interfaces are subjected to thermal gradients. Microgravity experiments are a route to more effective study of these effects.

### 2.7.4 – STUDY OF SURFACE TENSION AND LINE TENSION

Our ground-based experiments show that island dynamics can reveal a subtle dependence of surface tension on film thickness, which is impossible to detect, much less measure, with any of the standard techniques.

### 2.7.5 – TEXTURAL INTERACTIONS

Fundamental mysteries abound in the physics of topological defects, the understanding of interactions of colloidal inclusions in ordered phases, and the role of fluctuations in these phenomena. The proposed island interaction experiments offer opportunities to make advances in all of these areas. As discussed in **Section 1.2**, topological defects in the director field of tilted (SmC) films exhibit anomalous annihilation dynamics, which may be due to Casimir-like fluctuations that renormalize their interactions. Fluctuations may also play an important role in island interactions and thus in the stability of island emulsions in the SmC phase.

## 2.8 – SCIENCE OBJECTIVES IN MICROGRAVITY ENVIRONMENT

### 2.8.1 – STUDY OF 2D HYDRODYNAMICS

We will pursue detailed tests of theories of hydrodynamic flow, relaxation of hydrodynamic perturbations, and of hydrodynamic interactions in 2D. Freely suspended bubbles in microgravity, without islands, convection, and sedimentation, represent nearly

ideal, physically and chemically homogeneous 2D fluid systems for the precision study of 2D hydrodynamics. The effects of introducing islands will be studied, both as controllable inclusions that modify the flow and as markers of flow.

#### *2.8.2 – PROBING THE COLLECTIVE BEHAVIOR OF 1D INTERFACES IN A 2D SPACE*

The goal will be to study the behavior of collective systems of 1D layer step interfaces on 2D bubble surfaces, including the equilibrium spatial organization and interaction of islands, and the nonequilibrium coarsening dynamics of island emulsions. In addition to yielding information about a number of relatively weak physical effects (thickness-dependent surface tension and line tension, disjoining pressure, etc.), we anticipate that this will clarify the effects of dimensionality in coarsening dynamics (e.g., on dynamic scaling behavior).

#### *2.8.3 – INVESTIGATION OF THERMOCAPILLARY & MARANGONI EFFECTS*

We will carry out the first thermocapillary experiments on homogeneous two dimensional fluids. The proposed microgravity experiments present a unique opportunity to explore thermocapillarity and Marangoni effects, the translational symmetry of the smectics and absence of convection mitigating anomalous effects to the maximum extent possible, enabling detailed studies of these phenomena in 2D fluids.

#### *2.8.4 – STUDY OF SURFACE TENSION AND LINE TENSION*

We will study the dependence of surface tension and line tension on film thickness and Burgers vector. Ground-based experiments indicate that equilibrium and nonequilibrium island behavior should be sensitive to this dependence, enabling critical tests of extant theoretical predictions.

#### *2.8.5 – TEXTURAL INTERACTIONS*

We will probe the effects of a spontaneously broken symmetry in the 2D film surface (the appearance of 2D polar, XY-like ordering and accompanying electrostatic polarization) on the interaction of islands, exploring the stability of topologically stabilized emulsions of 1D interfaces in 2D.

#### *2.8.6 – ULTRAWEAK INTERACTIONS*

In ground based experiments under some circumstances, such as in the smectic A phase, islands appear to be noninteracting when not in contact, i.e., when they are apart the interactions are much weaker than spurious forces due to convective flow or flow induced by evolution of the meniscus structure. The OASIS experiment should enable long term study in absence of such effects as a probe of weak island or droplet interactions.

## 2.9 – CONCEPTUAL DESIGN OF THE PROPOSED FLIGHT EXPERIMENT

### 2.9.1 – GENERAL DESIGN CONSIDERATIONS

The experimental apparatus required to observe smectic islands in space will be developed around the Microgravity Science Glovebox (MSG), with the design based on proven, ground-based experimental hardware. A conceptual design of the modified MSG, showing the additional capabilities necessary to accommodate our experiment, is shown in **Figure 2.27**.

Each sample to be studied will require an independent Bubble Chamber (BC), each a small container including all of the hardware necessary to create, inflate, illuminate, position, manipulate, and observe liquid crystal bubbles and islands at low resolution. Different materials need to be kept separate in order to minimize cross-contamination: when a bubble breaks it is likely that fluid drops of LC material will be deposited on whatever is close at hand. Only the MSG objectives will be common to experiments on different samples, and will have to be cleaned with solvent by an astronaut when samples are changed.

The conceptual design will have four BCs, enabling the observation of four distinct LC materials, which will differ with respect to modes of inter-island interactions, or exhibit different phase sequences and transitions. These bubble chambers will either be individual units or be mounted on a linear conveyer belt-type sample changer so that they can be translated sequentially into the field of view of the microscope.

In either case, since many studies can be done using only the low-resolution video, experiments can be carried out simultaneously in all four BCs.

In each chamber, bubbles will be made using its Bubble Generation and Motion System (BGMS). LC material will be stored in the BGMS initially in a small cartridge (volume < 300  $\mu$ l). One end of this cartridge is attached to a pressure manifold, the other to a thin tube which leads to a pair of coaxial needles used to form the bubbles. The LC samples should be kept near room temperature and atmospheric pressure prior to use: during the experiments, the temperature of each bubble chamber would be controlled. Bubbles would be formed by a computer-controlled, automated sequence of steps: warming the coaxial needles; carefully expressing a small amount of LC material from the outer needle; and pushing air out of the inner needle in order to inflate the bubble. The bubble size will be determined and controlled using feedback from the macro-view camera and/or a position-sensitive detector. The bubble film thickness will be determined by optical reflection spectrometry.

Islands must then be generated on the bubble using one or more of four methods (i) shearing of the meniscus using extensional air flow (two needles placed close to the top of the bubble); (ii) inkjet printing (creating a relatively monodisperse collection of islands); (iii) local heating (the ends of the needles used for shearing can be heated); or (iv) pressure quenches (suddenly reducing the pressure inside the bubble). Island thickness will be measured using spectrophotometry to correlate interference color and/or intensity with the number of smectic layers.

Experimental observations of island interactions and dynamics will require both high-video microscopy with both large and small fields of view. Principal processes of interest include coarsening, coalescence, and diffusion of islands, island/hole generation, thermocapillary effects, and island interactions when placed in an external electric field (applied through the shearing needles). These experiments will be performed varying



the external stimuli such as magnitude of applied field and induced temperature (gradient), pressure oscillation frequency and quench depth, as well as bubble/island thickness and bubble size. Details of the proposed experiments are given below.

### 2.9.2 – DESIGN CONCEPT FEATURES

In general, the hardware development is based upon the following experimental requirements for each bubble chamber:

- **Automated Bubble Formation (Bubble Generation and Motion System)**
  - Coaxial needles, gas and LC injectors, valves (*for bubble generation, inflation, and tethering*).
  - Heating of tethering needle tip (*to pre-form the meniscus*).
  - Video observation.
  - Optical bubble size and film thickness measurement.
- **Gas Jets to Generate Bubble Flow**
  - Opposing needles tangent to bubble (*driving field for fluid dynamic experiments and creation of island emulsions*).
  - Offset needles tangent to bubble (*driving rotational flow of bubble*).
- **Inkjet Deposition of Single Islands or Drops (Inkjet Drop Dispenser, IDD)**
- **Observation by Reflected Light Imaging**
  - Macro-view digital video (macroDV) using hemispherical illumination (*to observe the bubble inflation, global bubble structure, global interface organization*).
  - Micro-view digital video (microDV) microscopy (*to observe the generated islands on the bubble, island structure and dynamics, and the orientational textures, using the LMM Leica M4000 or equivalent system*).
- **Spectrophotometry** (*SPEC and/or image color analysis, for island thickness measurement, using the LMM Leica M4000 or equivalent system*)
- **Electric Field Application** (*to induce island motion and interaction*).
  - Needle electrodes, including tethering needle.
- **Heating**
  - Overall temperature control of chamber (*to assess behavior near phase transitions*).
  - Local heating of needle tips (*to generate islands, pores, and thermocapillarity effects*).
- **Dynamic Bubble Inflation and Deflation** (*pressure jumps to nucleate or remove islands and/or pores*).
- **Motion Control**
  - positional control of chamber (X-Y-Z)
  - positional control (X-Y) of the tethering needle (LGMS)

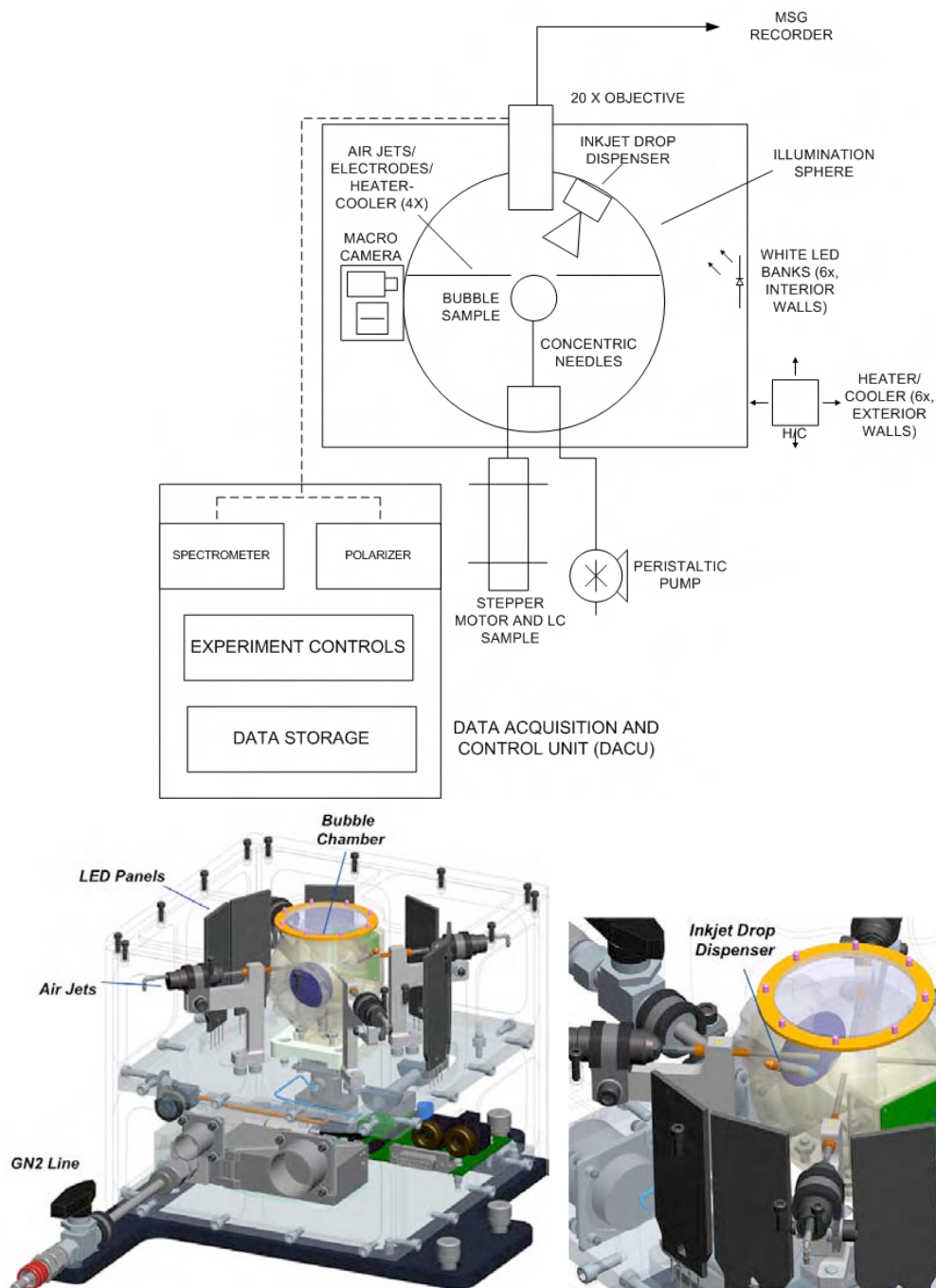


**Figure 2.27:** OASIS experimental concept. (top) Functional schematic. The bubble can be observed simultaneously with high magnification from above (the micro view camera, with 20x objective) and with low magnification video from the side (the macro view camera). Each experiment module includes hardware to inflate the bubble, four air jets used to generate islands, and to apply electric fields and temperature gradients to manipulate the islands (two of the airjet needles also serve as electrodes while the other two are a heater/cooler tandem), heater banks, and a water/glycerol dispenser. (bottom) OASIS experiment module. In the overview at left, the MSG GN2 (Gaseous Nitrogen) line is shown at lower left. The air jets, white light LED panels for illumination, and bubble chamber are shown with the external housing semi-transparent for clarity. The detailed view at right shows the bubble chamber with the inkjet drop dispenser, macro view camera, and four airjet needles.

## 2.10 – ANTICIPATED KNOWLEDGE TO BE GAINED: VALUE AND APPLICATIONS

### 2.10.1 – 2D HYDRODYNAMICS

The two dimensional hydrodynamics of truly homogeneous two dimensional fluids has never been studied. Freely suspended bubbles without islands represent nearly ideal, physically and chemically homogeneous 2D fluid systems for the precision study of 2D hydrodynamics. In microgravity, the absence of convection and sedimentation enables the study of the hydrodynamics of inclusions (islands) in a nearly ideal 2D fluid. This will enable detailed tests of theories of diffusion, relaxation of hydrodynamic perturbations, and of hydrodynamic interactions in 2D.

### 2.10.2 – COARSENING, OSTWALD RIPENING DYNAMICS, AND ISLAND AND DROPLET INTERACTION

3D coarsening dynamics in emulsions, foams, and other nonequilibrium systems is an important and relatively well-studied problem. 2D coarsening dynamics of 1D interfaces is of increasing importance, but detailed studies are complicated by the lack of appropriate model systems. The proposed bubble experiments offer a well-characterized, homogeneous platform for the study of 2D coarsening dynamics. In addition to yielding information about a number of relatively weak physical effects (thickness-dependent surface tension and line tension, disjoining pressure, etc.), we anticipate that this will clarify the effects of dimensionality in coarsening dynamics (e.g., on dynamic scaling behavior), and enable study of weak interactions between islands and droplets.

### 2.10.3 – THERMOCAPILLARY EFFECTS

Thermocapillary effects in fluids are notoriously difficult to characterize in Earth's gravity due to the complicating effects of convection and chemical partitioning of components in thermal gradients. Our proposed microgravity experiments with one-component smectic materials will mitigate these effects to the maximum extent possible, and will enable detailed studies of the thermocapillarity of fluid interfaces. These will be the first thermocapillary experiments on homogeneous two dimensional fluids.

### 2.10.4 – SURFACE TENSION AND LINE TENSION

Our ground-based experiments show a subtle dependence of surface tension on film thickness, which is impossible to detect, much less measure, with the standard techniques. This indicates that a possible outcome of the coarsening experiments will be information about the thickness dependence of surface tension. These experiments may also yield information about the Burgers vector dependence of the dislocation line tension, enabling critical tests of extant theoretical predictions.

### 2.10.5 – PERTURBING SMECTIC BUBBLES

The suite of proposed perturbation experiments (local heating, pressure quenches, electric field application, non-uniform flow) are relatively simple experiments which, in the context of free-standing smectic bubbles, probe unique physical states and interfacial conditions, enabling the study of hitherto unexplored fluid phenomena.

### 3 – JUSTIFICATION OF EXTENDED DURATION OF MICROGRAVITY ENVIRONMENT

#### 3.1 – LIMITATIONS OF TERRESTRIAL EXPERIMENT

As discussed above, there are a variety of 2D fluid phenomena that are difficult or impossible to study in terrestrial experiments under Earth's gravity. In the typical freely suspended smectic film geometry, the boundary of the film plays a dominant role in dislocation dynamics, providing the driving force for dislocation motion (the Laplace pressure difference between the film and the meniscus) and controlling the rate of dislocation motion (via dissipation due to flow of material through the meniscus). The dominant influence of the film boundary obscures a variety of more subtle effects, including those due to Burgers vector-dependent dislocation line tension, disjoining pressure, and thickness-dependent surface tension. While the role of boundary conditions can be greatly reduced in the bubble geometry, gravity-driven sedimentation invariably produces inhomogeneities in film thickness, precluding the formation of large, homogeneous, boundary-free films in Earth's gravity. It is also quite difficult to eliminate gravity-driven convection due to thermal gradients in terrestrial experiments, making precision studies of 2D hydrodynamics and thermocapillary effects in smectic films problematic at best.

#### 3.2 – LIMITATIONS OF DROP TOWER AND PARABOLIC FLIGHT EXPERIMENTS

The amount of time needed for generating smectic bubbles and doing experiments greatly exceeds that available in a drop tower or on a parabolic flight. Ground studies of the generation of bubbles, the creation of island emulsions and island coarsening processes indicate a characteristic time scale of about one hour for the islands to substantially merge. Our results from the experiments of hydrodynamics of thin smectic films, texture-mediated interactions, and Marangoni effects on freely suspended films indicate even longer times. We also expect that Ostwald ripening toward equilibrium continues for more than several hours.

#### 3.3 – LIMITATIONS OF MODELING

Analysis and interpretation of results from the proposed experiments requires a range of theoretical modeling activities, including microscopic modeling of dislocation structure, energetics, and interactions, and mesoscopic and macroscopic modeling of the hydrodynamics and collective dynamics of dislocation loops. The limitations of modeling are of two types: (1) lack of knowledge of appropriate physical parameters for input into theoretical models; (2) lack of validated models of the physical processes involved. The proposed experiments are designed to overcome these limitations by providing a versatile experimental testbed for parametrization, validation, and refinement of theoretical models.

#### 3.4 – NEED FOR MICROGRAVITY SCIENCE GLOVEBOX (MSG)

The MSG is a flexible, multi-user facility with an enclosed 255-liter work area accessible to the crew through sealed glove ports and to ground-based scientists through real-time data links and video. The MSG can provide power and data for the OASIS experiment, with dedicated video resources for live downlink or video recording, digital photography, and sensors for monitoring experiment health and status in real time. The MSG laptop computer (MLC) provides server software for experimental control and can also accommodate the switch-out of the planned OASIS components.

## 4 – EXPERIMENT DETAILS

### 4.1 – FLIGHT EXPERIMENT PLAN AND PROCEDURES

#### 4.1.1 – PRE-FLIGHT PROCEDURES

##### *Sample Containment and Preparation*

- Each of the four liquid crystal samples will be preloaded into its own ~10 cm x 5 cm x 5 cm Bubble Chamber (BC) containing all of the hardware necessary to create, inflate, position, manipulate, and observe its bubbles and islands at low resolution. In each chamber, the LC material will be stored in a small cartridge (volume < 300  $\mu$ l). There will be four BCs altogether, either as individual units or as part of a larger assembly.
- The BCs will be kept at room temperature and atmospheric pressure.

#### 4.1.2 – IN-FLIGHT PROCEDURES

##### *Experiment Preparation*

The experiment can be performed either in the Microgravity Science Glovebox or in the Light Microscopy Module (LMM). One BC unit will be positioned under the micro-view camera objective. If the BCs are individual units, then when experiments are completed on one unit it will be removed and a second unit placed in either the LMM or MSG by an astronaut. If the BCs are part of a larger assembly on a translator, then they can be exchanged automatically. Steps not requiring the micro-view digital video (i.e., everything except  $\mu$ DV and SPEC) can be run simultaneously in more than one BC.

For each new bubble, the following protocol would be executed sequentially, requiring no astronaut involvement:

**Bubble Creation (BGMS, MDV, LR/LCCD)** – Automated sequence by the BGMS: heat co-axial needle tip, expel small amount of LC, pressurize gently to blow bubble, monitor size, maintain desired size.

**Bubble Observation (MDV)** – Observation of advance of bubble; feedback loop to control size near final working diameter.

**Bubble Thickness Measurement (LR/LCCD)**

These basic bubble creation steps would enable one of the following choices of experiments:

**Island or Droplet Creation (gas jets, IDS, MDV,  $\mu$ DV)** – Use of air nozzles, inkjet printing, local heating, or pressure quenches.

**Island Thickness Measurement ( $\mu$ DV, SPEC)** – optical reflection spectrophotometry

**Island Experiments** – (BGMS, gas jets, electrodes, MDV,  $\mu$ DV) One or more of the following to be performed on each sample, all requiring only minimal astronaut involvement. These experiments would be performed varying the external stimuli such as magnitude of applied field and induced temperature (gradient), pressure oscillation frequency and quench depth, as well as bubble/island thickness and bubble size:

- *island coarsening* – (MDV,  $\mu$ DV) Do small islands in an ensemble shrink while large ones grow (Ostwald ripening)?
- *island coalescence* – (MDV,  $\mu$ DV) Do islands in an emulsion encounter one another on the bubble surface and merge together to form larger, thicker islands?



- island hydrodynamics – ( $\mu$ DV) apply voltage to air nozzles to briefly trap an island or islands then observe Brownian diffusion on the bubble.
- island/hole generation – (BGMS, MDV,  $\mu$ DV) apply sudden pressure quenches to generate islands, pressure steps to create holes; effects on islands of oscillating bubble pressure.
- thermocapillary effects – (needle tip heaters, MDV,  $\mu$ DV) heat needle tip near bubble (e.g., the air nozzles) to cause temperature gradient, then observe flow, textural changes, island rearrangement.
- island interactions – (MDV,  $\mu$ DV) Do charged or polar islands interact differently from non-charged ones?
- island interaction with external electric field – (electrodes, MDV,  $\mu$ DV) formation and interaction of island chains; field-induced textural changes; relaxation after field removal.

**Droplet Experiments** – (BGMS, gas jets, electrodes, MDV,  $\mu$ DV) One or more of the following to be performed on a sample, all requiring only minimal astronaut involvement. These experiments would be performed varying the external stimuli such as magnitude of applied field and induced temperature (gradient), as well as bubble/island thickness and bubble size:

- droplet coarsening – (MDV,  $\mu$ DV) Do small droplets in an ensemble shrink while large ones grow (Ostwald ripening)?
- droplet coalescence – (MDV,  $\mu$ DV) Do droplets in an emulsion encounter one another on the bubble surface and merge together to form larger, thicker islands?
- thermocapillary effects – (needle tip heaters, MDV,  $\mu$ DV) heat needle tip near bubble (e.g., the air nozzles) to cause temperature gradient, then observe flow, textural changes, droplet rearrangement.
- droplet interaction with external electric field – (electrodes, MDV,  $\mu$ DV) formation and interaction of droplet chains; field-induced textural changes; relaxation after field removal.

#### 4.2 – FLIGHT EXPERIMENT TESTS

For each liquid crystal sample, first the bubble will be created, then islands (droplets) will be generated (deposited) on the bubble. Island or droplet behavior (including hydrodynamics, coalescence and response to external fields) will then be observed. We require the continuous down-linking of the macro-view camera and micro-view camera to monitor bubble formation, island generation, and the film and island configuration during the experiments.

*Table 4.1 – Flight Experiment Tests*

<b>Test Number</b>	<b>Required Hardware Operation Mode</b>	<b>Control Parameters and Change of Physical Parameters</b>	<b>Parameters to be Measured</b>
<b>1. Single bubble creation</b>	<b>(BGMS, MDV, <math>\mu</math>DV)</b> <ul style="list-style-type: none"> <li>• heating the coaxial needle tip</li> <li>• expelling small amount of liquid crystal material from outer needle</li> <li>• introducing low flow of air into inner needle to form and expand the bubble</li> <li>• illumination of bubble</li> <li>• observation of bubble growth with macro-view camera</li> <li>• measurement of bubble size and thickness using macro-video and reflection spectroscopy</li> <li>• retraction of meniscus</li> </ul>	<ul style="list-style-type: none"> <li>• BC temperature control (+ 0.5°C over 25–70°C)</li> <li>• raise needle tip temperature for ~ 1 min (or as long as it takes to blow a bubble) to between 25°C and 75°C depending on sample</li> <li>• adjust intensity of illumination</li> <li>• bubble positioning</li> <li>• bubble size control</li> </ul>	<ul style="list-style-type: none"> <li>• BC temperature</li> <li>• bubble size</li> <li>• bubble film thickness</li> <li>• observation with macro-view camera (continuous)</li> </ul>
<b>2a. Creation of islands on the bubble</b>	<b>(gas jets, heaters, MDV, <math>\mu</math>DV, BGMS)</b> <ul style="list-style-type: none"> <li>• islands created using one of four techniques (i) extensional air flow, (ii) local heating, or (iii) sudden bubble shrinkage (dynamic deflation, pressure quenching)</li> </ul>	<ul style="list-style-type: none"> <li>• gas jet, heater, inflation control</li> <li>• bubble positioning</li> <li>• bubble size control</li> </ul>	<ul style="list-style-type: none"> <li>• observation with MDV and <math>\mu</math>DV (continuous)</li> <li>• number of islands</li> <li>• size of islands</li> <li>• thickness of islands</li> </ul>
<b>2b. Creation of droplets on the bubble</b>	<b>(gas jets, MDV, <math>\mu</math>DV, IDD, BGMS)</b> <ul style="list-style-type: none"> <li>• fluid droplets deposited on the film using the IDD</li> </ul>	<ul style="list-style-type: none"> <li>• gas jets control bubble flow</li> <li>• IDD (number of droplets)</li> <li>• bubble size control</li> </ul>	<ul style="list-style-type: none"> <li>• observation with MDV and <math>\mu</math>DV (continuous)</li> <li>• number of droplets</li> <li>• size of droplets</li> </ul>

Table 4.1 – Flight Experiment Tests (continued)

Test Number	Required Hardware Operation Mode	Control Parameters and Change of Physical Parameters	Parameters to be Measured
<i>3a,b. Observa- tion of evolution of islands and emulsions for extended period of time, global bubble structure, ripening, and coalescence</i>	<i>(MDV, <math>\mu</math>DV, LR/LCCD, SPEC)</i>  <ul style="list-style-type: none"> <li>• macro- and micro-view camera observation</li> <li>• measurement of film and island thicknesses</li> <li>• measurement of droplet size</li> </ul>	<ul style="list-style-type: none"> <li>• bubble positioning</li> <li>• bubble size control</li> </ul>	<ul style="list-style-type: none"> <li>• BC temperature</li> <li>• MDV, <math>\mu</math>DV video observation</li> <li>• bubble film thickness</li> <li>• island thickness</li> </ul>
<i>4a,b. Observa- tion of electric field-induced island and drop- let interactions and effects on orientational textures</i>	<i>(electrodes, MDV, <math>\mu</math>DV)</i>  <ul style="list-style-type: none"> <li>• macro- and micro-view camera observation of island positions</li> <li>• macro- and micro-view camera observation of droplet positions</li> </ul>	<ul style="list-style-type: none"> <li>• apply voltage (~100 kV/m from dc to 10 kHz) to the needle electrodes during the observation period</li> <li>• bubble positioning</li> <li>• bubble size control</li> <li>• switch between normal (unpolarized) reflection and depolarized reflection modes</li> </ul>	<ul style="list-style-type: none"> <li>• BC temperature</li> <li>• applied voltage</li> <li>• observe textures (e.g. strings) and spatial arrangements (patterns) of island or droplet emulsions</li> </ul>
<i>5a,b. Study of hydrodynamics of islands or droplets and film flow</i>	<i>(electrodes, gas jets, MDV, <math>\mu</math>DV)</i> <ul style="list-style-type: none"> <li>• induce bubble flow</li> <li>• macro- and micro-view cameras</li> </ul>	<ul style="list-style-type: none"> <li>• initial trapping of island(s) by electric field</li> <li>• bubble positioning</li> <li>• bubble size control</li> </ul>	<ul style="list-style-type: none"> <li>• BC temperature</li> <li>• position of observable features</li> </ul>
<i>6. Study the process of nucleation of islands and pores</i>	<i>(electrodes, <math>\mu</math>DV, MDV, BGMS, LR/LCCD, SPEC)</i> <ul style="list-style-type: none"> <li>• perturb the equilibrium state of the islands by dynamic deflation and inflation</li> <li>• macro- and micro-view camera observation</li> <li>• measurement of film and island thickness</li> </ul>	<ul style="list-style-type: none"> <li>• bubble positioning</li> <li>• bubble size control</li> </ul>	<ul style="list-style-type: none"> <li>• BC temperature</li> <li>• appearance and disappearance of islands</li> <li>• island and film thickness</li> </ul>

*Table 4.1 – Flight Experiment Tests (continued)*

<i>Test Number</i>	<i>Required Hardware Operation Mode</i>	<i>Control Parameters and Change of Physical Parameters</i>	<i>Parameters to be Measured</i>
<b>7a,b. Observation of temperature gradient-induced (thermocapillary) flow and its effect on island or droplet organization and dynamics</b>	<p><b>(needle heaters, MDV, <math>\mu</math>DV)</b></p> <ul style="list-style-type: none"> <li>• macro- and micro-view camera observation</li> <li>• observation of island interactions</li> <li>• observation of textures</li> </ul>	<ul style="list-style-type: none"> <li>• up to 30°C/cm temperature gradients induced by heating air nozzle or bubble generation needles</li> <li>• vary gradient during the observation period</li> <li>• bubble positioning</li> <li>• bubble size control</li> <li>• switch between normal (unpolarized) reflection and depolarized reflection modes</li> </ul>	<ul style="list-style-type: none"> <li>• BC temperature</li> <li>• island motion</li> <li>• observe textures (e.g. strings) and spatial arrangements (patterns) of island emulsion</li> </ul>

#### 4.3 – POST-FLIGHT DATA HANDLING AND ANALYSIS

Analysis will require complete frame-by-frame, time-stamped video data, together with simultaneous records of measured quantities (e.g., temperature, voltage), any astronaut procedures (audio), and user commands (computer log).

#### 4.4 – GROUND TEST PLAN

##### 4.4.1 – FLIGHT HARDWARE DEVELOPMENT

- **Preliminary Engineering Model** – a preliminary engineering model of the Bubble Chamber will be developed in our laboratory, including the Bubble Generation and Motion System (BGMS) and the other functionality indicated in **Figure 2.27**.
- **Improved MDV Illumination** – for example, high-power, sheet LEDs for the macro-view digital video (MDV) observations.
- **Razor-Sharp Bubble Generation Needles** – Initial experiments have shown that using razor-edged needles can significantly reduce the size of the Plateau border, as shown in **Figure 2.1d**. These effects of needle geometry will be investigated further.
- **Inkjet Printing of Droplets** – We propose to explore applying inkjet printing technology to prepare well-defined, monodisperse arrays of a finite number of islands. This method will also potentially allow the study of the interactions of droplets of liquid crystals in different phases, or of isotropic liquid droplets, deposited onto films.
- **Confirm Parameter Ranges** – for individual experiments, e.g., temperature gradient magnitude for thermocapillary effects; volume change for sudden deflation to produce islands and dependence on temperature, bubble size, etc.; electric field strength necessary to cause island trapping and chaining.

- **Contamination Issues** – Whenever a bubble breaks, there will be drops of its LC deposited onto the walls of the bubble chamber, the optics, and the microscope objective. We will probe how fast this material, a contaminant if a bubble of a different material is subsequently made in the same chamber, will be transferred via LC vapor to the new bubble.
- **Bubble Size Measurement** – Use macro-view video to monitor bubbles near working size. Design of active feedback electronics to control/maintain final bubble size.
- **Bubble and Island Thickness Measurements** – Implement visible light reflection measurement for bubble thickness. Calibrate the microscope illumination/spectrometer/video camera system for measuring thickness of colored islands.

#### 4.4.2 – PROPOSED GROUND-BASED EXPERIMENTS

**Optical Trapping of Islands and Interaction Measurement** – We propose to continue to use multiple optical trapping techniques to study island interactions and to observe the c-director (the azimuthal orientation field of the local plane of tilt of the molecules in the SmC) and polarization orientation in high polarization SmC films. R. Meyer at Brandeis University recently described a textural transformation in islands from pure bend to reversing spiral due to a strong correlation between the spontaneous electrical polarization of the ferroelectric phase and the apparent difference between the bend and splay elastic constants. In this study, we will continue to study textural transformations both inside (+1 defect) and outside (-1 defect) islands on very high polarization ( $>200$  nC/cm<sup>2</sup>) films. Another goal is to develop simulation techniques to be able to compute the c-director orientation on high polarization SmC\* films. We plan to calculate the effective interaction between two disk-defect pairs using a two-dimensional elastic free energy with different contributions for splay and bend deformations and to include the Coulomb energy due to polarization charges on the film.

**Island Generation via Inkjet Printing** – We propose to continue to develop inkjet techniques as a method for delivering droplets of liquid crystal. We will investigate whether we can print small volumes of nematic or smectic material onto films in order to generate islands directly. To compensate for the higher viscosity of smectics, the reservoir and print head may need to be heated. One of our goals is to use a relatively volatile liquid (such as a glycerol/water combination), or liquid crystal itself, to create monodisperse islands that have no remnant impurities in them and hence will be fully equivalent in all their physical properties to “natural” smectic islands.

**Parameter Measurement** – The theory outlined in **Section 2.4** presents and discusses the key materials parameters governing what behavior can be predicted for island dynamics and interactions on FSLC films. The need for quantitative understanding of these will be assessed on an ongoing basis and experiments designed to measure them.

#### 4.4.3 – GROUND-BASED THEORY

Theoretical work will be pursued in connection with the systems proposed for microgravity study and in support of ground-based experiments aimed at defining and motivating the space experiments. Extension of several key aspects of the current theoretical understanding of the collective behavior of 1D interfaces in 2D were presented in **Section 2.5**, including: mesoscopic modeling of dislocation loop dynamics; study of texture-mediated interactions in smectic films; and theory of the structure and interactions of edge dislocations in smectic films.

## 5 – SCIENCE EXPERIMENT REQUIREMENTS

The following **Sections** contain specific requirements necessary in order to fulfill the science mission for OASIS (Observation and Analysis of Smectic Islands in Space). The general purpose of OASIS is to explore and understand: (i) the 2D hydrodynamics of ultra-thin, uniform SmA films (i.e., without dislocations), approaching the ideal case of a 2D fluid with a single relevant shear viscosity; (ii) Ostwald ripening dynamics in arrays of islands/droplets on the surface of a smectic bubble, under conditions where coalescence is controlled by texture-mediated repulsion (e.g., in the SmC phase) or by direct island/droplet interactions (e.g., in the SmA phase of **8CB**); (iii) coarsening dynamics of arrays of islands/droplets on the surface of a smectic bubble, under conditions such that coalescence proceeds more rapidly than Ostwald ripening (e.g., in non-polar SmA films); (iv) thermocapillarity of an ideal 2D fluid; (v) electric field control of the collective behavior of weakly interacting islands/droplets.

### 5.1 – SCIENCE REQUIREMENTS SUMMARY TABLE

Table 5.1 Science Requirements Summary

<i>Item</i>	<i>Experiment Component</i>	<i>Science Requirement</i>
1	SECTION 5.1.1 OASIS HARDWARE UNITS	There shall be four separate OASIS hardware units. Each will have a separate enclosure in order to prevent cross contamination of the liquid crystal (LC) samples.
2	SECTION 5.1.2 BUBBLE CHAMBERS	Each bubble chamber shall have inner dimensions that accommodate a liquid crystal bubble of 15 mm diameter, the upper part of the bubble inflation device, the air jet needles, the electric field needles, the optics, and cameras so you can image the front of the bubble.
		Each bubble chamber shall be designed to provide as uniform illumination as possible of the half of the bubble facing the macro-view camera. A sphero-cylindrical shape is recommended around this half, with a black, matte screen behind the bubble in order to image it with maximum contrast.
3	SECTION 5.1.3 BUBBLE CHAMBER ILLUMINATION	The front 160° of the bubble to be illuminated with white light* (minimum 25 Lumens, maximum 60 Lumens) to allow observation of the bubble using the macro-view camera. The illumination system must be capable of avoiding hot spots in the field of view.
		* emission spectrum which mimics halogen light source (i.e., smooth curve with no spikes greater than 50% from aggregate, 350 nm to 780 nm).



*Table 5.1 Science Requirements Summary (continued)*

<i>Item</i>	<i>Experiment Component</i>	<i>Science Requirement</i>
4	SECTION 5.1.4 BUBBLE CHAMBER TEMPERATURE RANGE AND THERMAL CONTROL	The wall temperature of each chamber shall be controlled from 25°C to 70°C within $\pm 0.5^\circ\text{C}$ . The air temperature within 5 mm of the bubble shall be measured, with $\pm 0.5^\circ\text{C}$ accuracy.
5	SECTION 5.1.5 BUBBLE CHAMBER HUMIDITY	Each bubble chamber shall have humidity between 25% and 75%.
6	SECTION 5.1.6 BUBBLE CHAMBER PRESSURE	Each bubble chamber shall have pressure between 13.9 and 14.9 PSIA.
7	SECTION 5.1.7 LIQUID CRYSTAL SAMPLES	The liquid crystal samples shall consist of the following: <b><u>Smectic A</u></b> (1) <b><i>Polar 8CB</i></b> (2) <b><i>Non-polar MX 12160</i></b> 300 microliters $\pm 10\%$ of each sample to be contained in an enclosed dispensing unit for making LC bubbles.
		<b><u>Smectic C</u></b> (3) <b><i>Chiral MX 12805</i></b> (4) <b><i>Racemic MX 12846</i></b> 300 microliters $\pm 10\%$ of each sample to be contained in an enclosed dispensing unit for making LC bubbles.

Table 5.1 Science Requirements Summary (continued)

<i>Item</i>	<i>Experiment Component</i>	<i>Science Requirement</i>
8	SECTION 5.1.8 BUBBLE INFLATION SYSTEM	The bubble inflation system shall produce smectic bubbles with film thickness < 20 layers (each layer is 3 nm) with a tolerance of $\pm 3$ smectic layers, and a minimum of 2 layers. However, for specific tests, such as pressure quenching, the films shall be robust enough to withstand associated shearing which will require thicknesses of at least 100 layers.
9	SECTION 5.1.9 LIQUID CRYSTAL DISPENSING	The needle shall be capable of dispensing LC material via coaxial needles. The needles shall be coaxially aligned with the micro observation camera objective in order to enable observation of the surface of the bubble furthest from the needles. The bubble axis shall be coaxial with the needles within $\pm 2^\circ$ .
		The needle tip shall be heatable to a temperature between 25 and 75°C, depending on LC material.
		Tracking amount of LC solution dispensed onto the tip of bubble inflation device is required.
10	SECTION 5.1.10 BUBBLE SIZE AND DIAMETER CONTROL SYSTEM	Nominal bubble size is 15 mm with a diameter that must be controlled to within $\pm 0.1$ mm.

*Table 5.1 Science Requirements Summary (continued)*

<i>Item</i>	<i>Experiment Component</i>	<i>Science Requirement</i>
11	SECTION 5.1.11 EXPERIMENTAL AIR QUALITY	The experimental air shall be filtered such that particles larger than 10 microns do not enter the bubble chamber. The experiment package shall be cleaned and assembled such that particles larger than 10 microns are limited to 10 ppm.
12	SECTION 5.1.12 MACRO OBSERVATION AND IMAGING OF ENTIRE BUBBLE	The macro-view camera shall be of high resolution to allow near real-time viewing and recording of islands on the bubble. The camera lens-aperture must have a field of view that includes the outer diameter of the bubble, the airjet-needles, and the upper tip of the inflation needle. The depth of field and focus shall be adjusted to optimize imaging the nearer half (or front surface) of the bubble. Recommended FOV ~20 mm, DOF ~5 mm. Real-time images should be available on a color monitor for astronaut use.
		The bubble chamber shall be designed to allow observation of the front of the bubble with macro-view camera and achieve sharp contrast when viewing the bubble.
		Color camera (24 bit or higher), frame rate variable from 1 frame (still image) up to 30 fps (standard video rate).

*Table 5.1 Science Requirements Summary (continued)*

<i>Item</i>	<i>Experiment Component</i>	<i>Science Requirement</i>
13	SECTION 5.1.13 MICRO OBSERVATION OF ISLANDS	<p>The micro-view optical system shall enable near real-time visualization and recording of the details of motion of islands with diameters as small as 2 microns in a local area (micro-view FOV) of the bubble surface, enable spectroscopic reflectometry of a spot at the center of this area.</p> <p>The system shall allow images to be obtained with polarizer and analyzer. Illumination with white light (with a broad, smooth spectrum from 400 to 800 nm) polarized using a stationary polarizer. The analyzer (a polarizer with high extinction ratio of at least 200:1) should be located in the image path of the microview optical system. The analyzer should be capable of rotating in steps from 0 to 90 degrees with angular resolution of 1 degree (or better). ["0 degrees" means polarized parallel to the polarization of the illumination light.]</p> <p>Real time images should be available on a color monitor for astronaut use.</p> <p>Color camera (24 bit or higher), frame rate variable from 1 frame (still image) up to 30 fps (standard video rate).</p>
14	SECTION 5.1.14 CREATION OF DROPLETS ON BUBBLE FILM USING DROP DISPENSER	<p>Create multiple droplets (up to 500 per dispensation) between 10 and 60 microns in diameter on the bubble surface for observation and interaction. A glycerol/ water mixture will be used to create droplets. Glycerol/ water combination in drop dispenser to contain less than 5% glycerol.</p> <p>The droplets deposited onto the bubble are to be randomly distributed over an area that can be imaged by the macro-view camera.</p> <p>The rate of production of droplets by the IDD will be variable from 1 to 500 droplets per second, controllable in increments of 1 up to a deposition rate of 100 drops per second, and in increments of 50 over the remainder of the range.</p> <p>The time over which droplets are produced will be variable from 1 to 100 seconds in steps of 1 second.</p> <p>The IDD will also be capable of generating single droplets on demand.</p>

*Table 5.1 Science Requirements Summary (continued)*

<i>Item</i>	<i>Experiment Component</i>	<i>Science Requirement</i>
15	SECTION 5.1.15 CREATION OF ISLANDS AND PORES ON BUBBLE FILM USING AIR JETS	Island emulsions shall be created using air flow (utilizing filtered station air) of 10 to 150 sccm $\pm 1$ sccm issuing from 4 air jet nozzles located tangentially 500 microns above the bubble surface and centered on the field of view of the micro observation camera.  Duration: typically 1–2 minutes until islands form, maximum 5 minutes.
		Air jet shall provide very low velocity laminar flow, with Reynolds number less than 1500.
		Air jet nozzle separation shall be $\sim 1$ mm (should not be visible in the micro observation camera field of view at higher magnifications)
	{RAPID PARTIAL DEFLATION OF BUBBLE}	Reducing the bubble diameter abruptly (by around 2–10%) is an alternate way of creating islands on the bubble.
16	SECTION 5.1.16 EXTERNAL ELECTRIC FIELD INTERACTION WITH ISLANDS/PORES ON BUBBLE FILM	An electric field device capable of producing an E field of 100 kV / m from dc to 10 kHz.  The frequency shall be adjustable in 10 Hz steps from 0 to 1 kHz, and in 100 Hz steps over the remainder of the frequency range.  Recommended applied voltage: 100 $\pm 1$ V; needle separation: 1 $\pm 0.1$ mm.
17	SECTION 5.1.17 DYNAMIC INFLATION AND DEFLATION OF THE LC BUBBLE	Partial deflation of the bubble by abrupt contraction, the volume changing by up to 30% in less than 1 second.  Modulate bubble size smoothly by alternately expanding and contracting the bubble, the diameter changing by up to 5% at a rate variable between 0 and 30 Hz. Duration: 2–5 minutes  Need to be able to interrupt this process at any point in the expansion/contraction cycle.

Table 5.1 Science Requirements Summary (continued)

<i>Item</i>	<i>Experiment Component</i>	<i>Science Requirement</i>
18	SECTION 5.1.18 TEMPERATURE GRADIENT FOR MARANGONI EFFECT	Localized heating of bubble surface such that there exists a temperature gradient of $30\pm 1^{\circ}\text{C per mm}$ between the airjet needles.  Heat one of the air jet needles and cool the other to establish a temperature gradient of $30\pm 1^{\circ}\text{C per mm}$ for up to 2 minutes
19	SECTION 5.1.19 ISLAND OBSERVATION & DEPOLARIZED REFLECTED LIGHT MICROSCOPY	Measure island thickness to within $\pm 3$ smectic layers.  Observe, with and without polarizers, islands with the following characteristics: <ul style="list-style-type: none"> <li>- diameter from 2 to 100 microns</li> <li>- velocity <math>&lt; 30</math> microns/s</li> <li>- thickness can vary from 20 to 70 layers [3 nm per layer].</li> </ul>
20	SECTION 5.1.20 MICROGRAVITY ACCELERATION MEASUREMENT	Microgravity acceleration to be measured utilizing SAMS TSH-ES or equivalent.



### 5.1.1 – OASIS HARDWARE UNITS

The OASIS hardware will be designed and developed for the Microgravity Science Glovebox (MSG) or the Light Microscopy Module (LMM) and dedicated solely to the purpose of performing the proposed series of OASIS experiments.

There will be four separately enclosed OASIS hardware units (“shoeboxes”), in order to prevent cross contamination of the liquid crystal (LC) samples.

### 5.1.2 – BUBBLE CHAMBERS

Each Bubble Chamber (BC) is equipped to make bubbles of a particular liquid crystal sample, position the bubble for observation using the individual macro-view video camera, perturb the bubble in a variety of ways, and enable spectrometry and island observation with micro-view video imaging system.

These functions are controlled by the OASIS computer. The BCs are sketched in **Figure 2.27** and are described and equipped as follows:

- Temperature controlled (25°C to 70°C,  $\pm 0.5^\circ\text{C}$ )
- Automated, quasistatic liquid crystal loading and bubble inflation. Motor drives or other suitable mechanism for LC injection and inflation are required. Each sample is preloaded in a  $\sim 300\ \mu\text{l} \pm 10\%$  reservoir. Needle tip controllably heated up to 75°C depending on sample (see Section 5.1.8 below).
- Macro-view digital video with optical illumination over bubble hemisphere in reflection. A matte black background is necessary to achieve sufficient optical contrast. Used for imaging as well as for measuring and controlling bubble diameter.
- Flow generation – low pressure air source required.
- Field application electrodes.
- Temperature gradient induction.
- Inkjet or equivalent system for producing glycerol/water droplets and depositing them on the bubble.
- Equipment to position the bubble and measure its diameter, and photodiode to measure film thickness.
- While in orbit, station air shall be circulated into the chamber so that the air in the chamber is the same as that in the MSG and on station.

### 5.1.3 – BUBBLE CHAMBER ILLUMINATION

The front 160° of the bubble to be illuminated with white light\* in order to observe the air-jet needles, and the top part of bubble inflation system, using the macro-view camera. The illumination system must be capable of avoiding hot spots when observed by the macro-view camera.

The inner walls of the chamber must be highly diffusive and reflective (better than 95% R) in order to observe the entire bubble with the front half evenly illuminated with white light using the macro-view camera.

\* emission spectrum which mimics halogen light source (i.e., smooth curve with no spikes greater than 50% from aggregate, 350 nm to 780 nm).

#### 5.1.4 – BUBBLE CHAMBER TEMPERATURE RANGE AND THERMAL CONTROL

- The temperature of each chamber shall be controlled from 25°C to 70°C to within  $\pm 0.5^\circ\text{C}$ .
- The air gap temperature, within 5 mm of the bubble surface, in the bubble chamber, must be measured with  $\pm 0.5^\circ\text{C}$  accuracy.
- Set by a thermistor or RTD sensor and a PID feedback controller. Range, accuracy and desired response rate are respectively: 25°C to 70°C,  $\pm 0.5^\circ\text{C}$ , 1°C / min.
- Temperature monitored by a second thermistor or RTD sensor in the BC wall.

#### 5.1.5 – BUBBLE CHAMBER HUMIDITY

Each bubble chamber shall have humidity between 25% and 75%, although the lower the humidity the better.

#### 5.1.6 – BUBBLE CHAMBER PRESSURE

Each bubble chamber shall have pressure between 13.9 and 14.9 PSIA.

#### 5.1.7 – LIQUID CRYSTAL SAMPLES

Sample materials have been chosen to enable study of a range of island behavior and interactions, as follows:

- 8CB** [I – (40.5°C) – N – (33.5°C) – SmA – (21.5°C) – Xtal] – A widely-studied, chemically stable room temperature smectic A material that has a large molecular dipole moment parallel to the molecular long axis. It is known to adopt interfacial polar ordering, with the dipoles normal to the interface. Islands may interact electrostatically via dipolar interactions. The N to SmA transition in 8CB is second order, heralded by a general weakening of the smectic layer ordering as the transition is approached by increasing temperature in the SmA phase. Weaker layer ordering should result in faster molecular transport from layer to layer and therefore accelerated dynamic behavior of islands. 8CB is available from EM Industries.
- MX12160** [I – (51°C) – SmA – (-3.2°C) – Xtal] – A chemically stable, room-temperature SmA mixture of symmetric, weakly-polar molecules, minimizing dipolar interactions. MX12160 is available from Micron Technology (formerly Displaytech).
- MX12805** [I – (84.7°C) – N – (81.4°C) – SmA – (66.1°C) – SmC – (-22°C) – Xtal] – A chemically stable, room-temperature chiral SmC mixture with nematic and SmA phases at higher temperature, available as either the pure enantiomer (MX12805) or as a racemic mixture (MX12846). In the SmC phase the molecular long axis is tilted with respect to the film plane and the islands interact via the resulting c-director orientation field. This interaction is weakest for racemic films coming only from c-director elasticity. In chiral films the elastic forces are augmented by electrostatic interactions due to the spatial variation of the chiral SmC ferroelectric polarization. All of these interactions should exhibit a pronounced temperature dependence as the SmC–SmA transition is approached and the SmC c-director elastic constants and polarization approach zero. MX12805 and MX12846 are available from Micron Technology (formerly Displaytech).

300 microliters  $\pm 10\%$  of each sample will be contained in an enclosed dispensing unit for making LC bubbles.

Micron Technology will provide samples of the four liquid crystals identified above to the PI. The PI will provide samples of these materials to the OASIS project team for flight as some of them are proprietary in nature and cannot be acquired by NASA.

### 5.1.8 – BUBBLE INFLATION SYSTEM

The bubble is inflated using a pair of coaxial needles. First the needle tips are locally heated to lower the viscosity, then a small amount of liquid crystal material from the outer needle is expelled so that it blocks the inner needle opening. A low flow of air is introduced into inner needle to push out a thin, closed membrane of LC from the material across the needle opening, and to expand this to form a bubble, which remains tethered to tip of the inflation needle. The needle heater is turned off as soon as the initial bubble has formed and is then allowed to equilibrate with the chamber.

The bubble size is measured using the image from the macro-view camera image and/or a position-sensitive optical sensor during inflation and the desired bubble size is subsequently maintained by a feedback control loop. A peristaltic pump can be used to pump air in and out of the bubble. Heating the tip of the needle to between 20°C and 75°C may be helpful to lower the viscosity of the LC solution in order to blow the bubble. The needle tip temperature should be kept several degrees below the highest temperature at which the liquid crystal material is still smectic. Safe maximum values are 30°C for 8CB, 50°C for MX12160, and 75°C for both MX12805 and MX12846.

The experimental goal is to generate thin bubbles (film thickness <20 smectic layers with a minimum of 2 layers, with a tolerance of  $\pm 3$  smectic layers) that are 15 mm in diameter and then observe thicker islands/droplets floating on these background films. However, for specific tests, such as pressure quenching, film thickness shall be robust enough to withstand associated shearing which will require thicknesses of at least 100 layers.

### 5.1.9 – LIQUID CRYSTAL DISPENSING

The LC is dispensed via a coaxial needle. The dispensing amount varies but requires nominally about 0.25  $\mu\text{l}$  per bubble.

Tracking amount of LC solution dispensed onto the tip of bubble inflation device can be performed by recording the number of times LC is pumped from the reservoir.

### 5.1.10 – BUBBLE SIZE AND DIAMETER CONTROL SYSTEM

Nominal bubble diameter is 15 mm.

The bubble size must be determined and actively controlled to within  $\pm 0.1$  mm.

An optical or video tracking system with feedback loop is desired to control the bubble diameter. Over an extended period of time (4 days, for example) the bubble may shrink due to the diffusion of air out of the bubble, and one needs to “pump up” (reinflate) the bubble at certain intervals. The bubble reinflation feedback system will maintain the bubble at constant diameter.

### 5.1.11 – EXPERIMENTAL AIR QUALITY

The experimental air shall be filtered such that particles larger than 10 microns do not enter the bubble chamber. The experiment package shall be cleaned and assembled such that particles larger than 10 microns are limited to 10 ppm.

### 5.1.12 – MACRO OBSERVATION OF ENTIRE BUBBLE

Illumination of approximately one third of the bubble and observation in reflection (see **Figure 5.1** and detailed discussion in **Section 5.2** below).

The macro-view camera shall be of high resolution to allow near real-time viewing and recording of islands and droplets on the bubble. The camera lens-aperture must have a field of view that includes the outer diameter of the bubble, the airjet-needles, and the upper tip of the inflation needle. The depth of field and focus shall be adjusted to optimize imaging the nearer half of the bubble while allowing the outer diameter and needle tip to be observed as well. Recommended FOV ~20 mm, depth of field ~5 mm.

Real-time images should be available on a color monitor for astronaut use.

The bubble chamber must have a black or equivalent matte background to achieve sharp contrast when viewing the bubble.

Color camera (24 bit or higher), frame rate variable from 1 frame (still image) up to 30 fps (standard video rate), data collection intervals from once per hour to continuous for periods from five seconds to ten minutes.

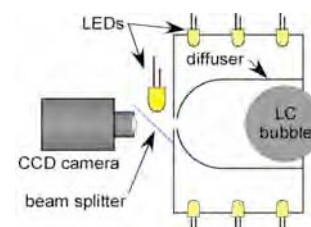


**Figure 5.1** Macro camera setup for overall bubble illumination and video observation.

### 5.1.13 – MICRO OBSERVATION OF ISLANDS

The micro-view optical system shall enable real-time visualization and recording of the details of motion of islands with diameters as small as 2 microns in a local area of the bubble surface, enable spectroscopic reflectometry of a spot at the center of this area.

Recommend Microscope objective: 20X

Field of view: 500x500 square microns

Resolution: 2 microns

The system shall allow images to be obtained with polarizer and analyzer. Illumination with white light (with a broad, smooth spectrum from 400 to 800 nm) polarized using a stationary polarizer. The analyzer (a polarizer with high extinction ratio of at least 200:1) should be located in the image path of the microview optical system. The analyzer should be capable of rotating in steps from 0 to 90 degrees with angular resolution of 1 degree (or better). ["0 degrees" means polarized parallel to the polarization of the illumination light.]

Real time images should be available on a color monitor for astronaut use.

Color camera (24 bit or higher), frame rate variable from 1 frame (still image) up to 30 fps (standard video rate), data collection intervals from once per hour to continuous for periods from five seconds to ten minutes.

### 5.1.14 – CREATION OF DROPLETS ON BUBBLE FILM USING INKJET DROP DISPENSER

Create multiple droplets (up to 500 per dispensation) between 10 and 60 microns in diameter on the bubble surface for observation and interaction. A glycerol/water mixture will be used to create droplets using inkjet printing (the Inkjet Drop Dispenser, or IDD) or an equivalent deposition method.

Glycerol/water combination in inkjet device to contain less than 5% glycerol.

A few tens of picoliters of glycerol/water solution are typically required to create a single droplet of less than 60 microns diameter.

The rate of droplet production by the IDD will be variable from 1 to 500 droplets per second, controllable in increments of 1 up to 100 drops per second, and in increments of 50 over the remainder of the range. The time over which droplets are produced will be variable from 1 to 100 seconds. The IDD will also be capable of generating single droplets on demand.

The droplets deposited onto the bubble will be dispersed over an area that can be imaged by the macro-view camera. The diameter of this area will be in the approximate range of 1 to 5 mm, depending on how many drops are on the film and how big the individual drops are.

It is desirable that the droplets can be deposited on the bubble in a two-dimensionally ordered arrangement, for example approximating a square or triangular lattice, or in parallel "strings" of droplets on the film.

#### 5.1.15 – CREATION OF ISLANDS AND PORES ON BUBBLE FILM

- **Technique 1** – Two pairs of opposing, sub-millimeter diameter (detailed dimensions given above) hypodermic needles connected to pressurized gas are located within 100 microns of being tangent to the smectic sphere. A pair of these air jets induce pure extensional, in-plane flow at a point on the bubble, as shown in **Figure 5.2**, with a shear rate of  $\sim 100 \text{ s}^{-1}$ , which generates a two-dimensional array of islands as shown in **Figure 2.1a**. Estimated flow rate is (mass flow of 10 to 150 sccm, velocity  $\sim 1.5 \text{ mm/s}$ ).

- **Technique 2** – Reduce the pressure inside the bubble abruptly, which reduces the diameter of the bubble. This method can be achieved either by retracting the air needle plunger rapidly or by opening the check valve (solenoid) and quickly closing it again before the bubble collapses.

- **Technique 3** – Locally heat the bubble by heating one or both needles used to generate thermocapillary flow.

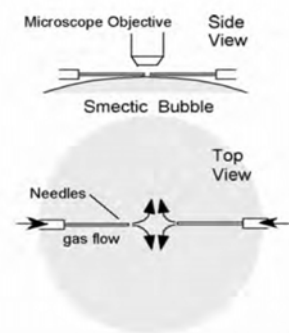


**Figure 5.2** Air jets for inducing extensional flow of the bubble surface.

#### 5.1.16 – EXTERNAL ELECTRIC FIELD INTERACTION WITH ISLANDS/PORES ON BUBBLE FILM

Fields can be applied using the airjet needles (25 gauge [500  $\mu\text{m}$  od, 260  $\mu\text{m}$  id]) as electrodes: tip shape (blunt) and electrode separation (1 mm).

An electric field device capable of producing an E field of 100 kV/m from dc to 10 kHz. Recommended sinusoidal applied voltage:  $100 \pm 1 \text{ V}$ ; needle separation:  $1 \pm 0.1 \text{ mm}$ .

A high voltage amplifier-converter and a function generator, ac sinusoidal voltage output.

#### 5.1.17 – DYNAMIC INFLATION AND DEFLATION OF THE LC BUBBLE.

Rapid inflation and deflation of the bubble can be achieved using a piezo element attached to the plunger or a deflation valve.

Partial deflation of the bubble by abrupt contraction, the volume changing by up to 30% in less than 1 second.

Modulate bubble size smoothly by alternately expanding and contracting the bubble, the diameter changing by up to 5% by volume at a rate variable between 0 and 30 Hz.

The user should be able to interrupt this process at any arbitrary time in the expansion/contraction cycle.

Duration: 2–5 minutes

#### 5.1.18 – TEMPERATURE GRADIENT FOR MARANGONI EFFECT

Localized heating of bubble surface in the field of view of the micro-view imaging objective, with a temperature gradient of up to  $30 \pm 1^\circ\text{C}/\text{mm}$ . The gradient in the air will need to be higher than this, e.g.  $50^\circ\text{C}/\text{mm}$ . Thermoelectric (Peltier) devices could be used to cool one needle while heating the other.

The heated needle can be wrapped with insulated 30 gauge nichrome wire and a  $350\ \mu\text{m}$  thermistor can be attached to measure and control the temperature. The electrodes/heater/air needles are less than 1 mm above the bubble surface.

#### 5.1.19 – ISLAND OBSERVATION & DEPOLARIZED REFLECTIVE LIGHT MICROSCOPY

Bubble images obtained by video microscopy will be the principal data to be collected and requires capabilities discussion in detail in **Section 5.2** below. Depolarized reflected light microscopy (DRLM) will be used to visualize textures in SmC films showing island interactions and thermocapillary flow.

Need to be able to measure island thickness to within  $\pm 3$  smectic layers.

Observe, with or without polarizers, islands with the following characteristics:

- diameter from 2 to 100 microns
- velocity  $< 30\ \mu\text{m}/\text{s}$
- thickness can vary from 20 to 70 layers [3 nm per layer]



### •Technique 1 – Optical Spectroscopy

The thickness of thick films and islands can be determined from the optical spectrum of reflected white light, the reflected intensity and interference color depending on the thickness ( $h$ ) and refractive index ( $n$ ) of the film (**Figure 5.3**). Spectra will be measured using the micro-view optical observation system at high magnification, which will enable the analysis of single islands. Measurements will be performed using a visible light spectrometer. The *Ocean Optics QE6500* meets all requirements for this measurement.

### •Technique 2 – Optical Reflectivity

A common procedure for determining smectic film thickness is based on measuring optical reflectivity. Since the reflectivity  $R$  of the film varies as  $R \propto h^2$  with thickness  $h$  for thin films (**Figure 1.2**), we can infer the number of layers by measuring the reflectivity using a CCD camera. The integrated reflectivities in the RGB channels of a color camera, averaged over a 200  $\mu\text{m}$  diameter spot on a flat film, are shown in **Figure 5.4**. In principle, any one of these curves can be used to infer the film thickness.

#### 5.1.20 – MICROGRAVITY ACCELERATION MEASUREMENT

In order to maximize the probability of the success of these experiments, the dc component of gravity should be as small possible and no larger than  $10^{-3}g$ , averaged over an hour. Since vibrations of the environment cannot be controlled, measurement of vibrations during the mission will be used to determine if samples were disturbed during critical periods.

Microgravity acceleration will be measured utilizing SAMS TSH-ES or equivalent.

#### 5.2 – ILLUMINATION AND IMAGING OF BUBBLES AND ISLANDS (VIDEO MICROSCOPY)

Bubble images obtained by video microscopy will be the principal data to be collected and will require the capabilities detailed below.

##### 5.2.1 – MACRO-VIEW IMAGING OF THE WHOLE BUBBLE

**Requirement** – The requirement is for an optical system that enables real-time visualization and recording of the distribution of the position, size and color of islands larger than 10  $\mu\text{m}$  in diameter over a 1  $\text{cm}^2$  area.

Islands will be observed on a spherical segment of the bubble surface comprising about 35% of the bubble area. The field of view must however include the whole 15 mm diameter bubble with enough extra area to enable the outline of the bubble and the tethering needle and the airflow needles to be visible. Frames are to be recordable at

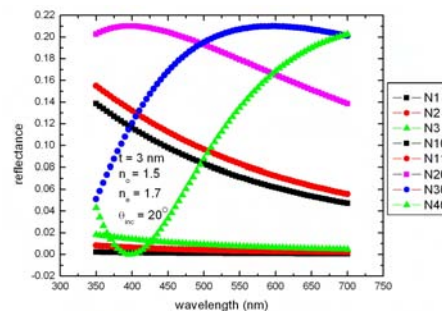


**Figure 5.3** Model optical reflection spectra of smectic A film as a function of film thickness, indicated in the legend by the layer number  $N$ .

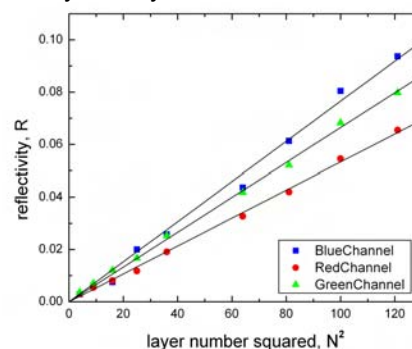


**Figure 5.4** Optical reflectivity of a SmA film as detected by the RGB channels of a color CCD camera. The signal varies quadratically with layer number  $N$  and can be used to determine film thickness.

video rate (30 frames/s), at any selected lower periodic frame rate, or aperiodically at any selected time (e.g., spaced logarithmically in time).

*Comments* – Film thickness will be measured in reflection so the imaging system must use reflected light. The intensity and color of the light reflected from the film determines its thickness, so both intensity and color must be recorded. The maximum film reflectivity is 16% (constructive interference of the reflections from the two 4% reflectivity surfaces). The minimum reflectivity, from a  $N = 2$  layer film, the thinnest likely to be encountered, is  $\sim 0.16\%$ , making the dynamic range of light reflected from the film a factor of 100. Thus the minimum requirement for the number of levels for each color is 256 (8 bits).

The illumination requirement is to provide diffuse light so there is a reflected light path for all rays traversing from the front of the bubble to the camera aperture, except for those where the camera aperture itself prevents illumination of the bubble. This requires a luminous, spherocylindrical frosted cavity surrounding the bubble and a matte black screen behind the bubble. The spherocylindrical shape enables the imaging camera to be suitably far from the bubble without making the frosted chamber unduly large. Since the area selected for imaging is being viewed in reflected light, the bubble surface must be illuminated such that the intensity of light reflected from points in this area is sufficiently uniform. Illumination should be with white light, similar to that obtained from halogen bulbs.

The smallest resolvable features on the bubble surface are the island edges, which are a few nm wide, representing the smallest possible island diameter. Therefore, if the optical resolution is greater than a few nm, the size of the smallest observable islands will be determined by the optical resolution. The requirement is thus to provide as small a resolution as is practicable. The imaging resolution will depend on the imaging optics and the pixelation of the imager. Design of the optical system must optimize competing requirements for resolution, depth-of-field, and light gathering.

The optical resolution obtained depends on the numerical aperture and depth of field of the imaging optics. The height of a spherical segment comprising 35% of the area of a 15 mm diameter bubble is 5 mm. The depth of field (DOF) should thus be  $\text{DOF} \sim 5$  mm, so that if the plane of focus intersects the half of the bubble closest to the camera ( $\sim 2.5$  mm behind the point of the bubble closest to the camera), then most of the front half of the bubble will be in focus and the back not in focus, which is a requirement.

*Example* – This can be achieved using, for example, an imaging lens with focal length  $f = 25$  mm placed  $\sim 75$  mm from the front of the bubble, which would image the bubble 2:1 onto a 1 cm  $\times$  1 cm imaging chip placed 37.5 mm behind the lens. With a 10 megapixel imager, the pixel size ( $p$ ) of a 1 cm  $\times$  1 cm imager is  $p \sim 3.5 \mu\text{m}$ .

DOF is given by  $\text{DOF} = 2(f\#)c(M+1)/M^2$ , where  $f\# = 75 \text{ mm}/D$ ,  $c$  = circle of confusion,  $M$  = magnification, and  $D$  = diameter of the lens aperture.

If we take  $c = p$  and  $M = 0.5$ , then the depth of field will be  $\text{DOF} = 12 \times (75 \text{ mm}/D) \times 3.5 \mu\text{m} = 3.1 \text{ mm}/(D \text{ mm})$ .

However, for this geometry the imaging numerical aperture (NA) is given in terms of  $D$  as  $\text{NA} = D/2 \times (75 \text{ mm})$ , in which case the diffractive optical resolution ( $R$ ) is given by  $R = 1/2 \text{ NA} = (75 \text{ mm})/D$ , which for  $D = 1$  (2) mm gives  $R \sim 35$  (18)  $\mu\text{m}$ , somewhat larger than desirable. Since decreasing  $R$  will increase both DOF and  $R$ , there is a trade-off to be established in the choice of  $D$ .  $D$  also affects the optical throughput to the chip:

in the above example, light is collected through a 1 mm hole. Increasing  $D$  gives more light and smaller diffractive resolution but decreases the DOF.

#### 5.2.2 – MICRO-VIEW VIDEO/SPECTROMETRY

**Requirement** – The requirement is for an optical system that enables real-time visualization and recording of the details of island motion in a local area of the bubble surface and enables spectroscopic reflectometry of a spot at the center of this area.

**Comments** – This system will be mounted onto the hardware unit (“shoebox”) and consist of three interchangeable  $\infty$ -tube-length objectives, and an optical path including a beam splitter and white light source enabling illumination of an area  $\pi R^2$  of the bubble through the objective, a beam splitter, imaging lens, aperture, and spectrometer for measuring the intensity and spectrum of the light reflected from a spot of area  $\pi S^2$  on the bubble, a beam splitter and collimated light source for illuminating a spot of area  $\pi L^2$  on the bubble, and an imaging (tube) lens focusing light onto an imaging chip, and a shutter in front of the imaging chip. The chip should be 10 Mpixel and about 1 cm x 1 cm in size. The objective will be 20X (nominal focal length = 8 mm). With a tube lens of  $F = 80$  mm, the 20X objective gives 20 times magnification from bubble to imager, i.e., images a 0.5mm x 0.5mm area of the bubble onto the imager.

#### 5.2.3 – REAL-TIME OBSERVATION

It is essential that the real time images from both cameras be available on a color monitor for the astronaut’s use.

#### 5.3 – ASTRONAUT INVOLVEMENT AND EXPERIMENT ACTIVATION

After initial setup minimal astronaut involvement is envisioned, although the experiment apparatus should have a manual control interface to allow intervention in near real time should any problems arise.

#### 5.4 – DATA REQUIREMENTS

On-board data storage should log complete experimental records including video data and experimental conditions:

- *micro-view and macro-view images*
- *BC temperature*
- *voltages*
- *color spectra*
- *spectrometer data*

#### 5.5 – TELESCIENCE

Downlink of near-real time video of the experiment is being requested. It is anticipated that the astronaut will set up the experiment and some ground commanding will be done on portions of the experiment while other portions will be automated. Using downlink data from the experiment or the facility, we will be able to assess the health status of various systems, assess the environment in the facility, and monitor the experiment hardware.

#### 5.6 – ACCELERATION: MAGNITUDE, DIRECTION, AND FREQUENCY

In order to maximize the probability of the success of these experiments the dc component of gravity should be as small possible and no larger than  $10^{-3}g$ , averaged over an hour. Since vibrations of the environment cannot be controlled, measurement

of vibrations during the mission will be used to determine if samples were disturbed during critical periods.

## 6 – SUMMARY OF EXPERIMENTS

### 6.1 – EXPERIMENT 1: COARSENING DYNAMICS

#### *Observation of Coarsening Dynamics of 2D Island Emulsions for Extended Period of Time (Ostwald Ripening and/or Diffusion-Coalescence Dynamics)*

This experiment will be carried for both SmA and SmC materials, at several temperatures for each material. **If time permits, this experiment can also be carried out for varying background film thickness.** For a given material, temperature, and film thickness, the experiment will be repeated several times to collect adequate statistics on island size (diameter) and thickness distributions as a function of time during the coarsening process. Each experiment (for a given material, temperature, and film thickness) is initiated by blowing air over the film for a short time (or depositing drops of glycerol/water with the IDD) to create a dense island emulsion. Ideally, the same bubble will be used for a complete series of experiments at various temperatures, maintaining a constant bubble diameter and a constant volume of material in the meniscus.

#### *Notes/challenges:*

- Observation of islands over a wide range of diameters (1  $\mu\text{m}$  to 1 mm) requires high-resolution micro and macro video.
- Coarsening dynamics is initially fast, slowing dramatically in later stages, so a variable data rate is desirable.
- We anticipate that the smallest islands (< 20  $\mu\text{m}$  diameter) will only be present in the early stages of coarsening dynamics, so high magnification may only be required for the first few minutes of each experiment.
- This suggests the following protocol for each material, temperature and film thickness:
  - A large number of short-duration experiments on early-stage coarsening dynamics, using high-resolution video.
  - A smaller number of long-duration experiments on middle- to late-stage coarsening dynamics, using medium-resolution video.
- Macro video will be required for both types of experiment, as will spectrometer output.
- Video and spectrometer data should be time-stamped and synchronized.
- The spectrometer will provide an accurate measurement of the thickness of the background film and of any islands that drift through the center of the field of view of the high- or medium-resolution microscope; island thickness will also be estimated from the reflection color observed in video images (using spectrometer output for calibration).

### 6.2 – EXPERIMENT 2: 2D THERMO-CAPILLARY EFFECTS

#### *2D Thermo-Capillary Effects (Temperature Gradient-Induced Flow and its Effect on Island Organization and Dynamics and on SmC Textures)*

In this experiment, temperature gradients in the plane of the film are produced by establishing a temperature difference between two of the needles used to blow air across the film. Based on literature values, it is anticipated that a 10°C temperature variation can produce a 5–10% change in surface tension, so we will aim for a temperature gradient of at least 10°C over the field of view of the micro-view camera (~30°C/mm). A temperature difference between the two needles will be maintained by

heating/cooling each needle with thermoelectric (Peltier) devices, and the temperature between the needle tips will be monitored with thermistors (RTDs). The needle–needle and needle–film distances are both on the order of 1 mm, so a temperature differential of 30°C between the two needles should be sufficient to produce the required in-plane gradients.

Two types of experiments will be carried out:

1. Thermocapillary flow will be visualized by tracking islands or other inclusions in the film (e.g., droplets); a sufficient number of islands/inclusions are created prior to establishing a temperature gradient (e.g., by blowing across the film or using ink-jet printing). This experiment can be carried out on both SmA and SmC bubbles.
2. Thermocapillary flow will be visualized through observation of textural changes in SmC films using depolarized reflected light microscopy (DRLM). The rotation of the c-director field of the liquid crystal couples to 2D flow velocity gradients.

Each experiment will consist of continuous, micro-view video observation of the film for several minutes. The macro-view camera will be used to monitor large-scale flow on the bubble, and the spectrometer will be used to measure background film thickness.

We will also look for thermo-migration of islands to hot or cold spots on the film, driven by thickness- and temperature-dependent surface tension. For these experiments, we will heat or cool the needles as needed to create a temperature gradient.

In all of the experiments, output from the micro- and macro-view cameras and from the spectrometer should be time-stamped.

### 6.3 – EXPERIMENT 3: 2D HYDRODYNAMICS

#### ***2D Hydrodynamics of Islands and Droplets (Brownian Motion and Hydrodynamic Interactions of Islands and Droplets)***

In this experiment we will apply a voltage between two of the air-jet needles to create an in-plane electric field. We will observe island interactions and migration (e.g., dielectrophoretic effects) in SmA and SmC bubbles, and field-induced textural changes in SmC bubbles. Each experiment will require several minutes of continuous micro-view video observation of films.

We will also observe the Brownian motion and hydrodynamic interactions of island emulsions after being subjected to either extensional or shear flow from the airjet needles.

Finally, we will observe the Brownian motion and hydrodynamic interactions of islands and droplets in the absence of a perturbing field with the micro-view camera (e.g., to look for a dependence of inclusion mobility on bubble curvature in bubbles of varying thickness).

Each measurement will require several minutes of continuous micro-view video observation.



#### 6.4 – EXPERIMENT 4: NUCLEATION OF ISLANDS AND PORES

##### ***Nucleation of Islands and Pores in Bubbles by Varying Internal Pressure***

In this experiment, we will apply sudden pressure quenches or periodic pressure variations to the bubble to generate islands or pores. The internal pressure of the bubble can be varied using the same pump that is used to inflate the bubble. Each experiment will consist of several minutes of continuous video observation of the bubble with the micro- or macro-view cameras.

## 7 - EXPERIMENT PROTOCOL & TEST MATRICES

This section contains the experiment protocol and test matrix for OASIS. First we outline the initial setup for OASIS, which is the same for all experiments. Then we list the steps that will be followed for each of the four major experiments and present a test matrix for each.

There are four different OASIS hardware units (the “shoeboxes”), each containing a different liquid crystal (LC) sample to be prepared and observed in a small bubble chamber. Four major experiments will be conducted with each unit. Prior to the start of each set of experiments, we require the formation of an LC bubble and generation of islands or droplets on the bubble, using respectively the air jet system or the inkjet drop dispenser. In addition to the variation of experiment parameters detailed in the procedures below, it would be highly desirable to repeat each experiment on bubbles of different film thickness.

### 7.1 - INITIAL SETUP

The initial set up requires astronaut involvement until the successful formation of a LC bubble of specified diameter (15 mm) and thickness of less than 10 layers is achieved.

#### 7.1.1 – POSITIONING OF THE BUBBLE CHAMBER

One of the four hardware units will be positioned in the observation system deck so that the inside of the bubble chambers is aligned with the microscope. The observation system comprises the DRLM (Depolarized Reflected Light Microscope) fitted with a high-resolution video camera, and another camera for a macro view of the bubbles and surrounding equipment, with one of the latter attached and dedicated to each bubble chamber. The video cameras are used in all four experiments.

#### 7.1.2 – BUBBLE FORMATION

##### **Required Physical Controls:**

temperature, liquid dispensing rate, volume of LC sample

**Observation:** macro camera

##### **Bubble formation sequence:**

- (1) Illuminate the bubble chamber.
- (2) Heat the bubble jet needle to specified temperature.
- (3) Extrude LC sample at the tip of the needle, known amount/ number of pulses or shots from the stepper motor syringe.
- (4) Inject air using the peristaltic pump.
- (5) Turn off the needle heater.
- (6) Continuously observe the formation and growth of the bubble until it reaches the specified diameter.
- (7) Measure bubble thickness.

### 7.1.3 – GENERATION OF ISLANDS/DROPLETS

**Required Physical Controls:** (for air jet) air flow sccm, time; (for droplets) deposition rate, position, time

**Observation:** micro and macro cameras

**Island generation sequence (air jets):**

- (1) Tangential air flow from opposing air needle jets.
- (2) Macro observation of creation of island emulsions.
- (3) Micro observation of islands.

**Droplet generation sequence (IDD):**

- (1) Droplets generated by inkjet device.
- (2) Droplets positioned on bubble surface.
- (3) Macro observation of creation of droplet emulsions.
- (4) Micro observation of droplets.

**Remark:** Experiments using the droplet dispenser will be carried out only after all experiments on LC islands have been completed in order to avoid contamination of the liquid crystal samples.

## 7.1.4 – TEST MATRIX FOR INITIAL SETUP

*Table 7.1 Test Matrix for Initial Setup: island generation sequence*

<i>Requirement and Execution Sequence</i>	<i>Method</i>	<i>Physical Controls and Parameter Values</i>	<i>Time Period</i>
Bubble formation	heating the needle extruding the LC air injection	T control of needle T control of chamber	turn off needle T control as soon as bubble forms and allow to equilibrate to chamber
Bubble film thickness measurement	Micro observation of bubble	video camera or spectrometer	for initial bubble, then periodically during experiments
Bubble diameter	macro observation of bubble	linear CCD array or video camera	continuous feedback to maintain the bubble diameter
Creation of islands	tangential air flow from opposing air needle jets or pressure quenching	air flow rate bubble pressure	for 1–2 mins.
Observation /video recording of bubble formation	micro or macro or both	video camera	
Observation and video recording of island generation	“	“	

*Table 7.2 Test Matrix for Initial Setup: droplet generation sequence*

<i>Requirement and Execution Sequence</i>	<i>Method</i>	<i>Physical Controls and Parameter Values</i>	<i>Time Period</i>
Minimize Sample Contamination	Experiments using the IDD will be carried out only after all experiments on LC islands have been completed in order to avoid contamination of the liquid crystal samples.		
Bubble formation	heating the needle extruding the LC air injection	T control of needle T control of chamber	turn off needle T control as soon as bubble forms and allow to equilibrate to chamber
Bubble film thickness measurement	Micro observation of bubble	video camera or spectrometer	for initial bubble, then periodically during experiments
Bubble diameter	macro observation of bubble	linear CCD array or video camera	continuous feedback to maintain the bubble diameter
Creation of droplets	generation of droplets in a predefined pattern using the IDD	- voltage for single droplet ejection - selection of desired patterns	few seconds
Observation / video recording of bubble formation	micro or macro or both	video camera	
Observation and video recording of island generation	“	“	

*Remark:* Experiments using the droplet dispenser will be carried out only after all experiments on LC islands have been completed in order to avoid contamination of the liquid crystal samples.

## 7.2 – Experiments

### 7.2.1 – EXPERIMENT 1: COARSENING DYNAMICS

- *Observation of 2D Island Emulsions (Ostwald Ripening) for Extended Period of Time*
- *Island and Droplet Coalescence*
- *Observation of Island/Droplet Emulsion*
- *Brownian Motion of Islands/Droplets*

In this experiment, we will study dense collection of islands created using the air jets or droplets created with the drop dispenser.

- (1) Illuminate chamber with white light.
- (2) Temperature control at desired temperature.
- (3) Islands: Create dense islands by blowing air over the film using air jets (5 sscm) for 1–2 minutes.  
Droplets: Create a pattern of droplets on the bubble surface by droplet ejection from the IDD for a few seconds.
- (4) Monitor temperature of bubble chamber every 30 s.
- (5) Monitor macro image of bubble (observe 1 hour, record every 2 minutes).
- (6) Measure bubble thickness (sample every minute).
- (7) Islands: Measure island thickness (monitor continuously but take data every 5 s for 15 min and then sample once per minute until the end of the experiment).  
Droplets: Measure droplet diameter by micro observation.  
Droplet diameter decreases by (water) evaporation from water/glycerol solution. Final droplet diameter is reached after 1 minute.
- (8) Continuous high-resolution, micro observation, acquire data continuously for 15 minutes, with 20X microscope objective
- (9) Raise temperature incrementally and repeat steps (2) to (8) at each temperature; use 1°C increments up to  $T=30^{\circ}\text{C}$  for SmA materials, 5°C increments up to  $T=60^{\circ}\text{C}$  for SmC materials.

## 7.2.2 – TEST MATRIX FOR EXPERIMENT 1

*Table 7.3 – Test Matrix for Experiment 1*

<i>Experiment</i>	<i>Time Period</i>	<i>Bubble Chamber Set T</i>	<i>Chamber Pressure</i>	<i>Chamber Tempera- ture</i>	<i>Bubble Thickness</i>	<i>Island Thickness</i>	<i>Macro Observation</i>	<i>Micro Observation High Res Video 20X</i>
Ostwald Ripening of the Emulsion; Island Coalescence in SmA materials	1 hr at each T	T=20°C to 30°C	Every 30 s	Every 30 s	Every min.	Every 5 s for first 15 min, then every min.	Observe continuously, take data every 2 min.	Observe, take data continuously for 15 min.
Ostwald Ripening of the Emulsion; Island Coalescence in SmC materials	1 hr at each T	T=20°C to 60°C	“	“	“	“	“	“



## 7.3.1 – EXPERIMENT 2: 2D THERMO-CAPILLARY EFFECTS

- *Thermo-capillary Effects, Temperature Gradient-Induced Flow and its Effect on Island Organization and Dynamics*
- *Thermomigration of Islands*

In this experiment, we will create islands using air jets.

- (1) Illuminate chamber with white light.
- (2) Temperature control at desired temperature.
- (3) Create dense islands by blowing air over the film by air jets (for 3 minutes).
- (4) Set temperature of the air jet needles in order to maintain a temperature difference of 30°C between them. For example, one needle could be at 50°C and the opposing needle at 20°C.
- (5) Monitor temperature of bubble chamber every 30 s.
- (6) Monitor temperature of the needle continuously throughout the experiment.
- (7) Monitor macro image of bubble continuously (observe for 1 hour 15 minutes).
- (8) Measure bubble thickness (sample every minute).
- (9) Measure island thickness continuously.
- (10) Continuous, high-resolution micro observation, acquire data continuously for 60 minutes, microscope objective of 20X.
- (11) Turn off temperature control of air jet needles.
- (12) Set chamber temperature to 50°C (20°C). Cool (heat) both needles to same temperature (20°C (50°C)). This is to observe the thermomigration of islands.
- (13) Observe for both signs of temperature gradient as in steps (5) to (10).
- (14) Turn off all temperature control of needles. Equilibrate and control the bubble chamber to desired temperature (20°C).

## 7.3.2 – TEST MATRIX FOR EXPERIMENT 2

Table 7.4 – Test Matrix for Experiment 2

<i>Experiment</i>	<i>Time Period</i>	<i>Bubble Chamber Set T</i>	<i>Bubble Needle Temperature</i>	<i>Air Jet Needle Temperature</i>	<i>Bubble Thickness</i>	<i>Island Thickness</i>	<i>Chamber Temperature</i>	<i>Macro Observation</i>	<i>Micro Observation High Res Video 20X</i>
Thermocapillary Effects	1 hr	T= 20°C		one each at 20°C and 50°C respectively	Every min.	Every 5 s for first 15 min, then every min.	Every 30 s	Observe continuously, take data every 2 min.	Observe, take data continuously for 15 min.
Thermomigration	1 hr	T= 20°C or T= 50°C		both 50°C or both 20°C	“	“	“	“	“

## 7.4.1 – EXPERIMENT 3: 2D HYDRODYNAMICS

- *Observation of Electric Field-Induced Island/Droplet Interactions and Effect on Orientational Textures*
- *Study of Hydrodynamics of Islands/Droplets and Film Flow (Laminar and Turbulent)*

In this experiment, we will create island / droplet emulsions using the air jets / IDD.

- (1) Illuminate chamber with white light.
- (2) Temperature control at desired temperature.
- (3) Islands: Create dense islands by blowing air over the film by air jets (5 sscm) for 1–2 minutes (usual extensional flow). Turn off air flow.  
Droplets: Create a droplet pattern using the IDD for a few seconds.
- (4) Apply dc electric field across the tangential air jet needles (100 V / mm) for 5 minutes.
- (5) Monitor temperature of bubble chamber every 30 s.
- (6) Monitor macro image of bubble (observe 1 hour, record every 2 minutes.)
- (7) Measure bubble thickness (sample every minute).
- (8) Measure island thickness (monitor continuously but take data every 5 s for first 15 min).
- (9) Continuous, high-resolution micro observation, acquire data continuously for 15 minutes, microscope objective of 20X.
- (10) Go to step (4), change the electric field to sinusoidal voltage at 100 Hz.
- (11) Observation as in steps (5) to (10).
- (12) Turn off electric field, execute the following experiment.

*Study of Hydrodynamics of Islands/Droplets and Film Flow (Laminar and Turbulent Flow on Bubble Films)*

- (13) Turn on two opposing air jet needles with laminar air flow (1 sccm) for 60 s. Turn off air flow.
- (14) Continuous, high-resolution micro observation, acquire data continuously for 15 minutes, with 20X microscope objective, to record island or droplet motion on the bubble surface.
- (15) Raise temperature incrementally and repeat steps (13) to (14) at each temperature; use 1°C increments up to T=30°C for SmA materials, 5°C increments up to T=60°C for SmC materials.
- (16) Turn on two opposing air jet needles with laminar air flow (10 to 150 sccm) for 60 s. Turn off air flow.
- (17) Continuous, high-resolution micro observation, acquire data continuously for 15 minutes, with 20X microscope objective.
- (18) Raise temperature incrementally and repeat steps (17) and (18) at each temperature; use 1°C increments up to T=30°C for SmA materials, 5°C increments up to T=60°C for SmC materials.

## 7.4.2 – TEST MATRIX FOR EXPERIMENT 3

Table 7.5 – Test Matrix for Experiment 3

<i>Experiment</i>	<i>Time Period</i>	<i>Bubble Chamber Set T</i>	<i>E Field between Opposing Needles</i>	<i>Laminar Air Flow</i>	<i>Turbulent Air Flow</i>	<i>Chamber Temperature</i>	<i>Bubble Thickness</i>	<i>Island Thickness</i>	<i>Macro Observation</i>	<i>Micro Observation High Res Video 20X</i>
E field (dc )	1 hr	T=20°C	dc 100 V/mm for 30 s			Every 30 s	Every min.	Every 5 s for first 15 min, then every min.	Observe continuously, take data every 2 min.	Observe, take data continuously for 15 min.
E field (ac )	1 hr	T=20°C	ac 100 Hz 100V/mm for 30 s			“	“	“	“	“
Laminar Air Flow	1 hr	T=20°C to 30°C for SmA materials T=20°C to 60°C for SmC materials		Flow on for 1–2 min.		“	“	“	“	“
Turbulent Air Flow	1 hr	T=20°C to 30°C for SmA materials T=20°C to 60°C for SmC materials			Flow on for 1–2 min.	“	“	“	“	“

## 7.5.1 – EXPERIMENT 4: NUCLEATION OF ISLANDS AND PORES

- *Nucleation of Islands and Holes.*
  - *Bubble Dynamics*
- (1) Temperature control at desired temperature.
  - (2) Create dense islands by blowing air over the film by air jets (for 1–2 minutes).
  - (3) Turn on bubble oscillation for 2 to 5 minutes.
  - (4) Monitor temperature of bubble chamber every 30 s.
  - (5) Monitor macro image of bubble (observe 1 hour 15 minutes, record every 2 minutes).
  - (6) Measure bubble thickness (sample every minute).
  - (7) Measure island thickness (monitor continuously but take data every 5 s for 15 min and then sample once per minute until the end of the experiment).
  - (8) Continuous, high-resolution micro observation, acquire data continuously for 60 minutes, microscope objective of 20X.

## 7.5.2 – TEST MATRIX FOR EXPERIMENT 4

Table 7.6 – Test Matrix for Experiment 4

<i>Experiment</i>	<i>Time Period</i>	<i>Bubble Chamber Set T</i>	<i>Bubble Needle Temperature</i>	<i>Pressure Quench</i>	<i>Bubble Thickness</i>	<i>Island Thickness</i>	<i>Chamber Temperature</i>	<i>Macro Observation</i>	<i>Micro Observation High Res Video 20 X</i>
Bubble Dynamics	1 hr	T= 20 °C		0 to 30 Hz	Every min.	Every 5 s for first 15 min, then every min.	Every 30 s	Observe continuously, take data every 2 min.	Observe, take data continuously for 15 min.

## 8 – FLIGHT RESULTS

### 8.1 – EVALUATION OF SUCCESS CRITERIA

The flight experiment will be considered successful if several of the following scientific experiments (arranged below in decreasing order of importance) can be carried out:

#### 8.1.1 – MAKE AND OBSERVE 2D ISLAND EMULSIONS

- Study Ostwald ripening (several data sets).
- Study island coalescence (several data sets).
- Vary temperature to observe dynamics in N, SmA, and SmC phases.

#### 8.1.2 – 2D HYDRODYNAMICS OF SMECTIC FILMS AND ISLANDS

- Set up and monitor laminar and turbulent flow in bubble films.
- Observe Brownian motion of islands.
- Observe correlations in motions of neighboring islands.
- Vary bubble diameter and thickness of islands

#### 8.1.3 – ELECTRIC FIELD EFFECTS

- Modify island interactions by charging.
- Observe formation, stability and interaction of island chains.

#### 8.1.4 – THERMOCAPILLARY EFFECTS

- Observe island flow and redistribution in response to temperature gradients.
- Observe SmC texture changes in response to temperature gradients.

#### 8.1.5 – CREATION AND OBSERVATION OF ISOTROPIC DROPLET INTERACTIONS ON BUBBLE

- Use the Inkjet Droplet Dispenser (IDD) to create droplets
- Observe droplet interactions with each other and with smectic islands
- Observe droplet response to applied electric fields.

#### 8.1.7 – ISLAND/HOLE GENERATION BY PRESSURE QUENCHES

- Observe a large number of events to establish phenomenology.
- Vary quench depth and rapidity ( $\Delta P$ ,  $dP/dt$ ).
- Modulate bubble size periodically and observe effect on islands and holes.

## 8.2 – *POSTFLIGHT DATA DELIVERABLES*

### 8.2.1 – *DATA ARCHIVING*

- Complete frame-by-frame, time-stamped macro-view camera and micro-view camera video.
- Simultaneous record of physical parameters.
  - Temperature
  - Voltages
  - Bubble diameter
  - Color spectrum
- Astronaut procedures (audio).
- User commands.
- Computer logs.

### 8.2.2 – *DATA INTERPRETATION*

- Digital processing of video images.
  - Size distribution of islands on bubble vs. time.
  - Dynamic correlations of island density.
  - Relaxation following flow and electric field perturbation.
- Correlation with physical parameters
  - Chamber temperature
  - Induced temperature gradient
  - Applied voltage
  - Bubble diameter
  - Film thickness/color spectrum
  - Island thicknesses/color spectrum
  - Island diameters



## 9 – REFERENCES

1. *Handbook of Liquid Crystals*, D. Demus, J. Goodby, G. W. Gray, H.-W. Spiess, V. Vill eds. (Wiley, Weinheim, 1998).
2. P. G. deGennes and J. Prost, *The Physics of Liquid Crystals*, 2nd edition (Oxford University Press, Oxford, 1993).
3. "LIGHT-SCATTERING STUDY OF TWO-DIMENSIONAL MOLECULAR-ORIENTATION FLUCTUATIONS IN A FREELY SUSPENDED FERROELECTRIC LIQUID-CRYSTAL FILM," C. Y. Young, R. Pindak, N. A. Clark, and R. B. Meyer, *Physical Review Letters* **40**, 773 – 776 (1978).
4. "LIQUID-HEXATIC PHASE TRANSITIONS IN SINGLE MOLECULAR LAYERS OF LIQUID-CRYSTAL FILMS," R. Geer, T. Stoebe, C. C. Huang, R. Pindak, J. W. Goodby, M. Cheng, J. T. Ho, S. W. Hui, *Nature* **355**, 152 – 154 (1992)
5. "X-RAY OBSERVATION OF A STACKED HEXATIC LIQUID-CRYSTAL B PHASE," R. Pindak, D. E. Moncton, S. C. Davey, and J. W. Goodby, *Physical Review Letters* **46**, 1135 – 1138 (1981).
6. D. R. Nelson, *Defects and Geometry in Condensed Matter Physics* (Cambridge University Press, Cambridge, 2002).
7. "DIRECT MEASUREMENT OF ORIENTATION CORRELATIONS: OBSERVATION OF THE LANDAU-PEIERLS DIVERGENCE IN A FREELY SUSPENDED TILTED SMECTIC FILM," D. H. Van Winkle and N. A. Clark, *Physical Review Letters* **53**, 1157 – 1160 (1984).
8. "X-RAY DETERMINATION OF THE MOLECULAR TILT AND LAYER FLUCTUATION PROFILES OF FREELY SUSPENDED LIQUID-CRYSTAL FILMS," D. J. Tweet, R. Holyst, B. D. Swanson, H. Stragier, and L. B. Sorensen, *Physical Review Letters* **65**, 2157 – 1160 (1990).
9. "FERROELECTRIC-ANTIFERROELECTRIC PHASE TRANSITION IN A TWO-MOLECULAR-LAYER FREE-STANDING LIQUID-CRYSTAL FILM," Ch. Bahr and D. Fliegner, *Physical Review Letters* **70**, 1842 – 1845 (1993).
10. "SPONTANEOUS FORMATION OF MACROSCOPIC CHIRAL DOMAINS IN A FLUID SMECTIC PHASE OF ACHIRAL MOLECULES," D. R. Link, G. Natale, R. F. Shao, J. E. MacLennan, N. A. Clark, E. Körblova, and D. M. Walba, *Science* **278**, 1924 – 1927 (1997).
11. "MONOPOLE-ANTIMONOPOLE ANNIHILATION IN A NEMATIC LIQUID CRYSTAL," A. Pargelis, N. Turok, and B. Yurke, *Physical Review Letters* **67**, 1570 – 1573 (1991).
12. "SCALING MODEL OF ANNIHILATION-DIFFUSION KINETICS FOR CHARGED PARTICLES WITH LONG-RANGE INTERACTION," S. F. Burlatsky, V. V. Ginzburg, and N. A. Clark, *Physical Review E* **54**, R1056 – R1057 (1996).
13. "SIMULTANEOUS OBSERVATION OF ELECTRIC FIELD COUPLING TO LONGITUDINAL AND TRANSVERSE FERROELECTRICITY IN A CHIRAL LIQUID CRYSTAL," D. R. Link, J. E. MacLennan, and N. A. Clark, *Physical Review Letters* **77**, 2237 – 2240 (1996).
14. "SPONTANEOUS FORMATION OF POLAR CHIRAL LAYERS FROM ACHIRAL MOLECULES IN A NOVEL ANTIFERROELECTRIC LIQUID CRYSTAL PHASE," D. R. Link, G. Natale, R. Shao, J. E. MacLennan, N. A. Clark, E. Körblova, and D. M. Walba, *Science* **278**, 1924 – 1927 (1997).
15. "THE CASE OF THRESHOLDLESS ANTIFERROELECTRICITY: POLARIZATION-STABILIZED TWISTED SMC\* LIQUID CRYSTALS GIVE V-SHAPED ELECTRO-OPTIC RESPONSE," N. A. Clark, J. E. MacLennan, R. Shao, D.A Coleman, S. Bardon, T. Bellini, D. R.

- Link, G. Natale, M. A. Glaser, D. M. Walba, M. D. Wand, X.-H. Chen, P. Rudquist, J. P. F. Lagerwall, M. Buivydas, F. Gouda, and S. T. Lagerwall, *Journal of Materials Chemistry* **9**, 1257 – 1261 (1999).
16. "ANTICLINIC SMECTIC-C SURFACES ON SMECTIC-A FREELY-SUSPENDED LIQUID-CRYSTAL FILMS," D. R. Link, G. Natale, N. A. Clark, J. E. MacLennan, M. Walsh, S. S. Keast, and M. E. Neubert, *Physical Review Letters* **82**, 2508 – 2511 (1999).
  17. "ORIENTATION FIELD FRACTURE IN A LIQUID CRYSTAL: METASTABLE ANTICLINIC MOLECULAR TILT IN ADJACENT LAYERS IN SMECTIC C DOBAMBC AND TFMHPOBC," D. R. Link, G. Natale, J. E. MacLennan, N. A. Clark, M. Walsh, S. S. Keast, and M. E. Neubert, *Physical Review Letters* **83**, 3665 – 3668 (1999).
  18. "RING PATTERN DYNAMICS IN SMECTIC-C\* AND SMECTIC-C<sub>A</sub>\* FREELY SUSPENDED LIQUID CRYSTAL FILMS," D. R. Link, L. Radzihovsky, G. Natale, J. E. MacLennan, N. A. Clark, M. Walsh, S. S. Keast, and M. E. Neubert, *Physical Review Letters* **84**, 5772 – 5775 (2000).
  19. "MICRO-SEGREGATION, MOLECULAR SHAPE AND MOLECULAR TOPOLOGY – PARTNERS FOR THE DESIGN OF LIQUID CRYSTALLINE MATERIALS WITH COMPLEX MESOPHASE MORPHOLOGIES," C. Tschierske, *Journal of Materials Chemistry* **11**, 2647 – 2671 (2001).
  20. "MESOMORPHIC BEHAVIOUR OF 1,3-PHENYLENE BIS[4-(4-ALKOXYPHENYLIMINO METHYL)BENZOATES] AND RELATED COMPOUNDS," T. Akutagawa, Y. Matsunaga, and K. Yasuhara, *Liquid Crystals* **17**, 659 – 666 (1994).
  21. "THE SMECTIC XP PHASES: CHIRAL LIQUID CRYSTALS FROM ACHIRAL MOLECULES," D. M. Walba, E. Korblova, R. F. Shao, J. E. MacLennan, D. R. Link, and N. A. Clark, *Proceedings of the Fifth International Display Workshops of the Society for Information Display*, Kobe, Japan (1998).
  22. "POLARIZATION-MODULATED SMECTIC LIQUID CRYSTAL PHASES," D. A. Coleman, J. Fernsler, N. Chattham, M. Nakata, Y. Takanishi, E. Korblova, D. R. Link, R.-F. Shao, W. G. Jang, J. E. MacLennan, O. Mondain-Monval, C. Boyer, W. Weissflog, G. Pelzl, L.-C. Chien, J. Zasadzinski, J. Watanabe, D. M. Walba, H. Takezoe, and N. A. Clark, *Science* **301**, 1204 – 1211 (2003).
  23. "EFFECT OF HIGH SPONTANEOUS POLARIZATION ON DEFECT STRUCTURES AND ORIENTATIONAL DYNAMICS OF TILTED CHIRAL SMECTIC FREELY SUSPENDED FILMS," D. R. Link, N. Chattham, J. E. MacLennan, and N. A. Clark, *Physical Review E* **71**, 021704 (2005).
  24. "GAS PERMEATION THROUGH ULTRATHIN LIQUID LAYERS," J.-J. Li, H. Schüring, and R. Stannarius, *Langmuir* **18**, 112 – 119 (2002).
  25. "SURFACE TENSIONS OF SMECTIC LIQUID CRYSTALS," H. Schüring, C. Thieme, and R. Stannarius, *Liquid Crystals*, **28**, 241 – 252 (2001).
  26. "EXPERIMENTAL STUDY OF THE BURSTING OF INVISCID BUBBLES," F. Müller, U. Kornek, and R. Stannarius, *Physical Review E* **75**, 065302(R) (2007).
  27. "ATOMIC-DETAIL SIMULATION STUDIES OF TILTED SMECTICS," M. A. Glaser, R. Malzbender, N. A. Clark, and D. M. Walba, *J. Phys.: Condens. Matter* **6**, A261 – A268 (1994).
  28. "ATOMISTIC SIMULATION AND MODELING OF LIQUID CRYSTALS," M. A. Glaser, in *Advances in the Computer Simulation of Liquid Crystals*, C. Zannoni and P. Pasini, ed (Kluwer, Dordrecht, 1999).
  29. "QUANTUM CHEMISTRY BASED FORCE FIELDS FOR SOFT MATTER," M. A. Glaser, N. A. Clark, E. Garcia, and D. M. Walba, *Spectrochimica Acta A* **53**, 1325 – 1340 (1997) [se-

- lected by the *Spectrochimica Acta* editors as one of the 10 best papers published in *Spectrochimica Acta* in 1997].
30. "PHOTOCONTROLLED NANOPHASE SEGREGATION IN A LIQUID-CRYSTAL SOLVENT," Y. Lansac, M. A. Glaser, N. A. Clark, O. D. Lavrentovich, *Nature* **398**, 54 (1999).
  31. "FLUCTUATIONS AND CLINICITY IN TILTED SMECTIC LIQUID CRYSTALS," M. A. Glaser and N. A. Clark, *Physical Review E* **66**, 021711 (2002).
  32. "PHASE BEHAVIOR OF BENT-CORE MOLECULES," Y. Lansac, P. K. Maiti, N. A. Clark, and M. A. Glaser, *Physical Review E* **67**, 011703 (2003).
  33. "INDUCED ANTIFERROELECTRIC SMECTIC- $C_A^*$  PHASE BY DOPING FERROELECTRIC- $C^*$  PHASE WITH BENT-SHAPED MOLECULES," E. Gorecka, *Physical Review Letters* **85**, 2526 – 2529 (2000).
  34. "INDUCED ANTICLINIC ORDERING AND NANOPHASE SEGREGATION OF BOW-SHAPED MOLECULES IN A SMECTIC SOLVENT," P. K. Maiti, Y. Lansac, M. A. Glaser, and N. A. Clark, *Physical Review Letters* **88**, 065504 (2002).
  35. "NANOPHASE SEGREGATION AND FRUSTRATION: CHIRALITY, SPLAY AND CURVATURE IN BENT-CORE SMECTICS," M. A. Glaser, N. A. Clark, and Y. Lansac, presented at the *11th International Conference on Ferroelectric Liquid Crystals*, Sapporo, Japan (2007).
  36. "WHEN BOUNDARIES DOMINATE: DISLOCATION DYNAMICS IN SMECTIC FILMS," P. Oswald, P. Pieranski, F. Picano, and R. Holyst, *Physical Review Letters* **88**, 015503 (2002).
  37. "OBSERVATION OF A CHIRAL-SYMMETRY-BREAKING TWIST-BEND INSTABILITY IN ACHIRAL FREELY SUSPENDED LIQUID CRYSTAL FILMS," J. Pang and N. A. Clark, *Physical Review Letters* **73**, 2332 – 2335 (1994).
  38. "MANIPULATION OF ISLANDS ON FREELY SUSPENDED SMECTIC FILMS AND BUBBLES USING OPTICAL TWEEZERS," A. Pattanaporkratana, C. S. Park, J. E. MacLennan, and N. A. Clark, *Ferroelectrics* **310** 131 – 136 (2004), [www.e-lc.org](http://www.e-lc.org).
  39. "DIRECT MEASUREMENT OF INTERACTION FORCES BETWEEN ISLANDS ON FREELY SUSPENDED SMECTIC C FILMS USING MULTIPLE OPTICAL TWEEZERS," A. Pattanaporkratana, C. S. Park, J. E. MacLennan, and N. A. Clark, *Ferroelectrics*, **344**, 71–80, (2006).
  40. "SELF-ORGANIZATION OF ISOTROPIC DROPLETS IN SMECTIC-C FREE-STANDING FILMS," C. Völtz and R. Stannarius, *Physical Review E* **70**, 061702 (2004).
  41. "DIFFERENT MECHANISMS OF NUCLEATION AND SELF-ORGANIZATION OF DROPLETS IN FERROELECTRIC SMECTIC MEMBRANES," P. V. Dolganov, H. T. Nguyen, G. Joly, V. K. Dolganov, and P. Cluzeau, *European Physical Journal E* **25** 31 – 38 (2008).
  42. "ISOTROPIC DROPLETS IN THIN FREE STANDING SMECTIC FILMS," H. Schüring and R. Stannarius, *Langmuir* **18** 9735 – 9743 (2002).
  43. "INCLUSIONS IN FREE STANDING SMECTIC LIQUID CRYSTAL FILMS," C. Bohley, and R. Stannarius, *Soft Matter* **4**, 683 – 702 (2008).
  44. "COLLOIDS ON FREE-STANDING SMECTIC FILMS," M. Conradi, P. Zihlerl, A. Sarlah, and I. Musevic, *European Physical Journal E* **20** 231 – 236 (2006).
  45. "BUCKLING INSTABILITY OF DROPLET CHAINS IN FREELY SUSPENDED SMECTIC FILMS, " C. Völtz and R. Stannarius, *Physical Review E* **72**, 011705 (2005); "SPONTANEOUS BUCKLING OF COMPRESSIBLE DROPLET CHAINS IN FREE STANDING SMECTIC-C FILMS," R. Stannarius and C. Völtz, *Physical Review E* **72**, 032701 (2005).

46. "GRAIN BOUNDARY SCARS AND SPHERICAL CRYSTALLOGRAPHY," A. R. Bausch, M. J. Bowick, A. Cacciuto, A. D. Dinsmore, M. F. Hsu, D. R. Nelson, M. G. Nikolaides, A. Travasset, and D. A. Weitz, *Science*, **299**, 1716 – 1718 (2003).
47. "THE SMECTIC STATE," J. Prost, *Advances in Physics* **33**, 1 – 46 (1984).
48. "COUPLING BETWEEN MENISCUS AND SMECTIC-A FILMS: CIRCULAR AND CATENOID PROFILES, INDUCED STRESS, AND DISLOCATION DYNAMICS," F. Picano, R. Holyst, and P. Oswald, *Physical Review E* **62**, 3747 – 3757 (2000).
49. P. Oswald and P. Pieranski, *Smectic and Columnar Liquid Crystals* (Taylor and Francis, Boca Raton, 2006).
50. "PHYSICS OF SMECTIC MEMBRANES," P. Pieranski et al., *Physica A* **194**, 364 – 389 (1993).
51. "DEPENDENCE OF FILM TENSION ON THE THICKNESS OF SMECTIC FILMS," R. Jaquet and F. Schneider, *Physical Review E* **67**, 021707 (2003).
52. "CONTACT ANGLE BETWEEN SMECTIC FILM AND ITS MENISCUS," A. Poniewierski, P. Oswald, and R. Holyst, *Langmuir* **18**, 1511 – 1517 (2002).
53. "EXPERIMENTAL CHARACTERIZATION OF LAYER THINNING TRANSITIONS," S. Pankratz, P. M. Johnson, H. T. Nguyen, and C. C. Huang, *Physical Review E* **58**, R2721 – R2724 (1998).
54. "THINNING TRANSITIONS IN FREE-STANDING LIQUID-CRYSTAL FILMS AS THE SUCCESSIVE FORMATION OF DISLOCATION LOOPS," S. Pankratz, P. M. Johnson, R. Holyst, and C. C. Huang, *Physical Review E* **60**, R2456 – R2459 (1999).
55. "KINETICS OF LAYER-THINNING TRANSITIONS IN OVERHEATED SMECTIC FILMS," S. Pankratz, P. M. Johnson, A. Paulson, and C. C. Huang, *Physical Review E* **61**, 6689 – 6695 (2000).
56. "DISJOINING PRESSURE AND THINNING TRANSITIONS IN SMECTIC-A LIQUID CRYSTAL FILMS," F. Picano, P. Oswald, and E. Kats, *Physical Review E* **63**, 021705 (2001).
57. "DISLOCATION LOOPS IN OVERHEATED FREE-STANDING SMECTIC FILMS," A. N. Shalaginov and D. E. Sullivan, *Physical Review E* **65**, 031715 (2002).
58. "DIRECTOR CONFIGURATION AND SELF-ORGANIZATION OF INCLUSIONS IN TWO-DIMENSIONAL SMECTIC MEMBRANES," P. V. Dolganov and V. K. Dolganov, *Physical Review E* **73**, 041706 (2006).
59. "REARRANGEMENT OF TOPOLOGICAL DEFECTS AND ANCHORING ON THE INCLUSION BOUNDARY IN FERROELECTRIC SMECTIC MEMBRANES," P. V. Dolganov, H. T. Nguyen, E. I. Kats, V. K. Dolganov, and P. Cluzeau, *Physical Review E* **75**, 031706 (2007).
60. "FERROELECTRICITY-INDUCED EFFECTS IN INTERACTION AND SELF-ORGANIZATION OF INCLUSIONS IN SMECTIC MEMBRANES," P. V. Dolganov, H. T. Nguyen, G. Joly, V. K. Dolganov, and P. Cluzeau, *Europhysics Letters* **76**, 250 – 256 (2006).
61. "EDGE DISLOCATION IN A VERTICAL SMECTIC-A FILM: LINE TENSION VERSUS FILM THICKNESS AND BURGERS VECTOR," J.-C. Geminard, C. Laroche, and P. Oswald, *Physical Review E* **58**, 5923 – 5925 (1998).
62. "EDGE DISLOCATION IN A VERTICAL SMECTIC-A FILM: LINE TENSION VERSUS TEMPERATURE AND FILM THICKNESS NEAR THE NEMATIC PHASE," A. Zywockinski, F. Picano, P. Oswald, and J.-C. Geminard, *Physical Review E* **62**, 8133 – 8140 (2000).

63. "DISLOCATION LOOP DYNAMICS IN FREESTANDING SMECTIC FILMS: THE ROLE OF THE DISJOINING PRESSURE AND OF THE FINITE PERMEABILITY OF THE MENISCUS," P. Oswald, F. Picano, and F. Caillier, *Physical Review E* **68**, 061701 (2003).
64. "ANNIHILATION OF EDGE DISLOCATIONS IN SMECTIC-A LIQUID CRYSTALS," M. Ambrozic, S. Kralj, T. J. Sluckin, S. Zumer, and D. Svensek, *Physical Review E* **70**, 051704 (2004).
65. "DIRECT MEASUREMENT OF THE PERMEABILITY OF THE MENISCUS BORDERING A FREE-STANDING SMECTIC-A FILM," F. Caillier and P. Oswald, *Physical Review E* **70**, 031704 (2004).
66. M. Kleman and O. D. Lavrentovich, *Soft Matter Physics* (Springer-Verlag, New York, 2003).
67. L. Landau and E. Lifshitz, *Theory of Elasticity*, 2nd edition (Pergamon Press, New York, 1981).
68. P. M. Chaikin and T. C. Lubensky, *Principles of Condensed Matter Physics* (Cambridge University Press, Cambridge, 1995).
69. "NONLINEAR THEORY OF DISLOCATIONS IN SMECTIC CRYSTALS: AN EXACT SOLUTION," E. A. Brener and V. I. Marchenko, *Physical Review E* **59**, R4752 – R4753 (1999).
70. "INFLUENCE OF SURFACE TENSION ON THE STABILITY OF EDGE DISLOCATIONS IN SMECTIC A LIQUID CRYSTALS," L. Lejcek and P. Oswald, *J. Phys II France* **1**, 931 – 937 (1991).
71. "DISLOCATIONS IN LAMELLAR AND LIQUID CRYSTAL FILMS: EQUILIBRIUM LOCATION, EDGE PROFILES, AND PHASE TRANSITIONS," R. Holyst, *Physical Review Letters* **72**, 4097 – 4100 (1994).
72. "TOPOLOGICAL INCLUSIONS IN 2D SMECTIC FILMS," D. Pettey, T. C. Lubensky, and D. R. Link, *Liquid Crystals* **25**, 579 – 587 (1998).
73. "COLLOIDAL DIPOLAR INTERACTIONS IN 2D SMECTIC-C FILMS," P. Patricio, M. Tasinkevych, and M. M. Telo da Gama, *European Physical Journal E* **7**, 117 – 122 (2002).
74. "ELLIPTICAL SOFT COLLOIDS IN SMECTIC-C FILMS," N. M. Silvestre, P. Patricio, and M. M. Telo da Gama, *Physical Review E* **74**, 021706 (2006).
75. "DYNAMICS OF THE MOLECULAR ORIENTATION FIELD COUPLED TO IONS IN TWO-DIMENSIONAL FERROELECTRIC LIQUID CRYSTALS," R. A. Pelcovits, R. B. Meyer, and J.-B. Lee, *Physical Review E* **76**, 021704 (2007).
76. "COUPLING OF POLARIZATION AND DISLOCATION IN FERROELECTRIC SMECTIC LIQUID-CRYSTAL FILMS," R. Holyst, A. Poniewierski, P. Fortmeier, and H. Stegemeyer, *Physical Review Letters* **81**, 5848 – 5851 (1998).
77. "FERROELECTRICITY-INDUCED EFFECTS IN INTERACTION AND SELF-ORGANIZATION OF INCLUSIONS IN SMECTIC MEMBRANES," P. V. Dolganov, H. T. Nguyen, G. Joly, V. K. Dolganov, and P. Cluzeau, *Europhysics Letters* **76**, 250 – 256 (2006).
78. "BROWNIAN MOTION IN BIOLOGICAL MEMBRANES," P. B. Saffman and M. Delbruck, *Proceedings of the National Academy of Sciences of the USA* **72**, 3111 – 3113 (1975).
79. "LATERAL MOBILITY OF PROTEINS IN LIQUID MEMBRANES REVISITED," Y. Gambin et al., *Proceedings of the National Academy of Sciences of the USA* **103**, 2098-2102 (2006).
80. "CORRECTIONS TO THE SAFFMAN-DELBROCK MOBILITY FOR MEMBRANE BOUND PROTEINS," A. Naji, A. J. Levine, and P. A. Pincus, *Biophysical Journal* **93**, L49 – L51 (2007).

81. "THE TRANSLATIONAL AND ROTATIONAL DRAG ON A CYLINDER MOVING IN A MEMBRANE," B. D. Hughes, B. A. Pailthorpe, and L. R. White, *Journal of Fluid Mechanics* **110**, 349 – 372 (1981).
82. "THE EFFECT OF CURVATURE AND TOPOLOGY ON MEMBRANE HYDRODYNAMICS," M. L. Henle, R. McGorty, A. D. Dinsmore, and A. J. Levine, [arXiv:cond-mat/0706.2198v1](https://arxiv.org/abs/cond-mat/0706.2198v1) (2007).
83. J. Milnor, *Topology from the Differentiable Viewpoint*, Princeton Landmarks in Mathematics (Princeton University Press, Princeton, 1965).
84. "SURFACE-TENSION-GRADIENT-INDUCED FLOW IN FREELY SUSPENDED LIQUID CRYSTALLINE FILMS," M. I. Godfrey and D. H. Van Winkle, *Physical Review E* **54**, 3752 – 3764 (1996).
85. "TURBULENCE IN FLOWING SOAP FILMS: VELOCITY, VORTICITY, AND THICKNESS FIELDS," M. Rivera, P. Vorobieff, and R. E. Ecke, *Physical Review Letters* **81**, 1417–1420 (1998).